TECHNISCHE
UNIVERSITÄT
WIEN
Vienna | Austria

DISSERTATION

Erosion of Fusion Relevant Materials - Experiments and Modelling

Ausgeführt zum Zwecke der Erlangung des akademischen Grades
eines Doktors der technischen Wissenschaften
unter der Leitung von

Univ.-Prof. Dr. Friedrich Aumayr
E134
Institut für Angewandte Physik

eingereicht an der Technischen Universität Wien
Fakultät für Physik

von

Ing. Dipl.-Ing. Reinhard Stadlmayr
Matrikelnummer: 00925015
Scheugasse 1/13, 1100 Wien

Wien, Februar 2020   (Reinhard Stadlmayr)

"Anyway, one problem at a time."

– Andy Weir, The Martian

Kurzfassung

Der Hunger der Menschheit nach immer mehr Energie dauert an. Um diesen Bedarf auch in Zukunft decken zu können und dabei das Weltklima nicht noch mehr zu beeinflussen, ist die Forschung im Bereich Kernfusion unverzichtbar. Leider gibt es noch viele physikalische und technische Probleme zu lösen, bevor das Prinzip der Kernfusion in einem Kraftwerk eingesetzt werden kann. Insbesondere die Innenwand eines solchen Reaktors, welche die erste Grenze zwischen dem Fusionsplasma und dem Reaktorkessel darstellt, muss extremen Bedingungen standhalten. Die hohe Wärmebelastung, die Neutronenstrahlung und die Zerstäubung durch Teilcheneinschlag führen zu Erosion und verkürzen die Lebensdauer der Wandkomponenten. Die vorliegende Arbeit konzentriert sich auf die Untersuchung der Erosion von Fusions-relevanten Wandmaterialien durch Ioneneinschlag. Unter präzisen Laborbedingungen wurde die Zerstäubung dünner Filme aus Wolfram, Eisen und Beryllium sowie Eisen-Wolfram-Mischfilme unter Deuterium- und Argonbestrahlung mit der hochempfindlichen TU Wien Quartzkristall-Mikrowaagen-Technik (QCM) untersucht. Darüber hinaus wurde die Erosion von nanostrukturiertem Wolfram (W-Fuzz) unter Argonbestrahlung untersucht, wobei hier die QCM in 'Auffänger' Konfiguration eingesetzt wurde. Obwohl für W-Fuzz eine hohe Erosionsrate vermutet wurde, kann im Experiment gezeigt werden, dass solche Nanostrukturen nur etwa 5% der Zerstäubungsausbeute von festem Wolfram haben.

Die in-situ Messungen der QCM Methode in Kombination mit Oberflächenuntersuchungen mittels Atomkraft- und Rasterelektronenmikroskopie sowie Messungen von Elementtiefenprofilen mittels Ionenstrahlanalysemethoden zeigen den dynamischen Prozess der Erosion unter Ionenbeschuss sehr detailliert. Dies ermöglicht den Vergleich und das "Benchmarken" der Erosionsmodellierung durch neu entwickelte dynamische Codes, die Oberflächenmorphologien, Elementtiefenprofile und sogar Nanostrukturen berücksichtigen können.

Diese Arbeit zeigt, dass oberflächensensible MC-BCA Programme, wie SDTrimSP-2D und TRI3DYN, in der Lage sind, das Ergebnis von Experimenten vorherzusagen, wenn präzise Oberflächenmorphologien und elementare Probenzusammensetzungen verfügbar sind. Darüber hinaus wurde zum ersten Mal der 3D-Code TRI3DYN erfolgreich zur Reproduktion der Erosion einer nanostrukturierten Oberfläche eingesetzt. Die physikalischen Grenzen der Modellierungsmethoden müssen jedoch immer berücksichtigt werden.

Im Laufe der Arbeiten wurden auch Anstrengungen unternommen, die TU Wien QCM zu verbessern. Eine quasi gleichzeitige Anregung mehrerer Eigenmoden ermöglicht die Kompensation von Frequenzänderungen auf Grund von Temperaturänderungen von bis zu $700\,\mathrm{K}$. Mit dieser neuen Technik konnte gezeigt werden, dass in Beryllium implantiertes Deuterium bereits unterhalb von $500\,\mathrm{K}$ vollständig desorbiert.

Abstract

Mankind's hunger for more and more energy does not stop. In order to satisfy this demand and not to influence the world climate even more, research on nuclear fusion is indispensable. Unfortunately, there are still many physical and technical problems to be solved before the principle of nuclear fusion can be used in a power plant. Especially the inner wall of such a reactor, which is the first boundary between the extremely hot plasma and the reactor vessel, must withstand harsh conditions. The extremely high heat loads, the excessive neutron radiation and severe sputtering by particle impact causes erosion and reduces the lifetime of wall components.

This thesis focuses on the investigation of the erosion of fusion relevant wall materials by projectile impact. Under well defined laboratory conditions the sputtering of thin films of tungsten, iron, and beryllium as well as iron-tungsten mixed films under deuterium and argon irradiation was investigated using the highly sensitive TU Wien quartz crystal microbalance technique. Furthermore, the erosion of nanostructured tungsten (W-fuzz) under argon irradiation was investigated, using the quartz crystal microbalance in catcher configuration. Although W-fuzz was suspected to have a high erosion rate, it could be demonstrated experimentally that such nanostructures show only about 5% of the sputtering yield of bulk tungsten.

In situ measurements with the quartz crystal microbalance method, in combination with surface investigations using atomic force microscope and scanning electron microscopy, as well as elemental depth profile measurements via ion beam analysis, reveal the dynamic process of erosion under ion bombardment in high detail. This allows the comparison with and benchmarking of erosion modelling by newly developed dynamic codes, which can take into account elemental composition, surface morphologies and even nanostructures.

This work shows that surface morphology sensitive MC-BCA codes, like SDTrimSP-2D and TRI3DYN are capable to forecast the outcome of experiments, if precise surface morphologies and elementary sample compositions are available. Furthermore, for the first time, the full 3D code TRI3DYN was successfully used to reproduce the erosion of a W-fuzz. The physical limits of the modelling methods, however, must always be considered.

During the work also efforts were made to improve the TU Wien quartz crystal microbalance. A quasi simultaneous excitation of two eigenmodes allows to compensate for frequency changes due to temperature changes up to $700\,\mathrm{K}$. With this new technique it could be shown, that deuterium implanted in beryllium completely desorbs already below $500\,\mathrm{K}$.

Preface and List of Publications

This thesis was elaborated under the supervision of Prof. Friedrich Aumayr at the Institute of Applied Physics (IAP) at TU Wien, in the years from 2016 to 2020. Several students have contributed to this thesis in the form of project works, bachelor or master theses.

Support and cooperation was also provided by the research centers Max Planck Institute of Plasma Physics (IPP)-Garching, IPP-Greifswald, the Forschungszentrum Jülich (FZJ), the Ångström Laboratoriet in Uppsala and the Helmholtz Zentrum Dresden Rossendorf (HZDR).

Publications as First Author:

- R. Stadlmayr, P.S. Szabo, B. M. Berger, C. Cupak, R. Chiba, D. Blöch, D. Mayer, B. Stechauner, M. Sauer, A. Foelske-Schmitz, M. Oberkofler, T. Schwarz-Selinger, A. Mutzke, F. Aumayr
  "Fluence dependent changes of surface morphology and sputtering yield of iron: Comparison of experiments with SDTrimSP-2D"
  Nucl. Instr. Meth. B 430 (2018), 42-46, URL https://doi.org/10.1016/j.nimb.2018.06.004

- R. Stadlmayr, P.S. Szabo, D. Mayer, C. Cupak, W. Möller, F. Aumayr
  "Erosion of iron-tungsten model films by deuterium ion irradiation: a benchmark for TRI3DYN"
  Phys. Scr. T180 (2020) (in press), URL https://doi.org/10.1088/1402-4896/ab438f
- R. Stadlmayr, P.S. Szabo, D. Mayer, C. Cupak, T. Dittmar, L. Bischoff, S. Möller, M. Rasiński, R.A. Wilhelm, W. Möller, F. Aumayr
  "Sputtering of Nanostructured Tungsten and Comparison to Modelling with TRI3DYN"
  J. Nucl. Mater. 532 (2020), 152019, https://doi.org/10.1016/j.jnucmat.2020.152019

Publications as Co-Author:

- B. Berger, R. Stadlmayr, G. Meisl, M. Cekada, C. Eisenmenger-Sittner, T. Schwarz-Selinger, F. Aumayr
  "Transient effects during erosion of WN by deuterium ions studied with the quartz crystal microbalance technique"
  Nucl. Instr. Meth. B 382 (2016), 82-85, URL https://doi.org/10.1016/j.nimb.2016.04.060
- B. Berger, R. Stadlmayr, D. Blöch, E. Gruber, K. Sugiyama, T. Schwarz-Selinger, F. Aumayr
  "Erosion of Fe-W model system under normal and oblige D ion irradiation"
  Nuclear Materials and Energy 12 (2017), 468-471, URL https://doi.org/10.1016/j.nme.2017.03.030
- B. Berger, P.S. Szabo, R. Stadlmayr, F. Aumayr
  "Sputtering measurements using a quartz crystal microbalance as a catcher"
  Nucl. Instr. Meth. B 496 (2017), 533-537, URL https://doi.org/10.1016/j.nimb.2016.11.039
- P.S. Szabo, R. Chiba, H. Biber, R. Stadlmayr, B. Berger, D. Mayer, A. Mutzke, J. Doppler, M. Sauer, J. Appenroth, J. Fleig, A. Foelske-Schmitz, H. Hutter, K. Mezger, H. Lammer, A. Galli, P. Wurz, F. Aumayr
  "Solar wind sputtering of wollastonite as a lunar analogue material - Comparisons between experiments and simulations"
  Icarus 314 (2018), 98-105, URL https://doi.org/10.1016/j.icarus.2018.05.028
- L. Ballauf, F. Hechenberger, R. Stadlmayr, T. Dittmar, M. Daxner, S. Zöttl, F. Aumayr, Z. Hermana, P. Scheier
  "Formation of beryllium-hydrogen ions in chemical sputtering from 20 to 420 eV"

Nuclear Materials and Energy 22 (2020) 100722, URL https://doi.org/10.1016/j.nme.2019.100722

- P.S. Szabo, H. Biber, N. Jäggi, M. Brenner, D. Weichselbaum, A. Niggas, R. Stadlmayr, A. Mutzke, A. Nenning, M. Sauere, D. Primetzhofer, J. Fleig, A. Foelske-Schmitz, K. Mezger, H. Lammer, A. Galli, P. Wurz, F. Aumayr
"Dynamic Potential Sputtering of Lunar Analogue Material by Solar Wind Ions"
Astrophys. J., (2020) (in press)

International Conference Participations and Talks

Invited Talks:

- R. Stadlmayr
"Erosion of fusion relevant surfaces by using a quartz crystal microbalance"
23rd International Conference on Ion-Surface Interactions (ISI-2017), Moscow/Russia 21.08.2017

- R. Stadlmayr
"Sputtering of Rough PFCs: Benchmarking 3D Binary Collision Approximation Codes with Experiments"
17th International Conference on Plasma-Facing Materials and Components for Fusion Applications (PFMC-17), Eindhoven/Netherlands 23.05.2019

Regular Talks:

- R. Stadlmayr
"Erosion of Fusion Relevant Surfaces by Using a Quartz Crystal Microbalance"
4th Fusion Day, Wien 17.11.2017

- R. Stadlmayr
"Impact of Surface Roughness on Erosion"
Joint Annual Meeting of WP JET2 and WPPFC, Ljubljana/Slovenia 21.11.2017

- R. Stadlmayr
"Erosion investigations of fusion relevant plasma facing materials"
Seminar Institut für Angewandte Physik (IAP), TU Wien 05.11.2019

Posters:

- R. Stadlmayr, B. Berger, D. Blöch, S. Kaser, L. Bergen, F. Aumayr
  "Erosion of iron and iron-tungsten films under deuterium ion impact"
  Symposium on Surface Science (3S*16), St. Christoph am Arlberg/Austria
  24.02.2016

- R. Stadlmayr, B. Berger, P.S. Szabo, D. Blöch, C. Cupak, D. Mayer, B. Stechauner, M. Oberkofler, T. Schwarz-Selinger, A. Mutzke, F. Aumayr
  "Influence of Surface Structural Modifications on the Sputtering Yield of Iron"
  16th International Conference on Plasma-Facing Materials and Components for Fusion Applications (PFMC-16), Neuss, Düsseldorf/Germany
  18.06.2017

- R. Stadlmayr, B. Berger, P.S. Szabo, C. Cupak, R. Chiba, D. Blöch, D. Mayer, B. Stechauner, M. Oberkofler, T. Schwarz-Selinger, A. Mutzke, F. Aumayr
  "Consequence of Surface Morphology Modifications on the Sputtering Yield of Iron"
  22nd International Workshop on Inelastic Ion-Surface Collisions (IISC-2017), Dresden/Germany 20.09.2017

- R. Stadlmayr, P. Szabo, D. Mayer, D. Thima, B. Berger, D. Blöch, F. Aumayr
  "Sputtering of Fusion Relevant Materials and Comparison to SDTrimSP-2D and TRI3DYN"
  Symposium on Surface Science 2018 (3S*18), St. Christoph am Arlberg/Austria 28.02.2018

- R. Stadlmayr, P.S. Szabo, D. Mayer, M. Sauer, A. Foelske-Schmitz, M. Oberkofler, T. Schwarz-Selinger, U. von Toussaint, A. Mutzke, F. Aumayr
  "Impact of surface roughness on the erosion of fusion relevant materials: comparison of experiment to morphology sensitive Monte-Carlo BCA codes"
  23rd International Conference on Plasma-Surface-Interactions in Controlled Fusion Devices (PSI-23), Princeton, NJ/USA 21.06.2018

- R. Stadlmayr, P.S. Szabo, H. Koslowski, P. Hansen, N. Helfer, T. Dittmar, C. Lungu, D. Primetzhofer, C. Linsmeier, F. Aumayr
  "Retention mechanism of hydrogen and helium isotopes in beryllium studied with the quartz crystal microbalance technique"
  10th International Symposium on Swift Heavy Ions in Matter & 28th International Conference on Atomic Collisions in Solids (SHIM-ICACS 2018), Caen/France 03.07.2018

Supervised Students:

- Stefanie Kaser
  "Test of a new Sample Holder for Angle of Incidence dependent Sputter Yield Measurements", Bachelor Thesis 2016
- Daniel Mayer
  "Roughness-Investigation of thin Fe- and Au Layers under Ar Ion Bombardment", Bachelor Thesis 2016
  "Roughness-Investigation of thin Fe layers under 500 eV Ar-ion irradiation", Projekt Work 2017
  "Erosion and Roughness Analysis of Fe and W under Ar Ion Bombardment", Master Thesis 2020
- Dominic Blöch
  "Sputter Yield Measurements with Deuterium on Iron-Tungsten Alloys under different Angles of Incidence", Project Work 2016
  "Influence of Ion Sputtering on Iron-Tungsten Alloy Surfaces and Iron Surfaces", Master Thesis 2017
- Bernd Stechauner
  "Ionen induzierte Erosion von Gold- und Eisenoberflächen", Bachelor Thesis 2017
- Christian Cupak
  "Influence of Surface Structure Modifications on the Sputter Yield of Iron by monoenergetic Argon Ions", Bachelor Thesis 2017
  "Influence of Roughness on Sputter Yields of Tungsten-Coatings relevant for Nuclear Fusion Devices", Master Thesis 2019
- Christopher Stany
  "Design and Setup of a new Experiment for High Flux Sputtering Measurements", Bachelor Thesis 2018
- Daniel Thima
  "Influence of Initial Roughness on the Effect of Ar^{1+} Ion Bombardment on Surface Structure and Sputter Yield of Tungsten", Bachelor Thesis 2019
- Elisabeth Kadletz
  "First Test Measurements of a Dual Mode Quartz-Crystal Microbalance", Bachelor Thesis 2019

Contents

1

Introduction and Motivation

This chapter presents the background of this doctoral thesis and clarifies the motivation. After a short overview of the current problem of climate warming (section 1.1), a possible solution to it is presented in the form of thermonuclear fusion (section 1.2). Subsequently, the principles of a magnetic confined fusion device will be presented and the problems still to be solved in order to be able to actually use this form of energy production (section 1.2.2). In particular, this work should help to bring a nuclear fusion power plant a small step closer to realisation. At the end of this chapter an outline of this thesis is shown (section 1.3).

1.1 Global Energy Demand and Climate Changes

The need for energy is continuously growing in our modern society as well as in third world countries. The consequences of burning fossil fuels are slowly becoming visible in form of weather and climate changes due to global warming of the earth's atmosphere. In figure 1.1 the world's total energy supply by source from the International Energy Agency (IEA) is shown from the year 1990 to 2017 and clearly indicates the substantial increase [1]. A small increase in hydro power as well as wind & solar power is observable, but unfortunately the energy sources producing carbon dioxide (CO_2), like oil, gas, coal were increasing the most. This trend can also be seen in the CO_2 concentration in Earth's atmosphere (figure 1.2), measured at the Mauna Loa Observatory on Hawaii [2, 3].
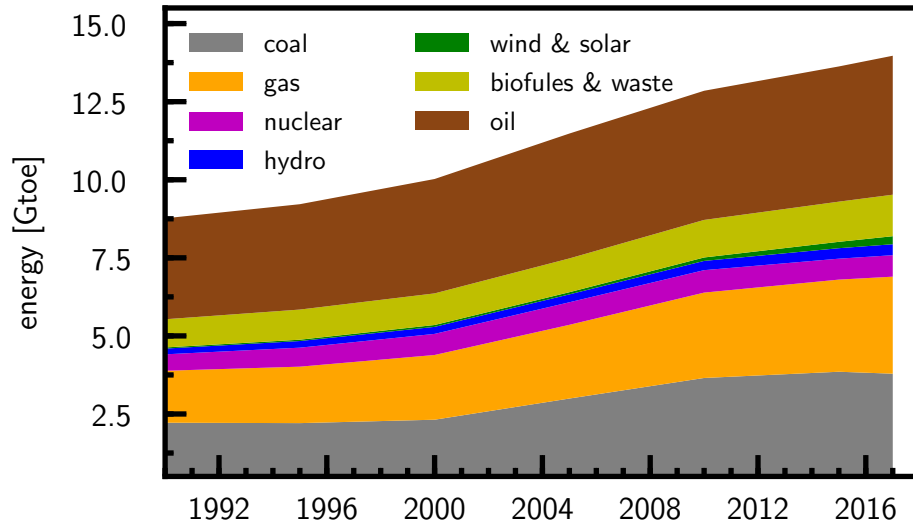
Figure 1.1 – The world total energy supply by source in units of tonnes of oil equivalent (toe) (equal to 11.63 kWh), from the year 1990 to 2017. Based on the IEA data from the IEA World Energy Balances 2019 [1].

As CO_2 is an important heat-trapping or greenhouse gas, it's increase in the atmosphere raises also the global surface temperature, as can be seen in figure 1.2 [3,4]. Since 1990 the global surface temperature increased by 0.7 K which is suspected to be responsible for the increased occurrence of extreme weather conditions.
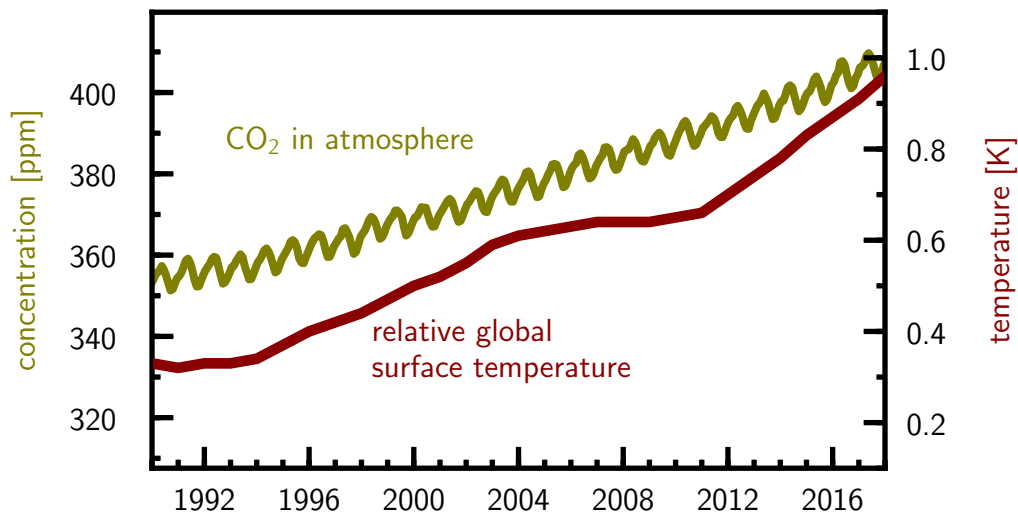
Figure 1.2 – The concentration of CO_2 in atmosphere from the year 1990 to 2018 and the global surface temperature relative to 1951-1980 average temperature. The zigzag pattern is related to the natural annual variation of vegetation [2, 4].

Figures 1.1 and 1.2 clearly demonstrate that this trend will not stop if mankind is not willing to take action.

The expansion of wind and photovoltaic power is a necessary step in the right direction, but with this form of energy alone it will not be possible to completely cover the world's energy needs [5]. Situations are possible in which no energy can be produced, if lack of wind and darkness occurs simultaneously for a longer period of time (designated in German as "Dunkelflaute") [6]. To cover such situations huge energy storage facilities are necessary, which cannot be built so far [5].

Nuclear power could be a possible solution to this problem, as it can generate enormous amounts of energy without releasing any CO_2 or other greenhouse gases. One method of obtaining nuclear energy is the fission of very heavy nucleus, like uranium (^{235}U), thorium (^{232}Th) or plutonium (^{239}Pu) fragmented into two or more lighter nuclei. These nuclear fission power plants are well established since the 1960s and provide a continuous contribution to the world energy balance (compare with figure 1.1). Nevertheless a major disadvantage of fission power plants is the fact that the fission products are highly radioactive and very toxic to humans. For example the resulting elements, like caesium (^{137}Cs), strontium (^{90}Sr), iodine (^{131}I) and zirconium (^{95}Zr) must not be released into our environment and need long time storage facilities, due to the high half-life of some thousands of years of some isotopes as well as their decay products [7]. Although the Egyptians have successfully constructed buildings that are more than 4600 years old and still standing [8], the long-term storage of nuclear waste is still an unsolved problem, since it has to be ensured that the radioactive isotopes do not enter the groundwater or the atmosphere.

Accidents at the nuclear power plant Fukushima Daiichi in Japan 2011 and in Chernobyl in Ukraine 1986 led to long-term contamination of the environment with radioactive isotopes and therefore the surrounding area uninhabitable for decades. Obviously this leads to a massive reduction in public acceptance of fission power plants.

Although electricity generation by nuclear power plants hardly impacts the climate, a complete conversion of the world's entire energy supply to nuclear fission power is inconceivable anyway, since uranium is not sufficiently available worldwide [9]. Research into alternative energy sources such as nuclear fusion is therefore essential.

1.2 Nuclear Fusion Research

An alternative method of obtaining nuclear energy is by thermonuclear fusion, which is shown to us every day anew by our sun. As the binding energy per nucleon below masses of iron (^{56}Fe) is not saturated according to the Bethe-Weizsäcker formula, the fusion of two or more very light nuclei into a heavier one is

energetically favourable [10]. As the mass of the fusion product is lower compared to the sum of the starting materials, the so called mass defect Δm is transformed into energy, according to Einstein's famous equation: $E = \Delta m\, c^2$ [11, 12].

To ignite the fusion process the reactants need to get below a distance of about 10^{-15} m, where the strong interaction force gets dominant. As every atomic nucleus is positively charged they repel each other due to the Coulomb interaction, which makes extreme temperatures ($=$ mean kinetic energy) necessary to bring the reactants so close together. Inside the sun the enormous gravitational forces in its center confines the nuclei sufficiently long for fusion eventually to happen via the quantum tunnelling effect and the weak interaction [13].

To bring the power of the sun to earth a different approach is necessary, as the gravitational forces of the sun cannot be reproduced. Lawson et. al. defined in 1956 the criteria for a power producing thermonuclear reactor: The triple product of ion temperature T_i, ion density n_i and confinement time τ_e must surpass a certain value, in order to realize a self sustained nuclear fusion reaction [14].

On Earth the most favourable fusion process is the reaction of the hydrogen isotopes deuterium (^{2}D) and tritium (^{3}T), as it has the highest reaction rate at lowest temperature. The fusion reaction is shown in equation 1.2.1, where the fusion product is helium (He) and one neutron (n). The energy released during this process is equal to $17.6\,\mathrm{MeV}$ and distributed as kinetic energy between the two fusion products [13, 15].

$$^2_1D \;+\; ^3_1T \;\Rightarrow\; ^4_2He \;+\; ^1_0n \;+\; 17.6\,\mathrm{MeV} \tag{1.2.1}$$
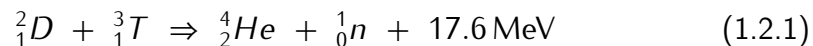
The necessary temperature to fuse D and T into He is still extremely high and in the range of $100 - 200 \times 10^6\,\mathrm{K}$ [15].

A nuclear fusion power plant would have the following advantages:

- The hydrogen isotopes deuterium and tritium are in principle available worldwide in almost unlimited quantities. Deuterium is a natural isotope and can be produced from sea water. Tritium is an unstable element with a half-life of about 12.6 years, therefore it is not naturally available. Nevertheless it can be obtained by neutron bombardment of lithium, which is also available in sufficient quantities [13].

- The D-T fusion process does not produce any long living radioactive isotopes, due to the underlying physical principle. Some of the used materials in the reactor chamber, however, will become radioactively activated due to the neutron bombardment from the fusion process, or by implantation of tritium in the reactor wall. Nevertheless, the radioactive waste of a fusion power plant will consist of relatively short-lived isotopes only and most of the activated material will be recyclable after an intermediate storage of about $30 - 100$ years only [16].

- The fusion reaction is inherently save, because the fuel inside the reactor only last for a couple of seconds, which makes runaway reactions like in a fission reactor, or a meltdown impossible [13].

- There is no risk of terrorist groups stealing key material to build nuclear bombs, as the fuel is readily available and the fusion process is extremely difficult to sustain [13].

While these advantages would make a fusion power plant an ideal source of energy, many technical and physical issues need to be overcome. The enormously high temperatures required to maintain the fusion process, which are even higher than the melting point of any available material, make it necessary to keep the fusion fuel floating as plasma, by using strong magnetic fields.

1.2.1 Tokamak Principle

The currently most advanced idea for a magnetic confined thermonuclear fusion device is the design called "Toroidal Chamber with Magnetic Coils (russian: TOроидальная КАмера с МАгнитными Катушками) (tokamak)". As the name suggests, the reactor chamber is torus-shaped, where toroidal field coils are arranged along this chamber, as shown in figure 1.3. The fusion fuel is inserted into the chamber as gas, up to a density of about 10^{20} atoms/m^3. Thermal energy will be applied to the gas by electron cyclotron resonance (ECR) and/or neutral beam injection (NBI) heating, until it is completely ionised and forms a plasma. This plasma can then be held in place by strong magnetic fields [13].

A toroidal magnetic field alone would not be sufficient for a confinement, as the curvature and gradient in radial direction of the magnetic field causes a drift of the ions and electrons of the plasma in opposite directions. This charge separation causes in turn an electric field and in combination with the toroidal magnetic field an $\vec{E} \times \vec{B}$ drift, increasing the charge separation. An additional magnetic field is necessary to compensate for that. In the center of the tokamak a central solenoid is placed and acts as a primary transformer circuit, which induces a current through the plasma. This plasma current generates then a poloidal magnetic field and in combination with the toroidal magnetic field a helical magnetic field is formed. This twisting of the magnetic field constrains the ions in the plasma to certain paths and allows a confinement for a certain time τ. Unfortunately this time is limited to some seconds, as the maximum induced plasma current is limited. Therefore a tokamak can be operated in pulsed mode only [13, 18, 19].
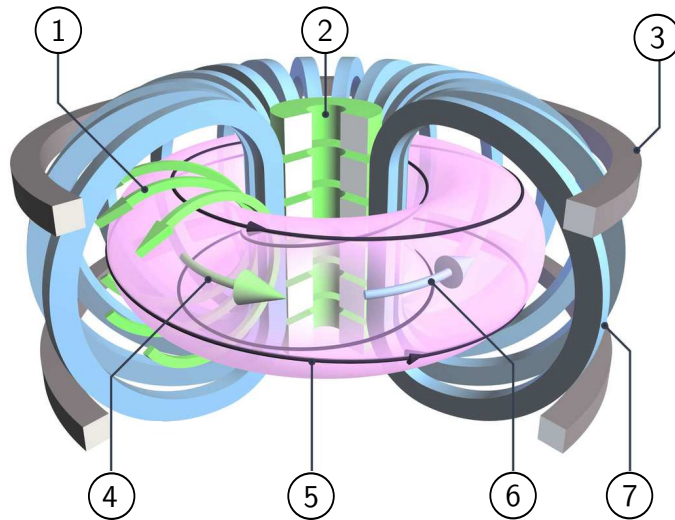
Figure 1.3 – Magnetic field configuration of a tokamak. Figure taken from [17].
① - poloidal magnetic field lines
② - central solenoid (primary transformer circuit)
③ - auxiliary poloidal field coils (for plasma shaping and positioning)
④ - plasma current (secondary transformer circuit)
⑤ - resulting helical magnetic field lines
⑥ - toroidal magnetic field lines
⑦ - toroidal field coils

An alternative configuration of a magnetically confined plasma is the so called "stellarator" design. The idea is here to use complex 3D shaped field coils which generate a helical magnetic field from the beginning [20]. A main advantage of this concept is that inducing a plasma current is no longer necessary to keep up the confinement, which means that theoretically an infinite long operation time is possible. The extremely challenging design and manufacturing of the 3D shaped field coils makes this concept less well explored as the tokamak design. The biggest stellarator experiment today, called Wendelstein-7X, started operation in 2016 and already showed very promising first results [18, 20].

In order to gain more power from nuclear fusion than necessary to heat the plasma and keep up the magnetic field, all magnetically confined thermonuclear reactors available today are too small. The so far biggest machine is Joint European Torus (JET), at the Culham Center for Fusion Energy (CCFE) in the UK. It still holds the world record and reached a factor of $Q(= P_{fus}/P_{in}) \approx 0.62$ only, where Q is the relation of fusion output power (P_{fus}) to the necessary input (heating) power (P_{in}) [21]. As the confinement time τ is largely dependent on the plasma radius and therefore the machine size, larger fusion reactors are necessary to get a $Q > 1$, which is technologically extreme challenging and expensive [13].

In the south of France the world largest nuclear fusion experimental reactor is currently being built, called International Thermonuclear Experimental Reactor (ITER) and follows the tokamak design. It should demonstrate for the first time a self sustained nuclear fusion reaction and should deliver a factor of $Q \geq 10$ [19]. A cross-cut through the reactor chamber of ITER can be seen in figure 1.4. With a height of the reactor chamber of $11.4\,$m and a major plasma radius of $6.2\,$m it will be nearly twice as big as any other fusion device [13, 19].

1.2.2 Plasma Wall Interaction Issues

One of the most challenging parts in a fusion device is the first wall, which faces the ultra-hot plasma. These plasma facing components (PFCs) are constantly eroded by ion and neutral particle bombardment originating from the plasma and must withstand tremendous heat loads, which limit their lifetime. Figure 1.4 shows, next to the cross section of the ITER tokamak, also the main PFCs. ITER will have a full metallic and active cooled first-wall, where the blankets on the side wall will be made out of beryllium and should withstand heat loads of $2 - 4.7\,\mathrm{MW/m^2}$ [19]. The divertor cassettes are located at the bottom of the torus and it's armour will be made out of tungsten [22, 23]. Such a divertor is exposed to the highest possible heat loads, as the magnetic field lines touch the wall here. The divertor also serves to divert the fusion product helium out of the plasma. It will be designed to be capable of withstanding heat loads of $10\,\mathrm{MW/m^2}$ continuously and $20\,\mathrm{MW/m^2}$ for some seconds [19].

Tungsten is the plasma facing material (PFM) of choice, as it has the highest melting point of all materials available and also a very small sputtering yield under low energy hydrogen isotope impact. Still the eroded, or sputtered particles from the wall can enter the plasma and get ionized too. In the case of high-Z materials, like tungsten, the strong radiative cooling effect of these impurities deteriorate the plasma performance and can lead to a breakdown of the fusion process. Therefore the amount of high Z impurities in the plasma need to be kept to a minimum [13, 25, 26].
Beryllium, on the other hand, is also a high-melting material, but with a significantly higher sputtering yield on hydrogen isotope impact. As a low-Z material beryllium causes radiative cooling only in the plasma edge, which is advantageous, as plasma instabilities resulting in edge localized modes (ELMs) are still expected to occur in ITER [13, 27, 28].
As an example of an overloaded PFC, a defective armour can be seen in figure 1.5. It shows images of beryllium blankets of the fusion experiment JET, which were directly exposed to the plasma that exceeding the thermal design. The damage in form of melting at the edges is clearly visible [29].
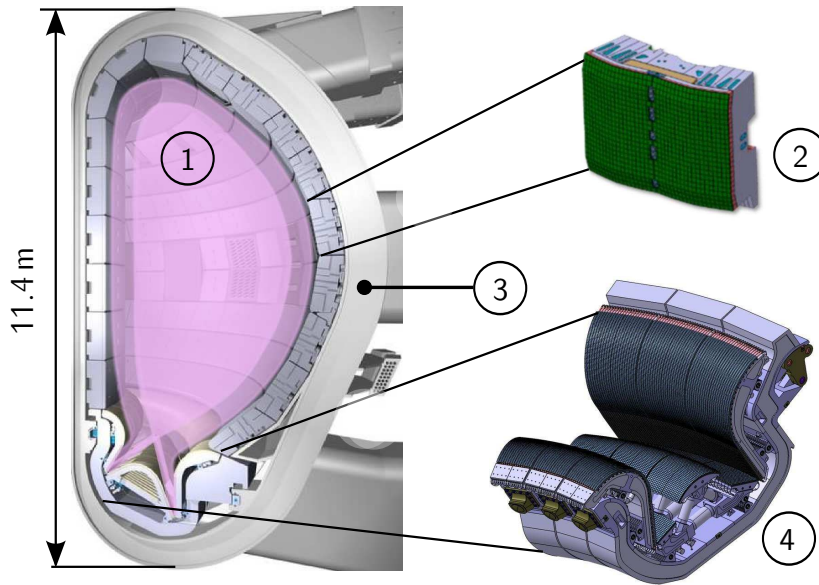
Figure 1.4 – Cross section of the ITER tokamak and the main PFCs. Figures taken from [19, 24].
① - cross section of the toroidal vacuum chamber, showing the typical shape of the plasma
② - side wall blanket module with beryllium armour (green)
③ - steel vacuum chamber with a height of 11.4 m
④ - divertor cassette modules, placed at the bottom of the vacuum chamber, with tungsten armour (dark grey)
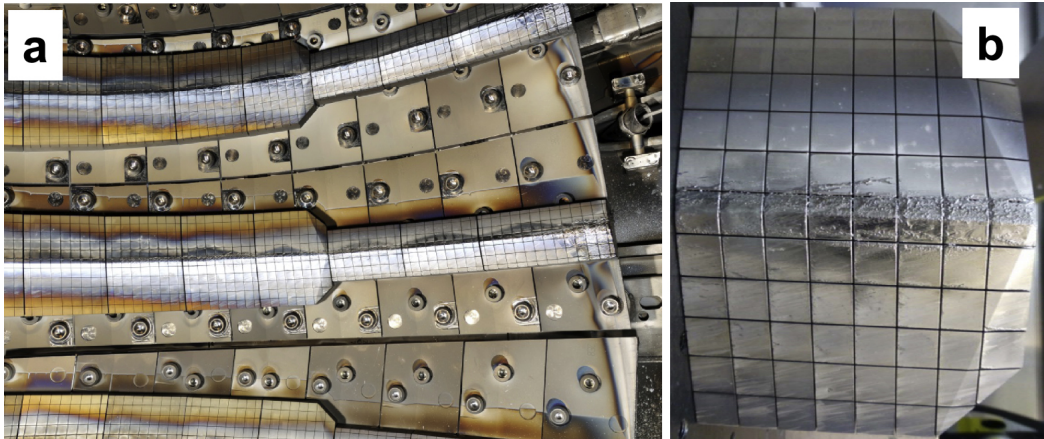
Figure 1.5 – Blankets from the upper part of the fusion experiment JET after direct plasma exposure. In (a) an overview image and in (b) a zoom in to one beryllium blanket can be seen. The damage is clearly visible in form of molten material. Figures taken from [29].

To avoid local overheating of the PFCs, radiative edge cooling is an advantage, as the head is spread over a bigger area. At the fusion experiment ASDEX-Upgrade at IPP-Garching, successful injection of nitrogen was performed, causing a reduced local heat load on the divertor and avoids melting of it's tungsten armour. Furthermore it was found out that a small amount of low Z impurities in the plasma can improve the plasma performance and its confinement [30–32]. For bigger machines, like ITER, the radiative power of nitrogen will not be sufficient and therefore somewhat heavier elements, like noble gases like argon need to be injected into the plasma [30].

The plasma exposure of the PFCs causes also implantation of the fusion fuel into the wall material, a process which should be kept to a minimum, especially for the case of tritium, as it is radioactive [33–36]. Implantation of the fusion ash helium or the seeding gases nitrogen or argon can influence the erosion behaviour and is under continuous research [37–39].

One is also already looking further into the future to the time after ITER and researching more advanced materials. For DEMO, which should be the first energy producing nuclear fusion power plant, a calm and stable plasma can be assumed [40]. This assumption would allow the use of so called tungsten enriched steels, like EUROFER as PFM [41]. It is well known, that high-Z materials have a lower sputtering yield compared to low-Z materials under low energy ion bombardment. This effect can be used to enrich the surface of such steels with a high-Z material, like tungsten, causing a reduced erosion rate. Furthermore steels are cheaper, easier to process and have less weight compared to pure tungsten. The interaction of the plasma with such steels is currently under investigation [38, 42, 43].

1.3 Thesis Outline

In section 1.2.2 the main issues of the plasma wall interactions were presented and the need of further research was pointed out. Many of these plasma surface interaction problems can be reproduced in small scale and investigated with high precision under well defined laboratory conditions.
In this thesis a regular sputter gun was used as particle source, to mimic the particles originating from the plasma, in combination with a quartz crystal microbalance (QCM) technique to measure the erosion of different PFMs with high precision. After a recap of sputtering theory in chapter 2 the used experimental methods are presented in detail in chapter 4.
These accurate erosion studies also allow the benchmarking of erosion modelling

codes such as SDTrimSP and TRIDYN, as well as newly developed surface morphology sensitive codes like TRIDYN in 3D (TRI3DYN). Theses codes are introduced and described in chapter 3.

Since tritium is radioactive, the investigations in this thesis concentrate on the interaction of deuterium, helium, as well as the seeding gas argon with different PFMs, like beryllium (see chapter 8), iron and tungsten (see chapter 5), as well as iron-tungsten alloys (see chapter 6). Furthermore the interaction of argon with nanostructured tungsten (so called W-fuzz) was investigated and will be presented in chapter 7. The final chapter 9 summarizes the main conclusions of this thesis.

2

Sputtering Theory

*Parts of the following chapter have been published in
references [44] and [45].*

Sputtering by ion bombardment is one of the major topics of ion-surface inter-actions and has a wide range of applications, such as surface cleaning, thin film deposition, etching or surface analytical techniques. Sputtering plays also a major role in space weathering by solar wind ion impact, which was observed on lunar or planetary surfaces, but most importantly in the erosion of wall material in a nuclear fusion device [41, 46, 47].

In this chapter a short recap of sputtering by particle bombardment is provided. After a preface in section 2.1, a short overview of physical sputtering is given in section 2.2. In section 2.3 the focuses is layed on the influence of surface roughness and nanostructures.

2.1 Preface

Sputtering is the phenomenon when one or more atoms of a solid are ejected from its surface by the impact of a projectile. These projectiles are usually energetic particles, like ions originating from an ion source or a plasma. The impact of such a projectile on the target initiates a collision cascade in the solid target and spreads its kinetic energy (a model of such a collision cascade can be found in chapter 3, figure 3.1). If the recoil cascade extends back to the surface, a target atom can gain enough kinetic energy to overcome the surface binding energy E_{SB}, it can leave the target and is then considered as sputtered [48].

Besides this form of sputtering, which is called physical sputtering, there are also

effects like chemical and potential sputtering: Chemical sputtering involves chemical reactions between the projectile and the target that allow the surface binding energy E_{SB} to be changed, thereby increasing or decreasing physical sputtering, or to overcome it completely, directly by forming molecules that desorb from the surface [48–50]. Potential sputtering instead, uses the potential energy of the projectile ion in the form of high ionization states to enhance the sputtering. The neutralization process, which begins near the surface, can significantly increase sputtering, especially in the case non-conducting materials [48, 51–53].

In this thesis the focus was put on experiments and modelling of physical sputtering, in the kinetic energy range from $0.1 - 5\,\text{keV/ion}$ which will be explained in the following in more detail.

2.2 Physical Sputtering

The definition of the sputtering yield Y, as shown in equation 2.2.1, is the mean number of emitted particles per impinging projectile. This yield is dependent on many parameters, like the mass of the target atoms as well as the projectiles, the kinetic energy of the projectile, angle of incidence, target composition and the surface binding energy [48, 54].

$$Y = \frac{sputtered\ atoms}{projectile} \tag{2.2.1}$$

In figure 2.1a sputtering yields of typical plasma facing materials (PFMs) under D bombardment are shown, evaluated with the modelling software SDTrimSP. A pronounced energy dependence is observable. The D projectile must exceed a certain threshold energy E_{thr} in order for sputtering to occur. In the case of W an E_{thr} of about $229\,\text{eV}$ was found and for Be an E_{thr} of only about $10\,\text{eV}$ is necessary [48]. The reason for this is mainly the more efficient elastic momentum transfer with less mass differences between projectile and target. With increasing projectile energy the sputtering yield is increasing too, until a maximum is reached. Further increase of the projectile energy causes the sputtering yield to decrease again, as the resulting collision cascade propagates very far into the target and hardly returns back to the surface [48].
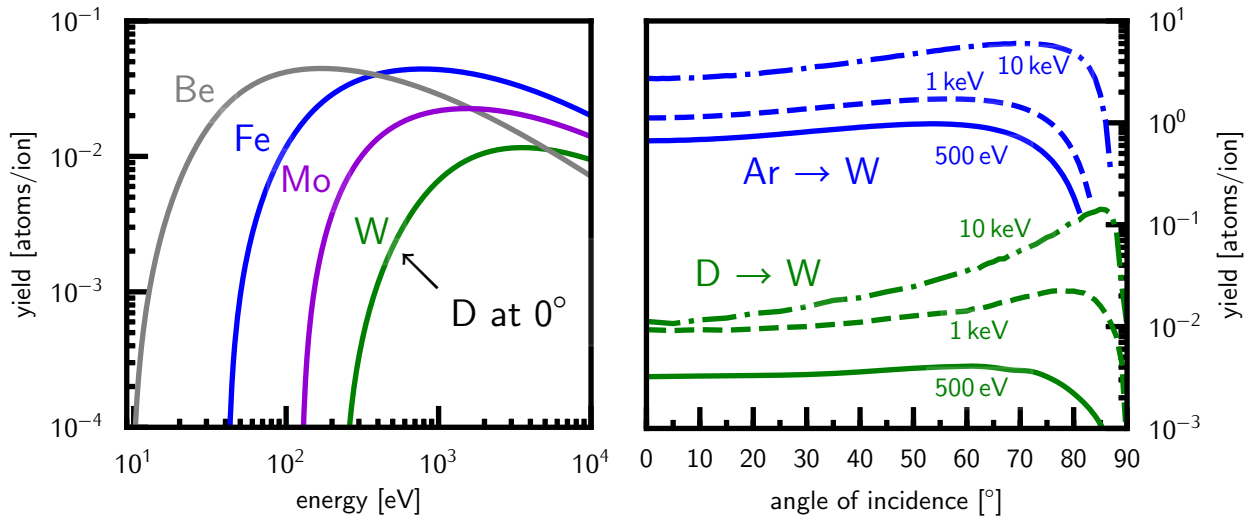
(a) Energy dependence under D irradiation

(b) Angle of incidence dependence

Figure 2.1 – Sputtering yields of typical plasma facing materials (PFMs) calculated with SDTrimSP and assuming pure elemental targets and perfectly flat surfaces. In (a) the energy dependence of Be, Fe, Mo and W under normal incidence (0°) D irradiation can be seen. In (b) the angle of incidence dependence of the sputtering yield is shown for W under D and Ar irradiation at different energies. Note the different scaling of the ordinates.

Figure 2.1b presents the angle of incidence dependence of the sputtering yields for W under Ar and D irradiation at different energies. At angles of incidence close to the surface normal (0°) and up to about 45° a rather constant behaviour with a slight increase can be observed. After further increasing the angle of incidence, an energy and projectile dependent maximum can be found. The reason for this is that the expanding collision cascade stays closer and closer to the surface, which increases the probability that a surface atom will gain enough energy to leave the target. A further increase of the angle of incidence, up to grazing angles of incidence, leads to a decrease of the yield again, because the reflection probability of the projectiles increases significantly [48].

The results in figure 2.1 show the ideal case, which rarely occurs in nature, since surface roughness and also the composition of the target play an important role, especially if precise absolute sputtering yields are of importance [43–45].

As a good approximation the interaction of ions with solids can in most cases be reduced to a series of independent and elastic binary collisions.

2.2.1 Binary Elastic Collision

In the energy range used in this thesis the assumption of fully elastic collisions between two nuclei are fulfilled, as the mechanical energies in the keV/ion range are too low to ignite nuclear reactions. The principle of binary elastic collisions are well understood and give a good insight into the sputtering behaviour [46, 48, 55]. As these principles are also a basis for erosion modelling a short recap is given here.

Figure 2.2 shows the used reference frames, where the laboratory system (LS) and the center of mass system (CMS) are usually distinguished. In the LS the target atom (2 in figure 2.2a) is at rest. After the collision the projectile (1 in figure 2.2a) is scattered by the angle Θ, where the target undergoes a recoil angle of Φ. The same system transferred into the CMS (figure 2.2b) allows to define the CMS scattering angle ϑ and the impact parameter p. The CMS system has the advantage that the two body system can be reduced to the kinematics of a single particle with reduced mass [55].

(a) laboratory system   (b) center of mass system
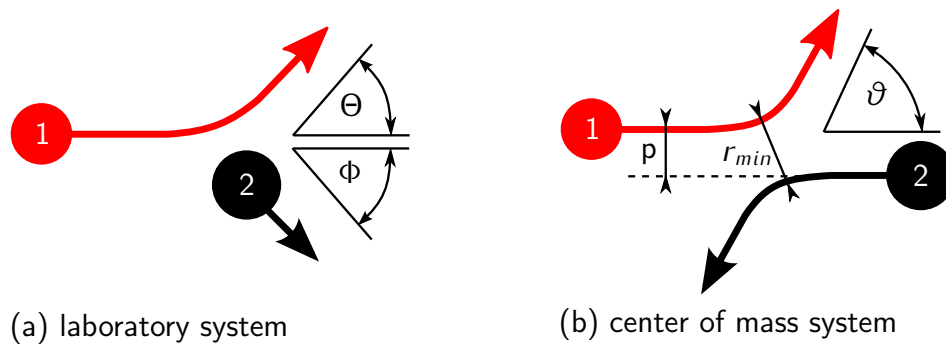
Figure 2.2 – Reference systems. In (a) the laboratory system can be seen, with the projectile (1) scattering angle Θ and the target (2) recoil angle Φ. In (b) the center of mass system (CMS) can be seen, introducing the impact parameter p and the scattering angle ϑ.

When energetic particles collide, an momentum transfer takes place. The maximum of the linear momentum and therefore kinetic energy can be transferred if the relation of masses of the two partners are close to 1 and becomes worse when the masses are very different, as can be seen in equation 2.2.2.

$$\frac{\Delta E}{E_{LS}} = \frac{4m_1 m_2}{(m_1 + m_2)^2} \, sin^2\left(\frac{\vartheta}{2}\right) \tag{2.2.2}$$

For $\vartheta = \pi$ this equation represents the ideal case of a direct knock on with an input parameter p equal to zero. ΔE represents the energy transfer from the projectile atom 1 to the target atom 2. m_1 and m_2 represent their corresponding masses and E_{LS} the total energy of the LS which is for the first collision equivalent to the kinetic energy of the projectile.

After a short calculation equation 2.2.2 can be transferred back into the LS, where the result can be seen in equation 2.2.3.

$$\frac{\Delta E}{E_{LS}} = \frac{m_2}{m_1} \frac{cos^2(\Phi)}{\left(1 + \frac{m_2}{m_1}\right)^2} \qquad (2.2.3)$$

The recoil angle Φ is limited to $\leq 90°$, because of linear momentum conservation. This concludes also that sputtering under normal incidence and a flat target needs at least two collisions to occur. Such an event is also called 'single knock-on regime'. If significantly more collisions are necessary to trigger sputtering, the process is called a linear collision cascade [46, 55].

The scattering angle ϑ can be evaluated by solving the scattering integral, which will be presented in the next section 2.2.2.

2.2.2 Classical Scattering Integral

As a basis for understanding the interaction of ion with solids the so called 'classical scattering integral' is very useful and is also the basis for modelling of sputter erosion [55, 56]. It follows from the assumptions made in section 2.2.1, were binary collisions are assumed. By including the inter atomic potential $V(r)$ as well as linear and angular momentum conservation, the classical scattering integral can be derived. (A precise derivation of the scattering integral can be found in references [46] or [55].) In equation 2.2.4 the formulation of this integral in the CMS can be seen.

$$\vartheta = \pi - 2p \int_{r_{min}}^{\infty} \frac{dr}{r^2 \sqrt{1 - \frac{V(r)}{E_{cms}} - \left(\frac{p}{r}\right)^2}} \qquad (2.2.4)$$

The variable ϑ represents the scattering angle of the projectile in the CMS, p the impact parameter, r the the distance between the two reactants, where r_{min} is the minimum distance that projectile and target atom can reach (compare with figure 2.2b), which also depends on the form of the potential $V(r)$ used. E_{cms} represents the total mechanical energy of the system and $V(r)$ the inter atomic potential, which is assumed to be spherically symmetric. Especially this potential is of high importance and needs to be chosen appropriately.

Very popular potentials are the Ziegler–Biersack–Littmark (ZBL) universal interaction potential and the Krypton-Carbon (KrC) interaction potential as they deliver good results for a wide range of projectile target combinations. Solving formula 2.2.4 is not straight forward and needs usually numerical methods. Here a very fast solving method is widely used, which is called the MAGIC integration formula. For more information about interaction potentials and solving the scattering integral the reader is refereed to references [46, 48, 55–59].

2.3 Sputtering of Rough Surfaces

Most theoretical descriptions and simulations of sputtering usually considers perfectly flat surfaces only [60, 61]. Such an assumption is, however, an idealization, and although it is possible to produce reasonably flat films for some materials, it often leads to discrepancies with the actual experimental conditions [43, 44, 62]. The deviations can be even more significant if the surface is additionally nanostructured [45]. In figure 2.3 a schematic sketch shows how the roughness and nanostructures of a surface can influence the sputtering process.
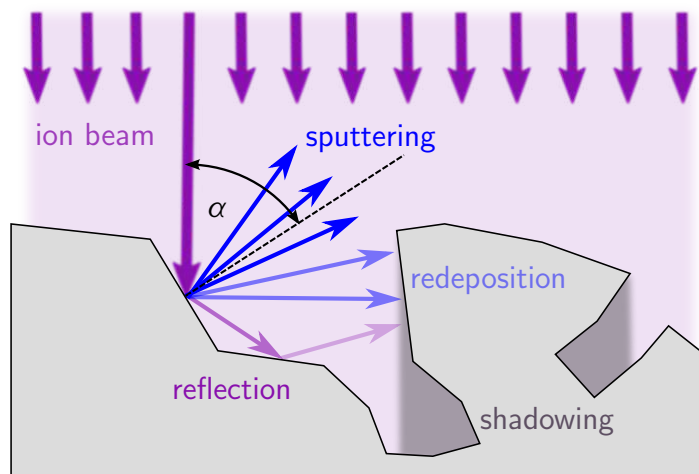
Figure 2.3 – Schematic sketch of a rough and nanostructured surface, hit by an ion beam. A global angle of incidence of 0° (normal incidence) does not correspond to the local angle of incidence α which is strongly dependent on the exact point of impact on the surface. Reflection of the projectiles can trigger further sputtering, whereby sputtered particles can also be redeposited. Nanostructures on the surface lead to shadowing of underlying structures and can enhance redeposition because the path to the surface is narrower. Figure adapted from [45].

An ion beam hits a target surface at a nominally 0° angle, which would be equivalent to normal incidence on a perfectly flat surface. However, due to the rough

surface condition the local angle of incidence α is different, with its value being strongly dependent on the exact point of incidence [44]. This fact already causes a different sputtering yield, as presented in figure 2.1b. The partially strongly varying angle of incidence α also leads to projectiles being reflected and hitting the surface a second time. Although the energy of the reflected projectile is lower than the incident energy, it could still be high enough to cause further sputtering. The angular distribution of sputtered particles is sometimes approximated by a cosine distribution [54]. Different experiments revealed, that the sputtering yield as a function of emission angle β can be better described by a $cos^y(\beta)$ distribution, with a parameter y greater than 1 [48].

Figure 2.3 indicates also, that not all of the sputtered atoms can escape the surface, as they hit other parts of the morphology and may be redeposited there or are even reflected with a certain probability. Evidently, all these effects show clearly that a theoretical description of the sputtering of rough surfaces becomes extremely complex.

Küstner et. al. tried to use scanning tunnelling microscope (STM) images as input for a simple model to describe redeposition effects and achieved very good results [63, 64].

To get a better understanding of the erosion behaviour of rough surfaces, numerical methods, especially modelling methods, are of increasing importance. High performance and cluster computing in combination with new developed codes allows to model the erosion of nearly any target and will be presented in the next chapter 3.

3

Sputter Modelling

This chapter presents the sputter modelling codes used in this thesis and summarizes their basics. After a short introduction (section 3.1) the modelling approach of choice will be presented (section 3.2). This is followed by an overview of the common available MC-BCA codes (section 3.3) and their surface morphology sensitive extensions in 2D and 3D (section 3.4).

3.1 Introduction

Computer simulations of sputtering are of great importance to get a better understanding of fusion relevant ion surface interactions. Next to modelling of the erosion behaviour of a PFM also sputtered and scattered particles distribution are of interest. Furthermore investigations of the projectile range in matter as well as implantation of the fusion fuel into a PFM are of great importance.

Different modelling approaches are available for ion surface interactions. A simple and well established approach is the molecular dynamics (MD) technique. Here every target atom in a modelled sample is placed in an appropriate interaction potential and then a projectile atom shot on it, with a certain kinetic energy E_{kin} and impact angle α. The impact of this projectile ignites collision cascades. Every trajectory is calculated continuously, by solving Newton's equation of motion and also the interaction potential updated, according to the target atoms actual position. This numerical manybody interaction approach lead to precise results, but needs also a lot of computation time. The chosen timesteps to solve Newton's equation of motion need to be very small (typically $10^{-15}\,\mathrm{s}$) and a huge amount of atoms (at least 10^6) needs to be calculated in order to get realistic

results [65]. This approach is suitable for timescales in the sub-second range, but for modelling erosion effects of fusion relevant materials, which are exposed to high fluences over a days and months, the MD modelling approach is not feasible. Alternatively, fast sputter modelling can by done by using the so called monte carlo (MC)-binary collision approximation (BCA) approach, which will be presented in more detail hereinafter.

3.2 The Monte Carlo - Binary Collision Approximation

The BCA approach models the history of the incident projectiles and the development of the collision cascades as a series of binary collisions. An illustration of such a collision cascade can be seen in figure 3.1.
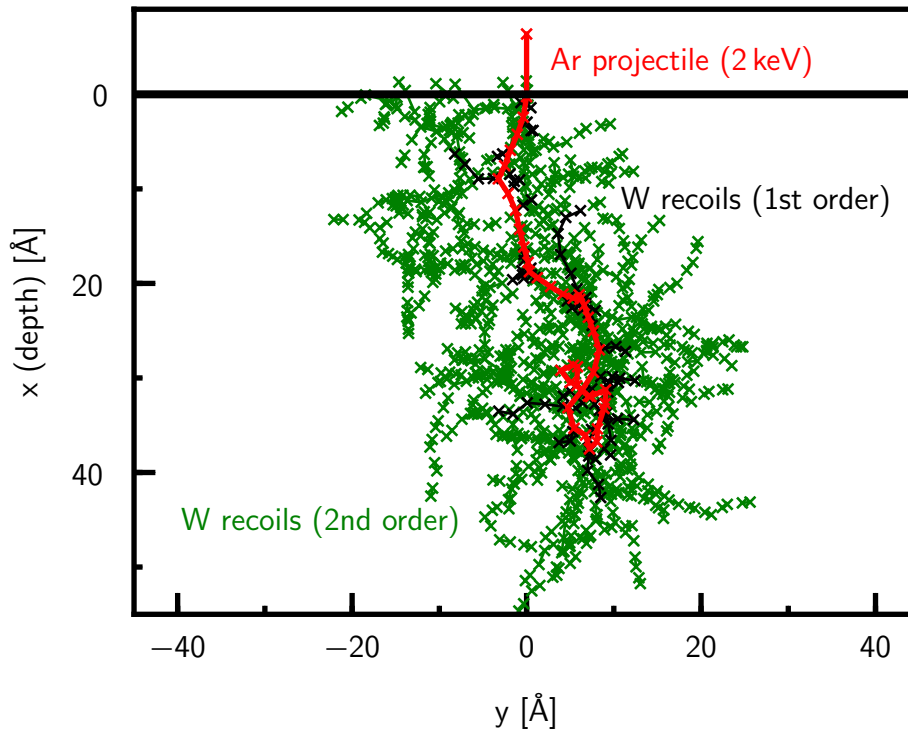
Figure 3.1 – An exemplary Ar on W collision cascade, at $2\,\text{keV/Ar}$ under normal incidence, modelled with SDTrimSP. The red line shows the history of the Ar projectile above and inside the W target. The black trajectories represent the W recoils, directly scattered with the projectile (1st order) and the green trajectories the W recoils scattered with other W recoils (2nd order). Above the surface line ($x = 0\,\text{Å}$) 5 W recoils are visible, which are sputtered during this cascade.

For modelling these two-body collisions the classical scattering integral, with the impact parameter p is solved (compare with section 2.2.2). Between two collisions the projectile is assumed to travel on straight paths, where the length of this path and the impact parameter of the next collision event is randomly chosen, according to a probability distribution which depends on the density of the target. Different models of electronic stopping can be included too. Every atom involved in the collision cascade is followed until its kinetic energy drops below a certain value, where it is considered as stopped, in order to avoid unnecessary long calculation times. If an atom or the projectile reaches the surface and its momentum perpendicular to the surface $p_\perp$ is sufficient to overcome the surface binding energy E_{SB} (equation 3.2.1), it is considered as sputtered (or scattered in the case of the projectile).

$$\frac{p_\perp^2}{2m} > E_{SB} \tag{3.2.1}$$

The surface binding energy E_{SB} is a crucial input parameter. As surface binding energy E_{SB} of mono-atomic targets the sublimation energy is usually used. Only for a few mixed or compounded target literature data are available (for example reference [66]). For other targets with mixed elements, the surface binding energy can be approximated as a concentration-dependent mean value of the individual binding energies, which usually leads to good results. This can also be too low in cases of oxides, a fact that needs to be taken into account [44].

The MC-BCA modelling approach allows very fast sputter modelling, because a complex many-body problem is simplified to many binary collisions, which are easy to calculate. The implementation of this method usually uses the principle of "pseudoatoms" as projectiles, each representing a certain number of real projectiles. A higher statistical accuracy can be achieved with a high pseudoatom number, but at the cost of computation time. For a more detailed review of its principle the reader is referred to [57, 58, 67–69].

3.3 Overview of Common MC-BCA Codes

Various implementations of the MC-BCA principle are available today. The most well known one is "Stopping and Range of Ions in Matter (SRIM)", by Ziegler et al. [57], because of the useful graphical user interface (GUI) and its good documentation. It uses the ZBL universal interaction potential [57] and for fast solving the scattering integral the MAGIC formula is used [58]. SRIM allows also to include elemental depth distributions of a sputter target (1D), but dynamic changes and fluence dependent effects cannot be modelled with this entirely static approach. Therefore "Dynamic Transport of Ions in Matter (TRIDYN)" by Möller et al. was developed, which allows modelling of ion implantation, atomic mixing and also

preferential sputtering [68, 69]. It uses also the MAGIC formula for solving the scattering integral, and uses the KrC interaction potential [59, 68, 69]. The dynamic approach was implemented by subdividing the target in depth-dependent layers with different elemental composition. After certain projectile history calculations the density of the layers are checked and if it gets to low, the residual material will flow into the underlying layer, resulting in a vacuum layer. Projectile implantation can also be included and can cause a swelling of the target, creating additional layers [68].

Alternatively "Static and Dynamic TRIM Sequential and Parallel (SDTrimSP)" is available, developed by Mutzke et al. [60, 70]. This modelling approach is extremely flexible, because integration method, interaction potential, screening function and model of electronic stopping can be selected appropriately. In addition, every parameter used can be inspected and, if necessary, adapted [60, 71]. Recent developments allow also including thermal induced material diffusion effects [70].

3.4 Surface Morphology Sensitive Modelling

In chapter 3.3 the most common MC-BCA codes were presented, which allow modelling of static as well as dynamic changes of a sputter target, but are limited in modelling in one dimension (depth). Therefore, only the modelling of flat surfaces is possible, so that effects caused by rough surfaces or nanostructures cannot be considered. For this reason new codes were developed which can include surface morphologies.

SDTrimSP-2D represents a first attempt to include surface effects. The layers were subdivided here in rectangular cells in one lateral direction with a defined elemental composition or as vacuum. In the dynamic mode of this code these cells can shrink or swell, which allows modelling of dynamic morphology changes of a line surface [72, 73].

In order to include the influence of realistic surface morphologies, which may have complex shapes or even nanostructures, an extension into the third dimension is unavoidable.

"TRI3DYN" by Möller et al. [74] represents an enhanced version of TRIDYN [69] and is able to model realistic 3D surfaces. In TRI3DYN the layer principle has been extended in the third dimension by using small cubic volumes (so called voxels) with a predefined elemental density, or vacuum. By stacking many of these voxel-cubes on top of each other almost any surface including substructure can be created and modelled. An expansion of SDTrimSP in 3D (SDTrimSP-3D) follows a similar approach, but is still under development [75].

The size of this voxel is an additional important parameter and should be at least smaller than the expected length of the collision cascade to avoid falsifications

22

caused by discretising a real surface. On the other hand, a large number of voxels considerably increases the computing time, so that the lateral expansion of the object to be modelled is limited [43, 44, 75].

A high importance of the three dimensional dynamic erosion modelling is given to the relaxation procedures of every single voxel. After a certain amount of calculated pseudoatom histories the elemental density of every voxel is verified. If it becomes to high, material will flow into an adjacent voxel which has a lower density. Inversely, if the density becomes too low, the rest of the material flows into an neighbouring voxel and the original voxel changes to a vacuum voxel.

For a more detailed explanation of the relaxation procedures and the precise function of the TRI3DYN code, the reader is referred to [68, 69, 74].

4

Experimental Methods

The contents of the following chapter have been partially
published in references [43–45] or are in preparation for publishing.

This chapter presents the experimental techniques and laboratory setup configurations used for this thesis. After a detailed explanation of the TU Wien QCM technique (section 4.1) and the dual mode technique, developed during this thesis (section 4.1.2), the measurement principles in different configurations are shown (section 4.1.3, 4.1.4). Subsequently, the sample analysis techniques are described (section 4.2).

4.1 The TU Wien Quartz Crystal Microbalance Technique

A QCM is based on the the piezoelectric effect and allows measuring mass changes with high precision. This is based on the fact, that the resonance frequency of a quartz can be measured very precisely [76–78]. It is used nowadays as device to monitor thin film growth in material deposition applications or it can also be used the other way round, to evaluate the recession of thin films in order to evaluate sputtering yields [79].

Sauerbrey in 1959 developed the fundamentals of the QCM technique. The basis for this is the fact that the resonance frequency of a quartz crystal is dependent on the thickness of the crystal itself plus the thickness of any layer on top of it [76]. Sauerbrey found out, that a relative change of thickness $\Delta d/d$ is proportional to a relative change in the resonance frequency $\Delta f/f$, which is in turn directly proportional to a relative change in mass $\Delta m/m$, as can be seen in equation 4.1.1.

25

$$-\frac{\Delta f}{f} = \frac{\Delta d}{d} = \frac{\Delta m}{m} \tag{4.1.1}$$

Equation 4.1.1 holds true for film thicknesses significantly thinner than the quartz thickness. Usually this is a difference in size of 3 orders of magnitude, therefore the initial mass m can be assumed to be the mass of the quartz itself [76].

Quartz crystals are also very sensitive to temperature, stress and pressure variations, which need to be taken into account in order to reach a high sensitivity. On the other hand, quartz sensors can also be used to measure these quantities [77, 80–82].

The Sauerbrey equation 4.1.1 can be extended to be able to evaluate mass change rates, by including the time derivative of the frequency, as can be seen in equation 4.1.2.

$$\frac{\Delta m}{\Delta t}\,[\mathrm{amu/s}] = -\frac{m_0}{f_0}\frac{\Delta f}{\Delta t} \tag{4.1.2}$$

f_0 and m_0 represent the initial resonance frequency and the initial mass of the quartz crystal (in atomic mass unit (amu)). The TU Wien QCM allows in situ measurements of mass changes, therefore this form of representation is more suitable.

In order to evaluate sputtering yields by particle bombardment information of the projectile beam need to be included in equation 4.1.2. This is done by including the projectile flux Φ and the surface area of the quartz sample A_q, wherefrom the sputtering yield Y can be determined, according to equation 4.1.3 [79, 83].

$$Y\,[\mathrm{amu/projectile}] = -\frac{1}{\Phi A_q}\frac{m_0}{f_0}\frac{\Delta f}{\Delta t} \tag{4.1.3}$$

In order not to have to consider the non-uniform radial sensitivity of the quartz disc, care must be taken to distribute the projectile flux evenly over the entire surface of the quartz sample [79, 83].

4.1.1 Electronics

The highly sensitive QCM electronics was originally developed by M.Schmid [78] at TU Wien and is described in detail in Hayderer et. al. [79]. It allows to measure the resonance frequency of a quartz crystal at around $6\,\mathrm{MHz}$ up to a precision of some mHz. The precision is limited by a quartz drift of about $2\,\mathrm{mHz}$ and a noise of the electronics of about $5\,\mathrm{mHz}$. This allows to measure mass changes in the order of $10\,\mathrm{pg/s}$, which is equivalent to about $10^{-4}\,\mathrm{W}$ monolayers/s [79, 83]. During this thesis the electronics setup has been improved in order to be able to excite overtone modes as well as to reduce the size of the whole setup.
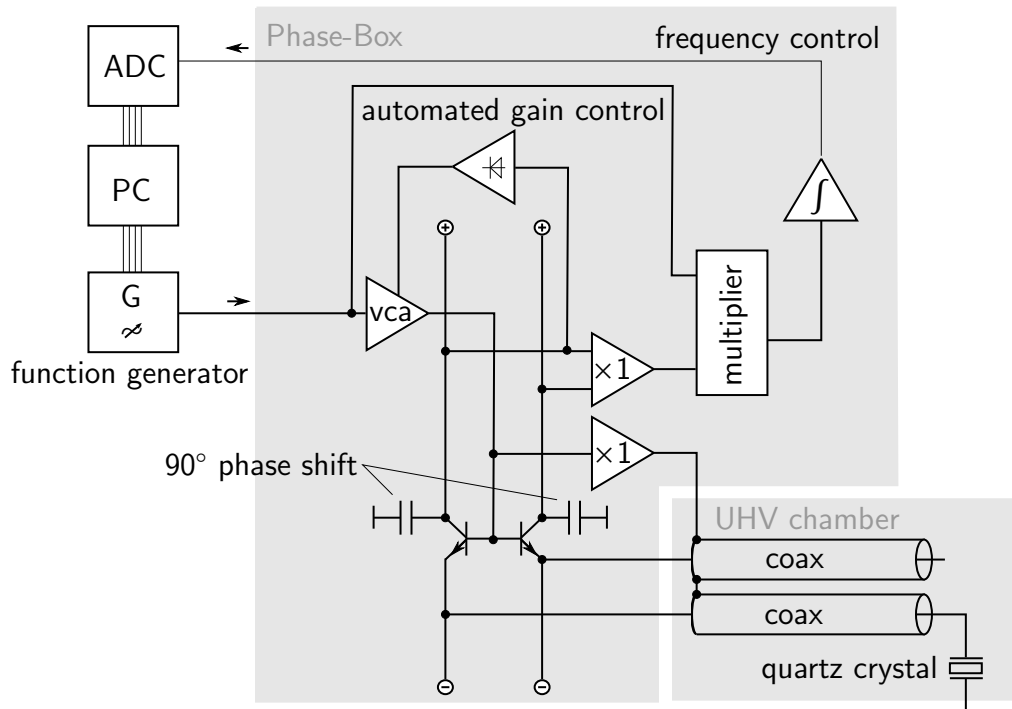
Figure 4.1 – QCM electronic schematics. A so called Phase-Box checks the fed-in frequency from a function generator if it deviates from the resonance frequency of the quartz crystal and adjusts a frequency control output accordingly. This output is read via an analog digital converter (ADC), connected to a personal computer (PC). A controlling script on this PC then adjusts the function generator output frequency to keep the quartz crystal exactly in resonance. Figure adapted from [79].

Figure 4.1 shows the schematics of the QCM electronics, driving the quartz crystal at its resonance frequency. The quartz crystal is operated in series resonance, in its fundamental mode at around 6 MHz. The so called Phase-Box includes the main parts of the driving electronics and is located outside the UHV chamber. Electrical feedthrough in combination with a high quality UHV coaxial cable (coax) connect the quartz crystal sample to the Phase-Box. A precise sine wave is generated by using a PC controlled function generator and is fed into the Phase-Box. The electric circuit in the Phase-Box checks if this frequency is the resonance frequency of the quartz crystal, by using a phase comparison technique between current and voltage. In resonance the phase shift is zero, leading to a zero voltage output of the frequency control. In any other case the frequency control output is increasing or decreasing, meaning that the actual supplied frequency is too high or too low. A more precise explanation of the function of the Phase-Box circuit can be found in [79].

The frequency control output voltage is read by using a fast ADC and forwarded to the PC. Thereafter a controlling script written in Python adjusts the function generators output frequency to the control voltage input, to keep the quartz crystal exactly in resonance.

Hayderer et. al. used an voltage controlled oscillator for feeding the sine wave voltage to the Phase-Box. The actual resonance frequency was then measured by using a frequency counter [79]. Unfortunately both of these devices are quite large. By replacing these by a high precision and PC controlled function generator the size of the whole QCM electronics could be reduced and allows more flexibility. The function generator can be read by a digital interface, making the use of an frequency counter unnecessary. Furthermore the operational frequency range is not limited any more to $5.9 - 6.1\,\mathrm{MHz}$, allowing for the first time operating the TU Wien QCM in overtone modes, up to $20\,\mathrm{MHz}$. The use of a PC as controlling device also allows a quasi simultaneous operation of two or more frequency modes. This technique will be presented in more detail in chapter 4.1.2.

The high sensitivity of the TU Wien QCM is also due to the use of high quality stress compensated (SC-cut) quartz crystals. This quartz type has a lower sensitivity to thermal and mechanical stress, compared to the most commonly used AT-cut quartz crystals [77, 79]. The TU Wien QCM uses plano-convex SC-cut quartz crystal resonator discs with the product specification XA-3641 from company KVG Quartz Crystal Technology GmbH [84]. A thickness of about $0.3\,\mathrm{mm}$ lead to a precise fundamental mode frequency of $6\,\mathrm{MHz}$. In figure 4.2 an image of a typical quartz crystal sample can be seen.
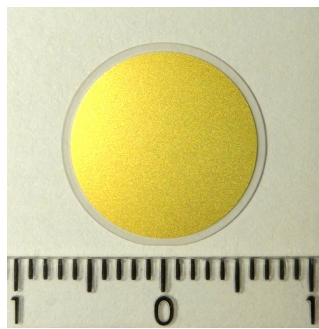

Figure 4.2 – Image of a typical SC-cut quartz crystal disc used in the QCM. The crystals have a diameter of $14\,\mathrm{mm}$ with gold electrodes of a thickness of $140\,\mathrm{nm}$ on both sides. A quartz thickness of $0.3\,\mathrm{mm}$ lead to a fundamental mode frequency of $6\,\mathrm{MHz}$.

4.1.2 Dual Mode Technique

The new TU Wien QCM electronic setup, developed during this thesis, allows to excite any quartz crystal modes up to $20\,$MHz. Of interest are the main C-modes only, due to its radially symmetric oscillation form [77, 78]. The C-1 main mode is the resonance frequency used in the single mode technique, as described in reference [79]. Due to the huge frequency range of the used function generator, care must be taken not to excite any secondary modes of the quartz crystal, which have a different sensitivity to mass and temperature changes [77, 78]. The principle used is described in section 4.1.2.1. Only odd overtone modes are excitable, therefore the second mode of interest is the C-3 mode. The C-1 and C-3 modes have the same sensitivity to mass changes, but a different response to changes in temperature. By knowing the frequencies of both modes, a temperature insensitive QCM can be realized [80]. The technique used is described in section 4.1.2.2.

4.1.2.1 Principle of Dual Mode Controlling

The improved TU Wien QCM technique quasi simultaneously excites the ground mode (C-1 mode) and the third overtone mode (C-3 mode) of a quartz crystal sample. Every 5 seconds a software controller switches a sine-wave frequency generator between both frequencies. The ground mode frequency can be measured up to a precision in the mHz range, while the 3rd overtone mode is limited to about 100mHz, due to increased noise and damping at this frequency range of the electronics.

The frequency control output of the Phase-box allows a simple and linear controlling (as described in chapter 4.1.1), but only in a small frequency range. The C-1 mode frequency can be found rather easily, because of the very strong response of the SC-cut crystal in this frequency range. Here the Phase-box and the controller are able to find the precise resonance frequency over a starting frequency range of $\Delta f \approx 100$kHz [79].

In contrast it is more difficult to find the C-3 mode frequency, because the resonance response is lower and the frequency damping of the electronics higher. Furthermore the risk of exciting secondary modes is high [64, 77, 78]. The frequency range for C-3 mode controlling is smaller and only in the range of about $\Delta f \approx 20$kHz. This means the position of the frequency of the third mode need to be 'guessed' as good as possible before starting operating the dual mode QCM. According to a theoretical model of M. Schmid the resonance frequencies of a quartz crystal can be calculated by [78]:

$$\omega_m^{(n)} = \frac{m\,\pi}{\alpha^{(n)}d}\left(1 - \frac{4(k^{(n)})^2}{m^2\pi^2}\right) \tag{4.1.4}$$

Where m is the main mode-number ($m = 3$ means third overtone mode and only odd overtones are exciteable), n the number of the secondary mode (in our case $n = 1$), d the thickness of the quartz, α the inverse phase speed ($1/\alpha = 3600$m/s) and k is a coupling constant (($k^{(n)})^2 = 0.024$ in C mode) [78, 79]. With this and by knowing the C-1 mode frequency f_1, the frequency position of the C-3 mode at room temperature can be estimated as:

$$f_3[\,\text{Hz}] \approx 3f_1 - 1.6 \times 10^5 \qquad (4.1.5)$$

This approximation allows guessing the third overtone C mode frequency within a range of 20kHz and is accurate enough for the QCM controller to lock on the precise frequency. It is noted, that the C-3 mode frequency is below three times the C-1 mode frequency, which allows to define an upper limit for the controller and avoids exciting unwanted B mode resonance frequencies [78].

4.1.2.2 Dual Mode Temperature Compensation

The resonance frequency of a quartz crystal is extremely sensitive to changes in temperature, which causes difficulties in separating the change in the resonance frequency due to mass change and due to temperature change. A common way is to operate the quartz crystal in its fundamental mode at an elevated temperature, at its frequency versus temperature minimum (compare with figure 4.3). Here a slight change in temperature causes only very small changes in the resonance frequency [42, 79, 83].

In order to perform temperature programmed thermal desorption spectroscopy (TDS) measurements with a QCM the change in resonance frequency due to a change in temperature cannot be neglected any more. The C-1 and C-3 modes of a quartz crystal have the same sensitivity to mass changes (as can be seen in figure 4.8), but a different response to changes in temperature. By knowing these two frequencies a temperature compensation can be realized, as reported in [80]. Figure 4.3 shows a typical temperature dependence of a SC-cut quartz crystal, of the C-1 mode (f_1) and the C-3 mode (f_3). The C-3 mode shows a saddle point temperature at $360\,\text{K}$, while the C-1 mode a minimum at $435\,\text{K}$. Further increasing the temperature lead to a strong increase in both resonance frequencies.

By defining the so called beat-frequency f_b, according to equation 4.1.6 a nearly linear dependence on the real temperature itself can be seen (compare with figure 4.4). Due to the linear response this frequency can be used as a quartz internal temperature equivalent [80].

$$f_b = 3f_1 - f_3 \qquad (4.1.6)$$

30
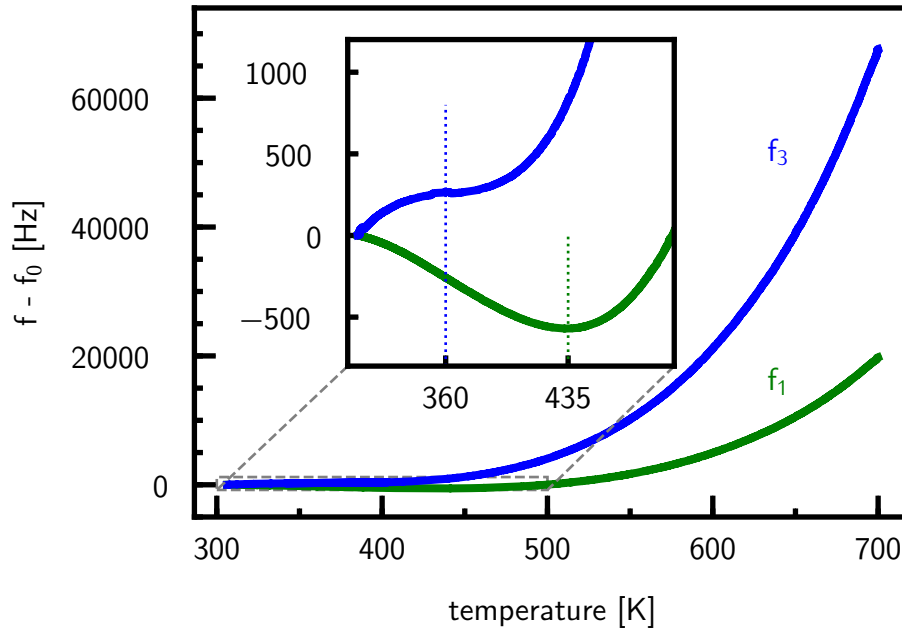
Figure 4.3 – The temperature response of the C-1 fundamental mode f_1 and C-3 overtone mode f_3 of a Be coated quartz crystal sample. While the fundamental mode shows a minimum at $435\,\mathrm{K}$, the third overtone mode shows a saddle point at $360\,\mathrm{K}$, as can be seen in the zoom box.
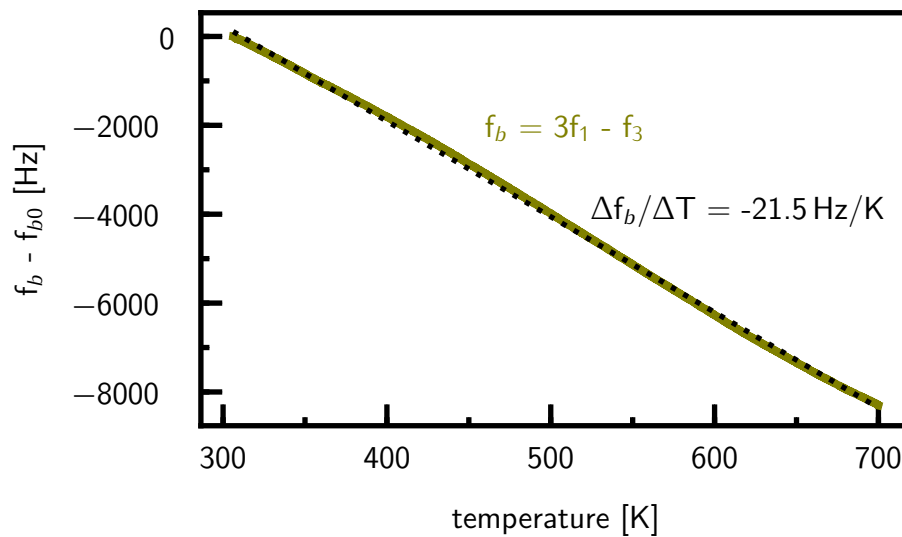
Figure 4.4 – The beat frequency f_b of a Be coated quartz crystal sample, measured from room temperature to $700\,\mathrm{K}$. A nearly linear behaviour can be seen. The dotted line shows a linear fit with a slope of $\Delta f_b/\Delta T = -21.5\,\mathrm{Hz/K}$.

In order to perform the temperature compensation, the famous Sauerbrey equation (equation 4.1.1) needs to be extended including also temperature changes, as can be seen in 4.1.7 and 4.1.8.

$$\frac{\Delta f_1(m, T)}{f_{10}} = \frac{\Delta f_1(m)}{f_{10}} + \frac{\Delta f_1(T)}{f_{10}} = -\frac{\Delta m}{m_0} + \frac{\Delta f_1(T)}{f_{10}} \qquad (4.1.7)$$

and:

$$\frac{\Delta f_3(m, T)}{f_{30}} = -\frac{\Delta m}{m_0} + \frac{\Delta f_3(T)}{f_{30}} \qquad (4.1.8)$$

This expansion includes both modes and the temperature dependence (index 1 for ground mode and index 3 for 3rd overtone mode, where '10' and '30' means initial frequency at room temperature).

Due to the nearly linear temperature dependence of the beat frequency, f_b can be used as a temperature equivalent. A separate frequency versus temperature measurement is nevertheless necessary, where no mass change occurs in order to calibrate the frequency versus beat-frequency behaviour. A polynomial of degree 5 can than be used to fit this separate measurement for both eigenfrequencies, according to equations 4.1.9 and 4.1.10.

$$f_1(T) \Rightarrow f_1(f_b) = \sum_{i=0}^{5} a_i \times (f_b)^i \qquad (4.1.9)$$

$$f_3(T) \Rightarrow f_3(f_b) = \sum_{i=0}^{5} b_i \times (f_b)^i \qquad (4.1.10)$$

Combining equations 4.1.7, 4.1.8, 4.1.9, 4.1.10 and expanding to mass change rate finally leads to a temperature compensated mass change rate:

$$\frac{\Delta m}{\Delta t} \, [\text{amu/s}] = -\frac{m_0}{2} \left[\frac{1}{f_{10}} \left(\frac{\Delta f_1}{\Delta t} - \frac{\Delta f_1(f_b)}{\Delta t} \right) + \frac{1}{f_{30}} \left(\frac{\Delta f_3}{\Delta t} - \frac{\Delta f_3(f_b)}{\Delta t} \right) \right] \qquad (4.1.11)$$

In principle a temperature compensated mass change rate can also be realized by combining only equations 4.1.7 and 4.1.9 or only equations 4.1.8 and 4.1.10, but an average over both modes can further increase accuracy.

Absolute temperature measurements of a quartz sample, e.g. with a thermocouple, have the disadvantage that it cannot be measured directly on the quartz crystal, but only on the sample holder. This causes always a shift between the real temperature of the quartz sample and the measured temperature via thermocouple. The beat-frequency instead is directly measured at the quartz crystal sample and allow a more precise temperature information. In principle this dual mode technique makes measurement of the temperature, e.g. by means of thermocouple, not absolutely necessary any more, if absolute values are not important [80].

4.1.3 Classic Configuration

This chapter presents the classic configuration ot the TU Wien QCM technique in order to evaluate sputtering yields. In this configuration the quartz samples are directly hit by the primary particle beam. A thin film of sample material is deposited on one side of the electrodes of a quartz crystal sample, by using physical vapour deposition (PVD), like magnetron sputter deposition or thermionic vacuum arc (TVA) techniques [85–87]. Thin film thicknesses of some 100 nm are used in the classic QCM configuration, to fulfil equation (4.1.1). In figure 4.5 the schematics of the classic QCM configuration can be seen. A well defined ion beam hits the surface of the quartz crystal disc under an angle of incidence α and causes sputtering of the thin film, scattering as well as implantation into the film. The resulting total change in mass can than be measured as a change in the resonance frequency of the quartz crystals, according to equation 4.1.1.
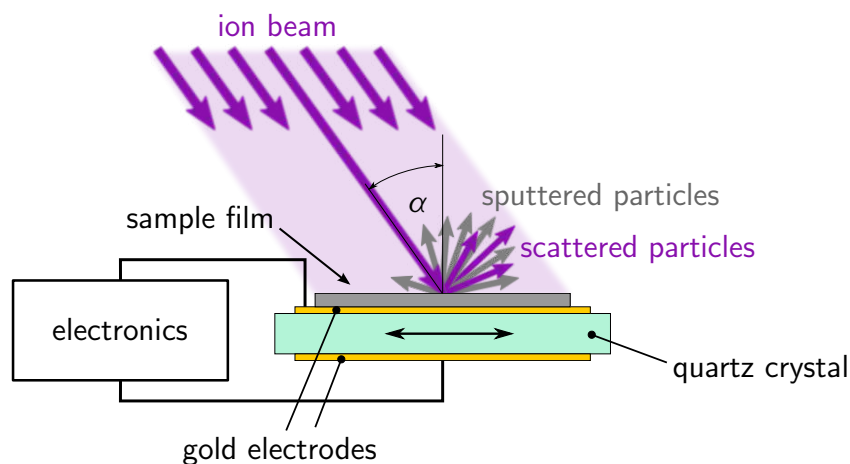
Figure 4.5 – QCM schematics in classic configuration. A quartz crystal disc is operated in thickness shear mode (ground or overtone mode). On both sides gold contacts provide good electrical conductivity to the electronics, which ensure that the crystal oscillating at its resonance frequency. On one side of the electrodes a thin film of the sample material is deposited. A scanned projectile beam hits this film under an angle of incidence α causes sputtering of the thin film material, scattering but also deposition/implantation of the projectiles. The resulting total mass change can then be measured as a change in the resonance frequency of the crystal.

The ion beam needs to be scanned uniformly over the whole sample surface to avoid inaccuracies, caused by the radial sensitivity of the quartz crystal. The influence of the projectile beam diameter to the total sensitivity of the QCM was evaluated by Dobeš et.al. [88] and Berger et.al. [89]. Above a critical beam diameter of $7\,\text{mm}$ the sensitivity of the quartz crystal becomes independent of the beam size. A beam diameter of $5\,\text{mm}$ reduces the sensitivity of the quartz to about 90% [89].

Figure 4.6 shows a 3D computer aided design (CAD) drawing of the sample holder used in this thesis, originally designed by B. Berger [89]. It is separated in two sections: The upper part consists of a Faraday cup with secondary electron suppressor and precise aperture, which allows a precise ion beam analysis. The lower part includes the quartz crystal sample and an ohmic heating system, to operate the sample at elevated temperatures or for TDS measurements. A K-type thermocouple (TC), mounted laterally on the sample holder, allows to evaluate the temperature.
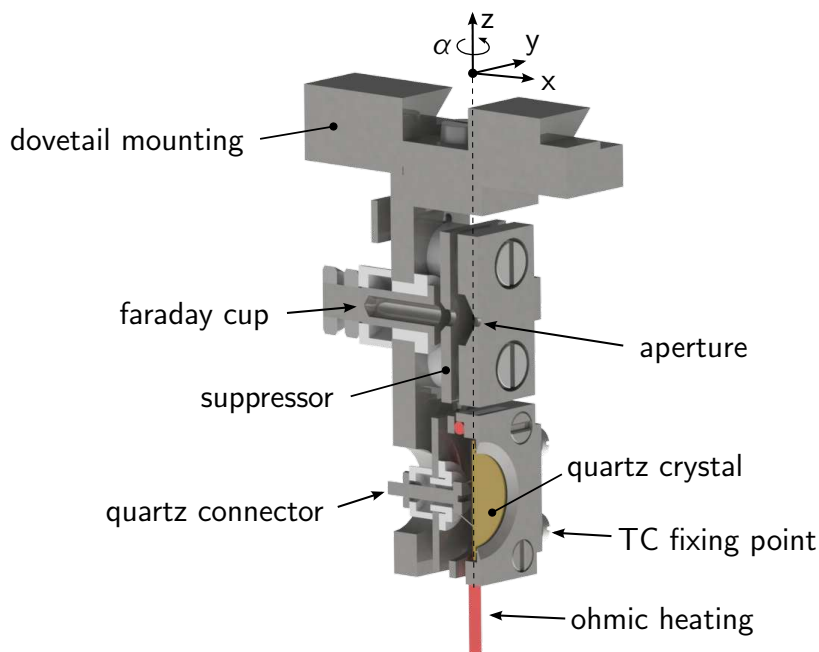
Figure 4.6 – QCM sample holder. This sectional drawing through the symmetry plane reveals it's main parts. It is separated in two sections: I: A Faraday cup with secondary electron suppressor and precise aperture for ion beam analysis. II: The quartz sample holder including an ohmic heating equipment. A K-type TC is mounted on one side of the holder. Both sections are accessible by linear movement of the sample holder in the z-direction. The dashed line indicate the rotation axis α, which runs exactly through the center of the quartz sample as well as the aperture of the Faraday cup.

Figure 4.7 shows a 3D-CAD drawing of the whole experimental setup, built and used during this thesis. High vacuum conditions are ensured by using a ConFlat (CF) flange system in combination with turbomolecular pumps and ensure a base pressure of 10^{-9} mbar after baking. Different electron impact ion sources were used during this thesis, where the latest setup is shown in figure 4.7. The ion sources provide energy ranges from $E_{kin} = 100$ eV $- 5$ keV up to a flux of $\Phi \approx 10^{18}$ m^{-2}s^{-1}.
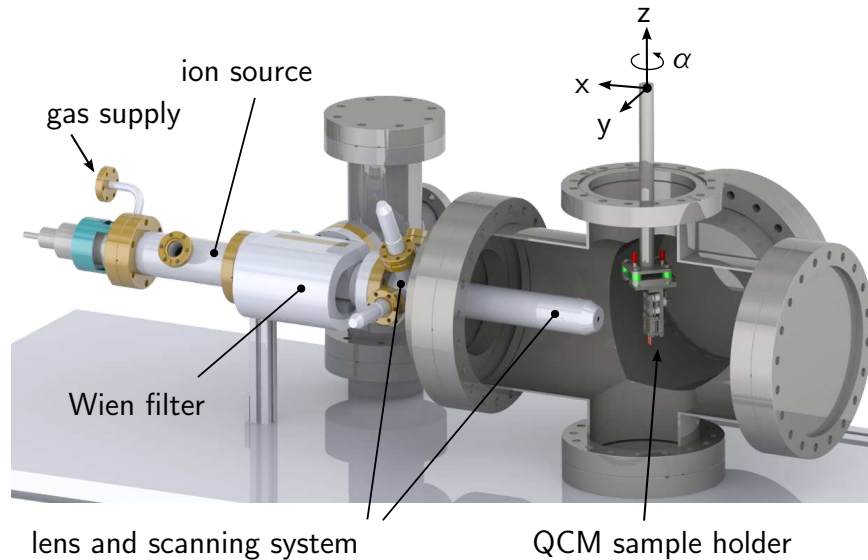
Figure 4.7 – Experimental setup. This 3D-CAD drawing shows the whole experimental setup built up during this thesis. A CF flange system in combination with turbomolecular pumps ensure a base pressure of 10^{-9} mbar. A sputter ion source (Specs IQE 12/38 with Wien filter) provides a mass separated ion beam, with a maximum flux of $\Phi \approx 10^{18}$ m^{-2}s^{-1}. The included lens and scanning system allows aligning and forming of the ion beam. A XYZα manipulator allows precise positioning of the sample holder.

4.1.3.1 Measurement Procedure

By using a Faraday cup, embedded in the sample holder (see figure 4.6), the ion beam shape and flux Φ is evaluated. The ion current I in the Faraday cup is read by using a Keihtley 6485 picoamperemeter. Including the charge state of the ion beam q and the size of the Faraday cup aperture A_{FC} the ion beam flux Φ is

evaluated, according to equation 4.1.12:

$$\Phi = \frac{I}{A_{FC}\ e\ q}\ cos(\alpha) \qquad (4.1.12)$$

where e corresponds to the elementary charge. By lateral displacement of the sample holder in y and z direction in mm steps, the shape of the ion beam is measured. The ion beam is adjusted so that the ion current fluctuates less than 10% over the entire scanning range. Any deviations are included in the error estimation. The Faraday cup can only be used under normal incidence, therefore the desired angle of incidence α for the sputtering measurements must be included in the ion beam flux evaluation.

After successful adjustment of the ion beam, the quartz sample (see figure 4.6) is moved into the ion beam and the frequency change evaluated. Since during irradiation of the sample no measurement of the ion beam is possible, the ion beam flux is checked before and after every irradiation step. For sputtering yield evaluation, according to formula 4.1.3 both ion flux measurements are averaged and assumed to be constant during irradiation. Any deviations between both ion flux measurements are included in the error estimation as maximum error propagation.

Figure 4.8 shows a QCM sputtering yield measurement, where an Ar^+ ion beam with an energy of $E_{kin} = 500\,eV$ hits a Au quartz sample under normal incidence. During the beam on phase ($t = 200\,s - 800\,s$) a constant rise in the resonance frequency can be seen, which is equivalent to a mass loss, according to equation 4.1.1. By including the ion beam flux Φ the sputtering yield Y can be calculated.

Using the fundamental mode lead to a sputtering yield of $Y_{C1} = 2.72 \pm 0.18\,Au/Ar$ and by using the or the third overtone mode a sputtering yield of $Y_{C3} = 2.70 \pm 0.17\,Au/Ar$ could be measured. Both modes provides very similar sputtering yields, but absolute changes in the resonance frequency are three times higher in using the third overtone mode. This result also shows very nicely that Sauerbreys equation 4.1.1 holds also true for the third overtone mode.
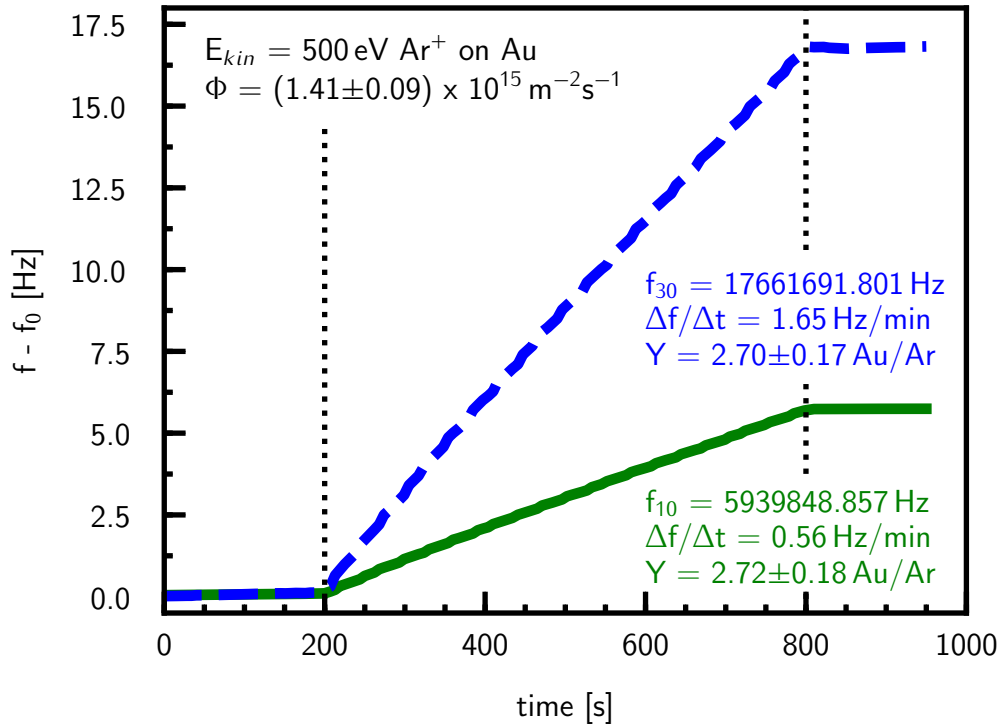
Figure 4.8 – QCM Ar on Au sputtering yield measurement, showing the frequency response over time. A kinetic energy of $500eV$ was used to bombard an Au coated quartz crystal under normal incidence. The ion beam was activated at $t = 200\,s$ and deactivated at $t = 800\,s$, where a continuous increase of the resonance frequency of the fundamental (C-1) mode (green solid line) as well as the 3rd overtone (C-3) mode (blue dashed line) is visible. The slope $\Delta f/\Delta t$ during the beam-on phase and the ion beam flux Φ is used to evaluate the sputtering yield Y.

4.1.4 Catcher Configuration

In the catcher configuration the quartz sample is used to capture sputtered particles, originating from a sample, which is hit by a particle beam. This technique allows to perform sputtering experiments with nearly any targets. A big advantage here is that the sample material no longer has to be deposited directly onto the quartz crystal and therefore thicker samples with high roughnesses can be examined. Also direct measurement of sputtered particles distributions is possible with this technique. On the other hand data evaluation is more difficult compared to the classic configuration, presented in section 4.1.3 [90].

The setup configuration is identical as shown in figure 4.7. Except in the catcher configuration the sample holder is used to hold an arbitrary sample, which fits into it. Additionally a catcher-QCM is mounted on the side, as can be seen in

figure 4.9. The surface of the catcher-QCM is aligned parallel to the ion beam (x-axis in figure 4.9 and 4.7). The distance d from the catcher-QCM surface to the center of the sample holder, as well as the relative position Δx from the center of the catcher-QCM to the center of the sample holder can be adjusted by manipulators (compare with figure 4.9).
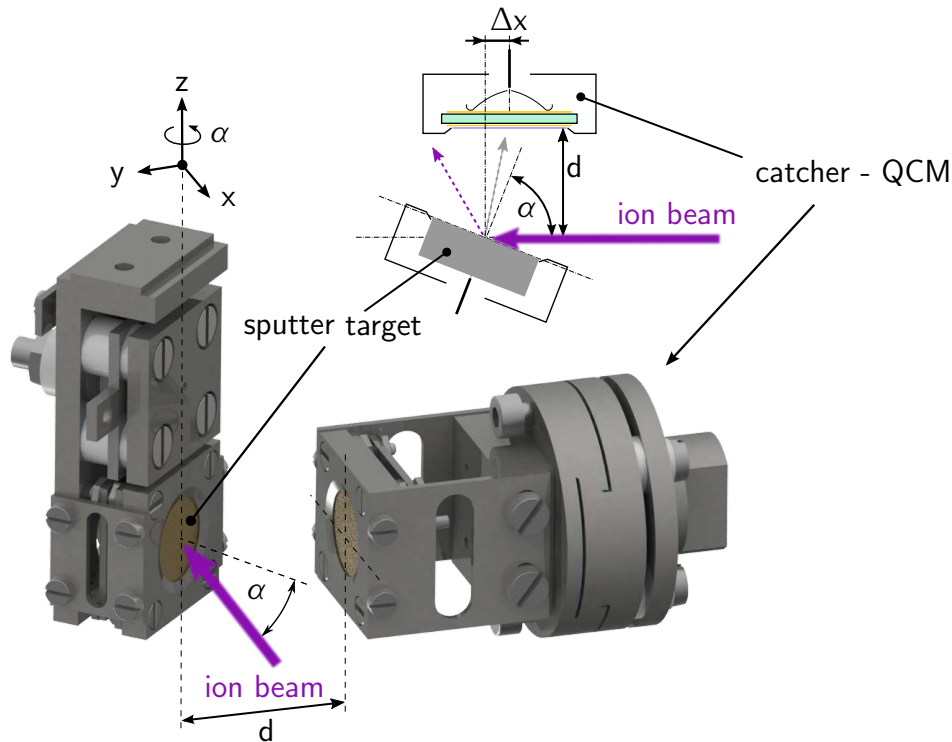
Figure 4.9 – QCM setup in catcher configuration, as schematics and 3D-CAD drawing. A sputter target of any kind is placed in the sample holder of the classic configuration. The ion beam hits the target under an angle of incidence α. The catcher QCM is positioned at a distance d from the sputter target. By varying the relative position Δx a sputtered particles distribution can be evaluated. The surface of the catcher - QCM is always aligned parallel to the ion beam axis (x-axis).

An ion beam hitting the sample under a certain angel of incidence α causes sputtering of the sample material as well as scattering of the projectiles. Sputtered particles stick on the catcher-QCM and cause a decrease of the resonance frequency, but on the other hand scattered projectiles might cause sputtering of the catcher-QCM, reducing the QCM signal. this needs to be included in data evalaution [90].

The so called catcher yield Y_c is equivalent defined as equation 4.1.3, with the difference, that the ion beam scanning area is included here, as can be seen in equation 4.1.13.

$$Y_c\,[\text{amu/projectile}] = \frac{1}{\Phi A_s}\frac{m_0}{f_0}\frac{\Delta f}{\Delta t} \tag{4.1.13}$$

Considering the solid angle Ω this value can also be regarded as differential sputtering yield, where Ω can be defined by the relative position Δx and d, as well as the distorted catcher surface area A_c (equation 4.1.14).

$$Y_{\Omega c}\,[\text{amu/projectile/sr}] = \frac{Y_c}{\Omega(\Delta x, d, A_c)} \tag{4.1.14}$$

Figure 4.10 shows an ideal catcher yield distribution, where a uniform sputtered particles distribution is assumed. The distribution shows a maximum at $\Delta x = 0\,\text{mm}$ and a decreasing signal in both Δx directions, due to the increasing distance and the decreasing or distorted relative catcher surface (compare with figure 4.9). The decreasing signal strength in both Δx directions can be compensated by taking into account the active solid angle Ω, at which sputtered particles can be captured with the catcher QCM. However, the decrease in sensitivity with higher delta x values must be remembered.
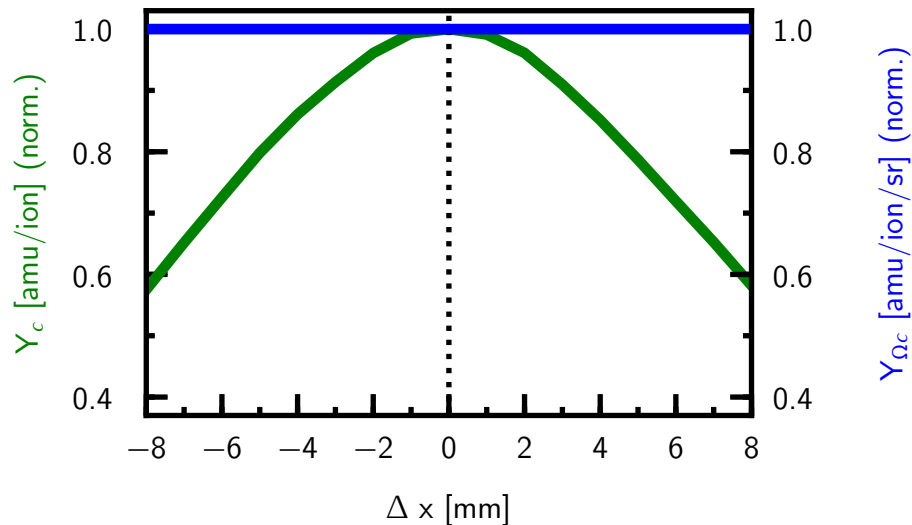
Figure 4.10 – Δx dependence of an ideal modelled and normalized catcher yield, assuming a perfect uniform sputtered particles distribution. The maximum at $\Delta x = 0\,\text{mm}$ and the decreasing of the signal in both directions is related to the increasing distance and distortion of the catcher QCM surface. At $\pm 8\,\text{mm}$ the signal drops below 60%. By taking into account the solid angle Ω at which the sputtered particles can be captured, the drop in both Δx directions can be compensated.

To evaluate an absolute sputtering yield one needs to integrate the catcher yield over the hemisphere, according to equation 4.1.15.

$$Y\,[\text{amu/projectile}] = \int_{2\pi} Y_{\Omega c}\, d\Omega \qquad (4.1.15)$$

Unfortunately experimental setup limitations do not allow evaluating catcher yields Y_c at every position over the entire hemisphere above the sample. Additionally it must be remembered that the QCM technique measures total net mass changes, which includes also sputtering due to scattered projectiles, hitting the catcher surface.

Two different approaches were used to evaluate absolute sputtering yields via the catcher QCM method. It has proved practical to carry out comparative measurements, by using two QCMs simultaneously, where one is used in classic configuration and irradiated directly. This allows to extract absolute sputtering yields and compare them to the catcher yields. This reveals an ratio g for every Δx position, as indicated in equation 4.1.16 [90].

$$g(\Delta x) = \frac{Y}{Y_c(\Delta x)} \qquad (4.1.16)$$

By switching to a sample with unknown roughness but the same material, one can now measure again the catcher yield Y_c in dependence of Δx and estimate the original sputter yield Y by using the parameter g.

Another approach is to perform a signal reconstruction procedure, by using MC-BCA sputter modelling codes, like SDTrimSP or TRI3DYN. Here a modelled sputtered and scattered particles distribution is used and the attempt made to reconstruct the catcher yield signal Y_c. This procedure is explained in more detail in section 4.1.4.2.

4.1.4.1 Measurement Procedure

The measurement procedure is very similar to the classic configuration (chapter 4.1.3.1. At first the ion beam is adjusted and characterized by using the Faraday cup, included in the sample holder (compare with figure 4.6). After adjusting the ion beam scanning area A_s and the ion flux Φ the sample holder is moved to the measuring position, where the ion beam can hit the sample under a certain angle of incidence α. The catcher-QCM is placed at a constant distance d, where the catcher yield Y_c is measured. By varying the relative position Δx

the catcher yield distribution can be evaluated. To avoid additional dynamic effects due to different material sticking the coating of the catcher quartz crystal is chosen equal to the sputter target.

4.1.4.2 Reconstruction of the QCM catcher measurements

Through the use of a correct sputtered and scattered particles spacial-distribution f_{sp} the QCM catcher signal can be reconstructed. These distributions can come for example from a mathematical description, by, for example Sigmund et al. [61] or alternatively from MC-BCA sputter modelling codes, like TRIDYN, TRI3DYN or SDTrimSP as presented in chapter 3 (for more details see also reference [45, 90]). The precise setup configuration need to be taken into account, which can be seen in figure 4.9. This includes the angle of incidence of the ion beam α, the catcher distance d, ion beam scanning along the x and y coordinates and also the sensitivity s of the quartz crystal. The QCM-catcher signal Y_c can then be calculated for every Δx position according to formula 4.1.17:

$$Y_c(\Delta x, \alpha, d) = Y_{c,catched}(\Delta x, \alpha, d) - Y_{c,sputtered}(\Delta x, \alpha, d) \qquad (4.1.17)$$

$Y_{c,catched}$ is the yield of catched sputtered particles and $Y_{c,sputtered}$ the sputter yield at the catcher, caused by scattered projectiles from the ion beam.

$$Y_{c,catched}(\Delta x, \alpha, d) = \int_{x,y} \int_{\Omega} f_{sp,sputtered}(\Omega, \Delta x, x, y) s(\Omega, \alpha, d) dx\, dy\, d\Omega$$

$$(4.1.18)$$

$$Y_{c,sputtered}(\Delta x, \alpha, d) = \int_{x,y} \int_{\Omega} F_{sp,scattered}(\Omega, \Delta x, x, y) s(\Omega, \alpha, d) dx\, dy\, d\Omega$$

$$(4.1.19)$$

$$F_{sp,sccattered}(\Omega, \Delta x, x, y) = \int_E f_{sp,scattered}(\Omega, \Delta x, x, y, E) \cdot Y_{sp}(E) dE \quad (4.1.20)$$

$Y_{c,catched}$ and $Y_{c,sputtered}$ are calculated according to formula 4.1.18 and 4.1.19. The quartz sensitivity s corresponds to a Gaussian function, decreasing radially outwards from its center [89, 91].

At a given QCM catcher position, the spacial distribution f_{sp} is weighted with the radial sensitivity of the quartz s and numerically integrated over solid angle Ω, as well as the ion beam scan area along x and y. For $Y_{c,sputtered}$, the energy and therefore the sputtering of the catcher surface by the scattered particles is included in the spacial distribution $F_{sp,scattered}$, as can be seen in equation 4.1.20. The energy dependence of the sputtering yield $Y_{sp}(E)$ can be evaluated via a separate modelling, assuming a pure and flat sample surface.

As can be seen in equation 4.1.18 the assumption was made, that every sputtered particle hitting the catcher QCM is catched, which is equivalent to a so called sticking coefficient equal to 1. This assumption is reasonable if on top of the catcher QCM a layer of the same material is deposited as of the sputter target [45, 90].

4.2 Sample Analysis Methods

Pre and post sample analysis methods, used in this thesis will be presented here. Precise surface morphology information as well as elemental depth information are essential in order to perform precise sputter modelling and to compare the outcome of experiments to the sputter modelling.

4.2.1 Surface Morphology Evaluation Techniques

Commonly available methods were used to evaluate surface morphologies. Optical instruments like confocal microscope (CM) give a quantitatively overview over a certain surface, but lack in resolution due to the use of light. The used apparatus (μsurf explorer, Nanofocus Labs) allows the measurement of structure sizes down to $0.7\,\mu$m.

For nm-size resolution atomic force microscope (AFM) measurements are well suited and allow extraction of precise height $h(x, y)$ information at every point x, y along a certain range of the surface. This information can then be used to evaluate precise roughness informations (see section 4.2.1.1. During this thesis a Cypher AFM (Oxford Instruments) was used.

AFM measurements are suitable to roughness values up to $R_q \approx 150\,$nm (definition according to equation 4.2.1). Higher roughnesses or nanostructures with overhanging surface structures cannot be measured with this technique.

In this case, scanning electron microscopy (SEM) measurements are more suitable and allow imaging conductive surfaces independent of roughness [92]. This method allows to create a very high contrast image of the surface, but it is not possible to extract precise roughness values from it, as with the AFM method.

42

In combination with a focused ion beam (FIB) this technique allows also to cut through the surface, by using a Ga ion beam with $\approx 30\,\text{keV}$, revealing possible underlying structures. By using a powerful image analysis programs such as 'ImageJ', surface structure sizes as well as underlying structure sizes (revealed via FIB-cut SEM) can be assessed [93].

Different SEM instruments were used during this thesis and were thankfully performed at the HZDR and the FZJ.

4.2.1.1 Surface Roughness

During this thesis the root mean square roughness (RMSR) R_q is mainly used, where its definition can be found in equation 4.2.1.

$$R_q = \sqrt{\frac{1}{n \cdot m} \sum_{i,j}^{n,m} \left(h(x_i, y_j) - \overline{h} \right)^2} \tag{4.2.1}$$

$h(x, y)$ corresponds to the height information at every point x, y and n, m correspond to the number of data points along the lateral x and y directions. $\overline{h}$ is the arithmetic mean value of the height. The size of the measured surface must be chosen big enough to get a usable R_q value.

4.2.1.2 Inclination Distribution

In addition to the roughness, the so-called inclination distribution can be determined. By calculating the two-dimensional slope at every point x, y, the local impact angle Θ can be evaluated (see equation 4.2.2).

$$\vec{v} = \left(\frac{dh}{dx}, \frac{dh}{dy} \right) \quad v = |\vec{v}| \quad \Theta = tan^{-1}(v) \tag{4.2.2}$$

A one-dimensional distribution in the form of a histogram can be evaluated by a statistical analysis of each local impact angle Θ. The maximum and the full width half maximum (FWHM) can then be extracted.

These parameters in combination with the roughness value R_q can describe a surface already quite well, but it must be noted, that any kind of preferred orientation of surface pattern is not included here. However, these parameters were sufficient for the measurements carried out during this thesis.

4.2.2 Elemental Depth Evaluation Techniques

4.2.2.1 Sputter-XPS

To evaluate depth dependent elemental composition of the samples, different techniques were used. X-ray photoelectron spectroscopy (XPS) is a highly surface sensitive technique and allows next to the elemental composition measurements also determination of molecular binding informations of a surface. For gaining depth dependent information, sputtering is used (mainly by using Ar ions at keV energy), to 'dig' into the sample (sputter-XPS). Unfortunately this process can already influence the sample-composition and falsifies the outcome of this measurement technique. Evaluating the actual depth under the surface is done by assuming a constant sputtering yield, which is imprecisely for a mixed elemental sample. The sputter-XPS measurements presented in this thesis were performed at the Analytical Instrumentation Center (AIC) at TU Wien. A custom SPECS XPS system with a monochromatized Al K-alpha source (μFocus 350) and a wide-angle lens hemispherical analyser (WAL 150) was used here. For depth profiling a SPECS sputter ion source was used with $3\,keV$ Ar^{1+} ions.

4.2.2.2 RBS

Rutherford backscattering spectroscopy (RBS) is a powerful ion beam analysis (IBA) tool for investigating film thicknesses and determining elemental compositions. It is a non-destructive measurement technique due to the use of low mass MeV ions and low flux. The energy of the backscattered ions are measured and due to their energy loss, caused by electronic stopping and the reasonable assumption that each ion scatters elastically and only once with a target atom, very accurate elemental depth informations can be obtained [94, 95]. RBS uses mainly ^{4}He ions to ensure backscattering, which means that the momentum transfer to elements with higher masses, or Z number is worse, causing a higher reflection yield and therefore a better signal. This means in turn that RBS has a low sensitivity to low Z materials. Especially the determination of oxide-layers at the surface is difficult or the evaluation of the amount of hydrogen and its isotopes in a sample cannot be measured at all [42, 94, 96]. RBS measurements presented in this thesis were performed at the IPP in Garching, Germany, where a tandem-accelerator with a $3\,MeV$ ^{4}He^{1+} beam was used.

44

4.2.2.3 TOF-ERDA

Another used IBA technique is elastic recoil detection analysis (ERDA). It is based on the RBS technique but here heavy ions are used and the recoiled atoms analysed [94, 97]. This analysis can be done by using a time of flight (TOF) detector in combination with an energy detector as reported in [98]. Advantageous of this technique is the capability to determine the amount of low Z materials in thin films with high precision [97]. The TOF-ERDA measurements shown in this theses were performed at the Ångströmlaboratoriet at the University of Uppsala, Sweden. There a $36\,\mathrm{MeV}$ $^{127}\mathrm{I}^{8+}$ beam was used, impinging the sample surface under an angle of incidence of $67.5°$ (with respect to the surface normal), where the recoiled atoms were measured in forward direction under the same angle of incidence. A detailed description of the setup can be found in references [98, 99].

<div style="text-align: right">*5*</div>

Results on the Erosion of W and Fe Films

*The contents of the following chapter have been partially
published in reference [44].*

In this chapter the results of the erosion of W and Fe films under Ar and D bombardment are presented (section 5.2). The influence of a surface roughness in the nm range and an native oxide layer on the sputtering of Fe under Ar bombardment is investigated in more detail and compared to SDTrimSP (1D and 2D) (section 5.3).

5.1 Preface

In a future fusion power plant, tungsten is foreseen as a PFM and tungsten-containing steels, such as EUROFER, are considered as possible alternatives for recessed areas PFCs in the reactor vessel [100]. Experimental investigations of Fe-W films (with $1.5\,at.\%W$), which are used as model system for EUROFER (nominally $0.33\,at.\%W$), showed a significant reduction of the erosion yield during low energy ion bombardment [101]. The decreased erosion rate was explained by surface enrichment of W, provoked by preferential sputtering of Fe (see also chapter 6 for more details). Additionally, changes in the surface structure due to erosion were measured [42], which also influence the sputtering behaviour. To separate the effect of surface enrichment of high Z materials from the effect of surface structure modifications, sputtering experiments with pure Fe- and W-films were performed and the influence of changes in surface morphology on the sputter yield due to prolonged ion erosion was investigated.

Simulations (e.g. [60]) and theoretical descriptions (e.g. [61]) of sputtering often

only take perfectly flat surfaces into account. This is however an idealization, and although it is possible to produce reasonably flat films for some materials, this assumption will often lead to discrepancies with realistic experimental conditions. A more detailed modelling of this situation with improved codes is necessary to take into account effects like shadowing (especially with grazing ion incidence, some parts of the surface are not directly accessible to the ions) and also redeposition of sputtered particles (compare with figure 2.3 in chapter 2). For this reason, the SDTrimSP-2D code was tested to make an attempt to include the actual surface structure in the sputtering simulations and to test its performance by comparing the results of the simulations to the experimental data [44, 72, 102].

5.2 Literature Data of Sputtering of Fe and W surfaces and Comparison to SDTrimSP-1D

Figure 5.1 summarizes literature data of sputtering yields of W and Fe under normal incidence Ar and D irradiation as well as sputtering data evaluated during this thesis and obtained by using the classic QCM technique (red circles inf figure 5.1). Apart from this a comparison with modelling with the 1D version of SDTrimSP is shown, where pure elemental samples and a flat surface were assumed. One can see that absolute values of sputtering yields differ between the experiments by more than a factor of 2 and also the agreement to modelling with SDTrimSP-1D is moderate, which once again points out the necessity to improve the modelling.

5.3 Ar Irradiation of Fe and Comparison to SDTrimSP-2D

In this section a detailed comparison of experimental sputtering of Fe films with the code SDTrimSP-2D was performed. In section 5.3.1 the experimental approach will be presented in detail, including a precise analysis of the sputtering sample. Section 5.3.2 presents the modelling method using the 2D version of the code SDTrimSP, where also the novel approach is shown to include a real 2D surface morphology into a 1D line-surface as input for the code. Finally section 5.3.3 compares the results and presents the performance of the code SDTrimSP-2D. The main parts of chapters 5.3 and 5.4 have been published in reference [44].
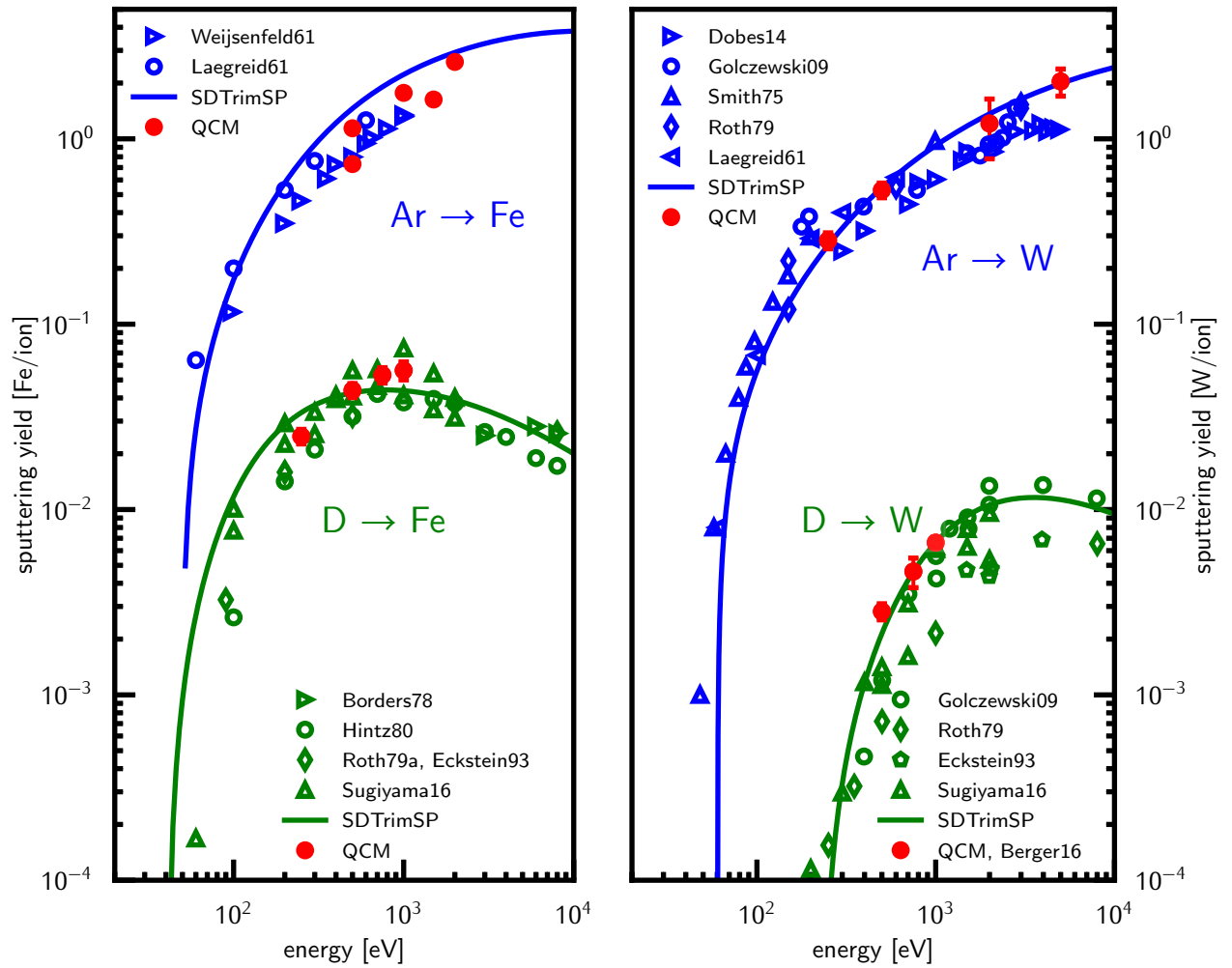
Figure 5.1 – Energy dependence of the sputtering yield for Fe (left image) and W (right image) for D (green) and Ar (blue) irradiation under normal incidence and comparison to literature data as well as to static simulations with SDTrimSP-1D (solid lines). The red circles highlight the experimental results obtained with the classic QCM technique during this thesis [83, 103–114].

5.3.1 Experimental Approach

The measurements have been performed using the classic QCM setup (chapter 4.1). The investigations here concentrated on mono-energetic Ar ions of 500 eV hitting on an Fe-coated QCM sample. Ar will be used as, so-called, seeding gas in fusion reactors like ITER, to avoid local overheating of the PFCs by radiative cooling [30]. Additionally Ar $\rightarrow$ Fe sputtering yields are significantly higher than D $\rightarrow$ Fe sputtering yields, making Ar^{1+} projectiles ideally suited for the experiments. This can also be seen in figure 5.1.

Typically 400 nm thick Fe films were deposited onto polished quartz crystals, by using a magnetron sputter deposition device at IPP Garching, Germany. As the samples were exposed to atmosphere, the presence of an oxide layer on the Fe film was assumed. Therefore one of the Fe samples was analysed by sputter-XPS. Sputter depth profiling via Ar-ion sputtering in combination with XPS was used to obtain the quantitative elementary analysis as a function of depth (see chapter 4, section 4.2.2.1 for setup details).
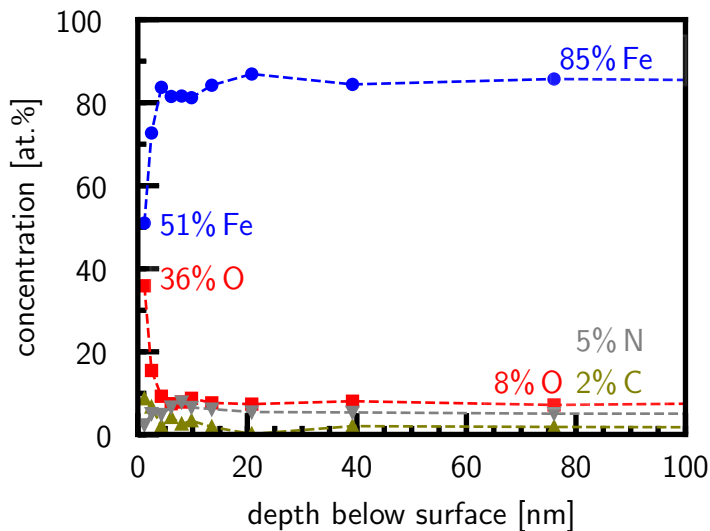
Figure 5.2 – Elemental depth profiles of a virgin Fe sample as determined by Sputter-XPS. The estimated error of the data points is 10%. The XPS analysis of the Fe-film as function of depth shows a significant oxide layer on top of the sample [44].

XPS results are shown in figure 5.2 and reveal a high concentration of O at the surface indicating a native oxide layer as expected. Long term depth profiling shows that the Fe concentration finally reaches 85% in the bulk of the film but significant concentrations of O, N and C are still detected in the XPS spectra. In section 5.3.2 it will be shown, that for the simulations it is essential to take

the actual elemental composition into account. The evolution of the sputtering behaviour of the Fe model films under Ar ion bombardment was then investigated at the specific angle of incidence of $\alpha = 60°$ and in dependence of the bombarding ion fluence (results are shown in section 5.3.3). Measurements were performed at an Ar base pressure of 1×10^{-7} mbar, reaching an Ar ion flux of $\Phi \approx 5 \times 10^{16} \text{m}^{-2}\text{s}^{-1}$. AFM images of the Fe-coated quartz crystal samples were taken before and after prolonged irradiation (see figure 5.3). On the initial surface, nano-scale structures are visible (figure 5.3a) that significantly change during the ion bombardment. After applying a total Ar fluence of $8 \times 10^{21} \text{ m}^{-2}$ under an angle of incidence of 60° a structure aligned int the direction of the incoming projectiles is observable (figure 5.3b).
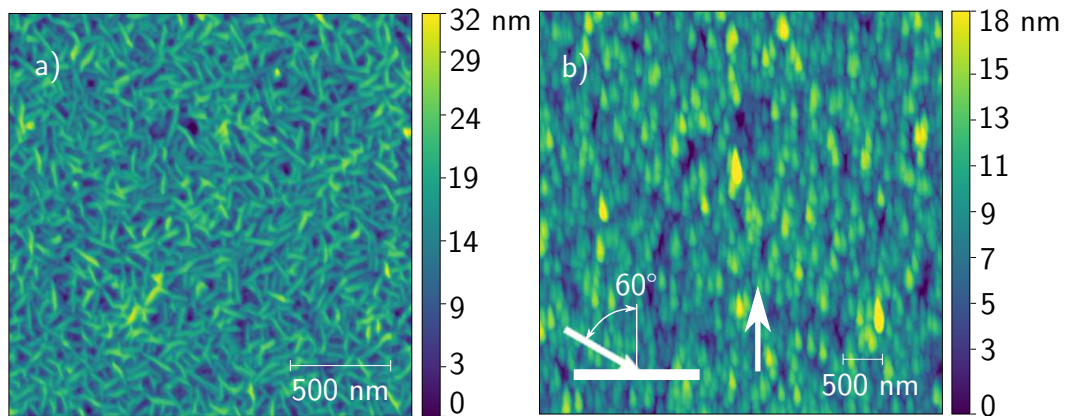
Figure 5.3 – AFM images of the target before (a) and after (b) prolonged Ar ion irradiation with a total fluence of $8 \times 10^{21} \text{ m}^{-2}$ reveal a change of the surface morphology. An initial nano-scale structure, with no preferred orientation on an unirradiated sample transforms into a structure clearly aligned in the direction of irradiation (indicated by a white arrow) [44, 115].

5.3.2 Modelling with SDTrimSP-2D

The two-dimensional MC-BCA code SDTrimSP-2D, developed at the IPP, was used here and allows to make an attempt of including a line surface structure into an SDTrimSP erosion simulation [72].

This is realized by expanding the geometrical description from layers to a grid, where the cells of this grid can either be vacuum or solid. Modification of these cells are calculated from the material transport following the collision cascades. Surface cells can grow and shrink based on the transport of target atoms and thus a change in the surface morphology can be simulated (for more details of the codes underlying principle see chapter 3).

The surface topography of the Fe films, measured via AFM (figure 5.3), was used

as an input for SDTrimSP-2D. But the AFM images in figure 5.3 clearly show a structure that cannot simply be reduced to two dimensions without loosing information about the surface. If only one line of (x, z)-coordinates of the AFM image were taken, for example, the surface would appear much flatter because any additional tilt in the y-direction would be ignored. Therefore an initial two dimensional target was defined which has the same R_q roughness value as the real sample and the same distribution of the "local impact angles Θ", or inclination distribution (compare with section 5.3.3). This distribution shows the frequency of impact angles between the local surface normal and projectile incidence direction (compare with figure 2.3 in chapter 2). A model target consisting of 10 initial layers with different concentrations of Fe and O according to the elemental composition obtained from the XPS measurements (figure 5.2) was created. Additionally the compound option in SDTrimSP-2D was used to account for the density and surface binding energy for iron(III)-oxide (data taken from [66]). The final target surface used as the starting point for the SDTrimSP-2D simulations is shown in figure 5.4a, where the color scale indicates the O concentration.

Using this model target, SDTrimSP-2D simulations with 500 eV Ar under 60° were performed. The fluence dependence of the sputtering yield as well as the change of the surface morphology during prolonged ion irradiation was simulated. Also the angular dependence of the sputtering yield before and after these irradiations was investigated. The results of these simulations are presented hereinafter and compared to the experimental data.

5.3.3 Comparison of Experimental Results to SDTrimSP-1D and SDTrimSP-2D

Figure 5.5 presents the measured fluence dependent sputtering yield of the Fe coated QCM sample at 500 eV Ar ion irradiation under an angle of incidence of 60°. The sputtering yield increases from 0.7 Fe/Ar to 1.5 Fe/Ar and reaches steady state after an Ar fluence of about $2 - 3 \times 10^{21}$ m^{-2}. It needs to be noted, that the QCM technique allows measuring the total mass change rate only. The resulting mass change rate is then divided by the molar mass of Fe to scale it to the sputtering yield of Fe [113].
The observed initial strong change of the sputtering yield is due to the removal of an oxide layer on top of the sample, while changes at higher fluences can be attributed to the change in surface morphology/roughness. The SDTrimSP-1D simulation assuming a target with pure Fe shows no fluence dependence and a constant sputtering yield of 2.2 Fe/Ar, which is higher than the actual measurements. A detailed analysis of our simulation results show that the main reason for this discrepancy can be found in the C, N and O concentrations of the sample
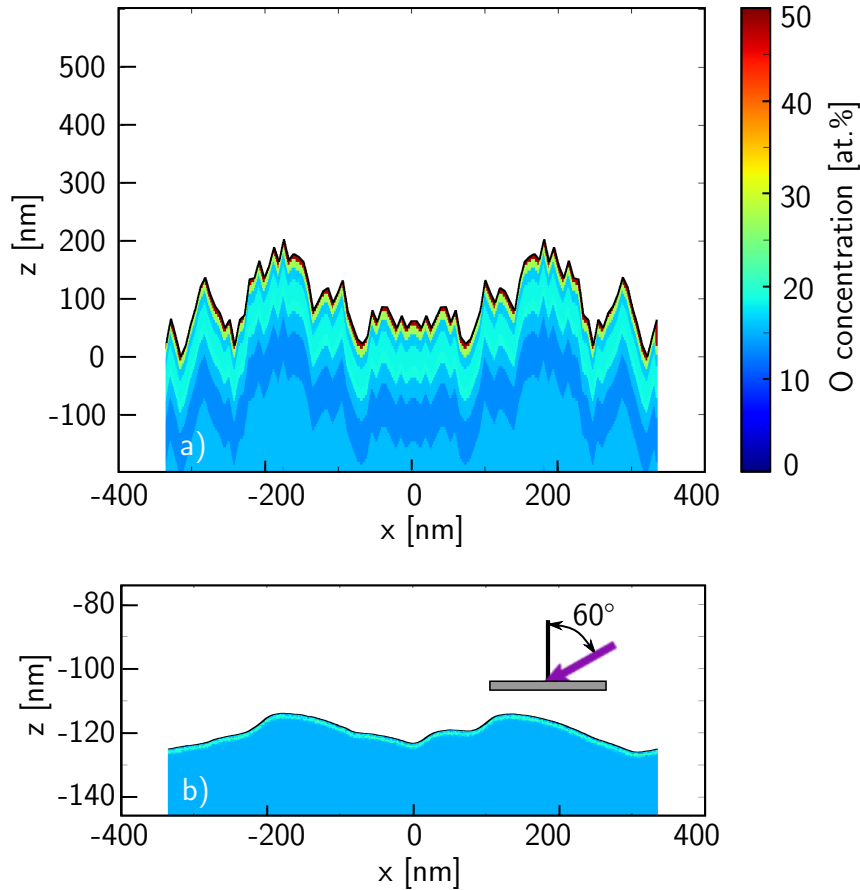
Figure 5.4 – (a): The line-surface model used as input for the SDTrimSP-2D simulations. The color code represents the O concentration. The x-axis represent the lateral position along the surface and the z-axis the depth, relative to the unirradiated surface. The surface was defined to have the same inclination distribution and R_q roughness as measured via the AFM image in figure 5.3.
(b): After irradiation with $500\,\text{eV}$ Ar ions up to a fluence of $8 \times 10^{21}\,\text{m}^{-2}$ impinging under an angle of incidence of $60°$ from the right (in -x direction), the simulations show a smoothening of the surface consistent with the experimental data presented in figure 5.3. Additionally oxygen depletion at the surface occurs [44].

neglected in this 1D simulation. If the SDTrimSP-1D simulation includes the elemental depth distribution, as measured with sputter-XPS, the resulting sputtering yield is closer to the experimental data, but still too high and the transient effect at very low fluences is not well reproduced. It should be noted, that the 1D version of SDTrimSP (version number 5.07) is not able to include iron-oxide compounds for a given elemental depth distribution, which could be a reason for the overestimation of the sputtering yields even in steady state. The SDTrimSP-2D simulation in addition also includes the initial surface morphology and all dynamically changes during simulated ion irradiation, which leads to very good agreement with the experimental data. Both the steady state sputtering yield of $1.5\,\mathrm{Fe/Ar}$ as well as the transient effects at very low fluences are very well reproduced [44].
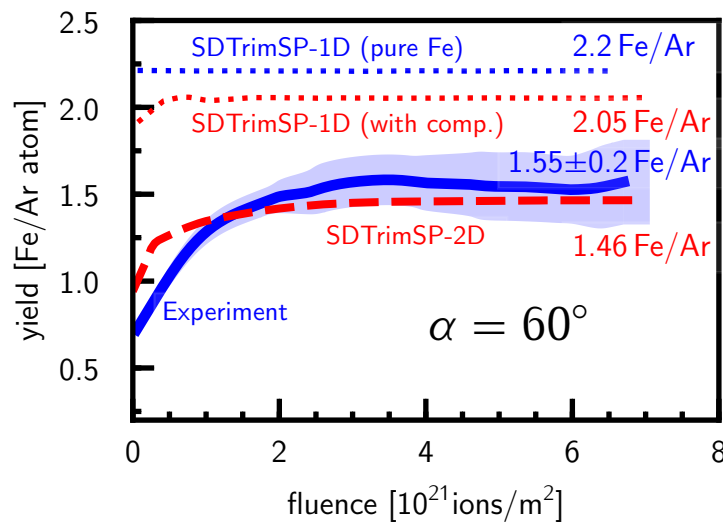
Figure 5.5 – Measured fluence dependence of the sputtering yield for $500\,\mathrm{eV}$ Ar ions bombarding an iron film under an angle of incidence of $60°$ (thick blue line). The increase of the sputtering yield at low fluences corresponds to the sputtering of the oxide layer. The dotted and dashed lines represent numerical simulations with SDTrimSP-1D and 2D. Taking into account the actual elemental composition of the target improves the 1D simulation (red dotted line) somewhat. By including the surface morphology in a SDTrimSP-2D simulation (thick red dashed line) the agreement with experimental results is substantially improved [44].

In figure 5.6 experimental data for the measured and simulated Fe sputtering yields as a function of the ion impact angle α are compared for two cases: The green triangles show the situation of the initial target. In addition to the full dynamic SDTrimSP-2D results (solid lines) also data obtained with the 1D version of SDTrimSP are compared, assuming a pure and perfectly flat Fe target (blue dotted line), as well as including the elemental depth concentration of the sample (red dotted line). Neither the absolute value nor the qualitative characteristic of the angular dependence can be reproduced correctly with the 1D simulation,

while agreement with the 2D version is excellent. It is interesting to see that SDTrimSP-2D predicts even at gracing incidence angles high sputtering yields, but this could not be confirmed due to limitations in the experimental setup. After a total Ar fluence of $8 \times 10^{21} \, \mathrm{m}^{-2}$, applied under an angle of incidence of $60°$, the agreement with SDTrimSP-2D remains excellent. Here the SDTrimSP-1D simulation, which includes also the elemental depth composition but assumes a flat surface, gives a good qualitative agreement with the measurement, but the absolute values of the sputtering yield are too high. The more pronounced angular dependence of the sputtering yield after applying the fluence of $8 \times 10^{21} \, \mathrm{m}^{-2}$ indicate an ion induced smoothening of the surface, which is confirmed by the AFM measurements (figure 5.3) [44].
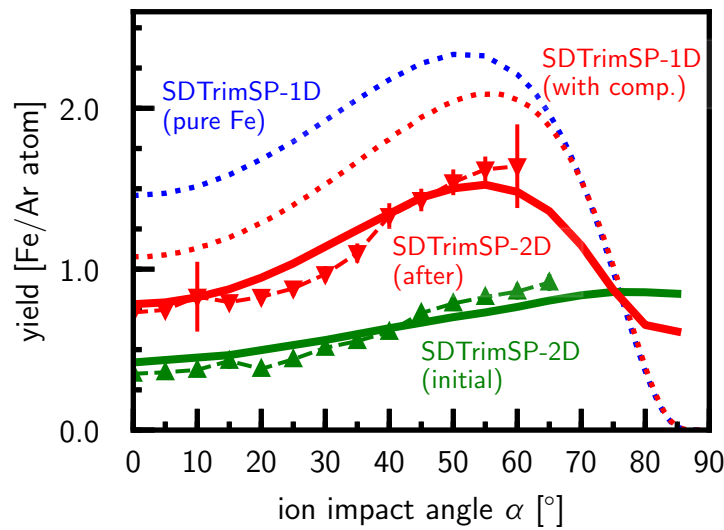
Figure 5.6 – The green triangles give the measured Fe sputtering yield as a function of nominal impact angle for the initial target surface. A simulation with SDTrimSP-2D (green curve) which includes both the measured surface roughness (from AFM) and elemental composition (from XPS) fits the experimental data better than a static 1D simulation with SDTrimSP assuming a flat surface and a pure Fe target (blue dotted curve). The agreement remains excellent when comparing the experimental data for the Fe film (red inverted triangles) irradiated with a total Ar fluence of $8 \times 10^{21} \mathrm{m}^{-2}$ with a fully dynamic SDTrimSP-2D simulation starting from the initial situation given in figure 5.4a. The SDTrimSP-1D simulation, which includes also the elemental depth composition with a flat surface (red dotted line) show a good qualitative agreement, but the absolute values are too high [44].

The root mean square (RMS) roughness R_q, evaluated from the AFM measurements, shows a decrease from $5.2 \, \mathrm{nm}$ (figure 5.3a) to $3.5 \, \mathrm{nm}$ (figure 5.3b). The RMS roughness value R_q from SDTrimSP-2D gives $3.6 \, \mathrm{nm}$ (figure 5.4b) and confirms the AFM measurements also very well. This smoothing can better be

quantified by the inclination distribution Θ. This distribution can be evaluated also from the AFM data and a comparison between this distribution of angles before and after irradiation is shown in figure 5.7 [44].
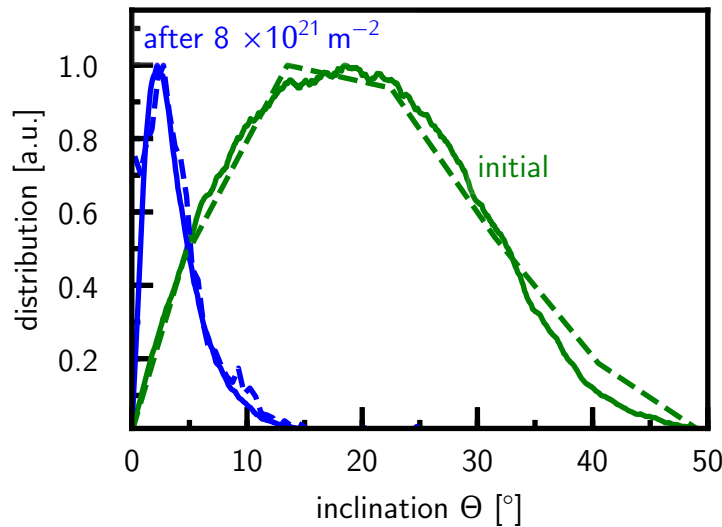
Figure 5.7 – The inclination distribution Θ (i.e. the angles between the direction of the incident projectile and the local surface normal) as derived from the AFM images in figure 5.3, show a shift towards lower angles and a decrease in width after ion irradiation under 60° and up to a fluence of 8×10^{21} m^{-2}. The dashed lines show the results of numerical simulations with SDTrimSP-2D [44].

The inclination distribution of the initial rough surface has a peak at around 20° and is rather broad, with a FWHM of 28°. The distribution after irradiation has a peak at 2° and a FWHM of 4°. As a perfectly flat surface would be represented by a delta distribution at 0°, the surface can be interpreted as much smoother after the ion irradiation. Figure 5.7 also shows the initial local angular distribution of the unirradiated model surface for SDTrimSP-2D (figure 5.4a), which was chosen to match the real surface, evaluated with AFM (figure 5.3a). After a simulated irradiation with Ar by 8×10^{21} m^{-2} under 60°, the calculated angular distribution narrows to a FWHM of 4° and has its maximum also at 2°. The smoothing is thus confirmed by SDTrimSP-2D. The remaining small discrepancies between measurement and simulation are probably due to the two dimensional approach. The missing extra dimension reduces possible local impact angles in this dimension, so the local impact angle statistics show also a peak at 0° [44].

5.4 Summary and Outlook

Sputtering experiments of W and Fe samples under Ar and D ion bombardment have been performed by using the classic QCM technique and compared to BCA simulations with the code SDTrimSP-1D. The moderate agreement between experiments and modelling shows that simulations need to be improved by taking into account surface morphologies and accurate elemental depth informations.

Therefore, the erosion of Fe films under 60° ion bombardment was investigated in very detail and compared with the new code SDTrimSP-2D, which allows to include a line surface.

Monoenergetic Ar ions at $500\,\mathrm{eV/Ar}$ were used for prolonged irradiation of the samples under an angle of incidence of 60°. Sputter XPS measurements of the unirradiated samples revealed a clear oxide layer on top and an Fe concentration of only 85% with substantial impurities of O, N and C in the bulk. AFM measurements before and after irradiation with a total Ar fluence of $8 \times 10^{21}\,\mathrm{m^{-2}}$ reveal information about the change in surface morphology, R_q roughness and the inclination distribution. A clear decrease of R_q, as well as the width of the inclination distribution could be observed. Additionally nano-scale structures, oriented in the direction of the incident ion beam could be seen. SDTrimSP-1D simulations assuming a pure elemental target and a perfectly flat surface were not able to reproduce the sputtering behaviour. Including the elemental depth composition into SDTrimSP-1D improved the qualitative agreement at least for the angular dependent sputtering behaviour of the irradiated sample. Only by considering the actual surface structure and elemental composition, including the correct compound information in an SDTrimSP-2D simulation, a close agreement between simulation and experiment could be achieved. It could be shown, that rather small R_q values in the nm range have already a severe influence on the absolute sputtering yield [44].

While a two dimensional modelling with SDTrimSP-2D is already quite successful, a full 3D code, called SDTrimSP-3D is under development at IPP and promises even better results [75]. With this code it should be possible to simulate effects like formation of ripple-like structures and to investigate their influence on the sputtering behaviour. As an alternative the full 3D code TRI3DYN is already available and its performance will be presented in the following chapter 6.

6

Results on the Erosion of Fe-W Model Films

*The contents of the following chapter have been partially
published in references [43] and [42].*

In this chapter a detailed comparison between the QCM erosion measurements for Fe-W model films under D ion bombardment and simulations using the code TRI3DYN is presented. These Fe-W films serve as a model system for W containing steels, like EUROFER, which could be an attractive and cost efficient alternative to a full W main chamber first wall in a future fusion device [116, 117]. Furthermore, these experimental erosion measurements allow a detailed benchmarking of the full 3D-MC-BCA code TRI3DYN.

6.1 Experimental Data

The experimental results used for benchmarking the code TRI3DYN have been obtained at TU Wien and partially already presented in [42]. In the following the experimental procedure and main results are summarized. Sample preparation and initial analysis was done at IPP Garching within the EUROfusion work package on plasma-facing components [38, 42]. 670 nm thick films of Fe-W, containing nominally $1.5\,\mathrm{at.\%}$W, were deposited onto several quartz crystal discs by using magnetron-sputter deposition with multiple targets.

The samples were then analysed via RBS measurements (see chapter 4, section 4.2.2.2 for details) confirming the thickness and a W concentration of $1.5\,\mathrm{at.\%}$. The RBS data, however, also showed an oxygen amount of $1.5\,\mathrm{at.\%}$ (the results are summarized in table 6.1) [42]. Independently, the elemental composition of the films as a function of depth were determined by sputter-XPS measurements

performed at the AIC of TU Wien (see chapter 4, section 4.2.2.1 for details). Sputter-XPS results are shown in figure 6.1. Beside a clear oxide layer in the topmost few nanometers, oxygen as well as some impurities like C and N are also found in the bulk of the sample. AFM images of the virgin samples can be seen in figure 6.2(a), taken from [42]. The images presented here have a lateral resolution of 200×200 pixels with a scan size of $389\,\text{nm} \times 389\,\text{nm}$. The surface of the freshly deposited film displays a grain like structures with a length of about $200\,\text{nm}$ and a root-mean-square roughness of $3.2\,\text{nm}$ [42]. Sputtering experiments have been performed by using the classic QCM technique (see chapter 4.1 for details). A sputter ion source provided a D ion beam with $250\,\text{eV/D}$, where the main contribution of the ion beam was D_2^+ in molecular form (94.5%).

The ions impact energy is very close to but slightly above the sputtering threshold for W by deuterium projectiles, therefore the sputtering yield of W is about three orders of magnitude smaller than the yield of Fe. With a deuterium flux of $\Phi \approx 4 \times 10^{17}\,\text{m}^{-2}\text{s}^{-1}$ total fluences of up to $4 \times 10^{23}\,\text{m}^{-2}$ could be applied to the samples. In total three samples have been irradiated under an angle of incidence of $0°$, $45°$ and $60°$ with respect to the surface normal and at a temperature of $465\,\text{K}$ [42]. After irradiation the surface morphology changes were evaluated by AFM.

Table 6.1 – Film thickness and elemental composition of the Fe-W films as analysed by RBS and used for TRI3DYN (data taken from [42]).

thickness [nm]	Fe [at.%]	O [at.%]	W [at.%]	Ar [at.%]
670	96.5	1.5	1.5	< 1.0

6.2 Modelling with TRI3DYN

The sputter modelling software TRI3DYN [74] was used here, where its fundamentals are described in chapter 3. The code uses the principle of 'pseudoatoms' as projectiles, each representing a certain number of real projectiles. A higher statistical accuracy can be achieved with a high pseudoatom number, but at the cost of computation time. In these simulations shown here a pseudoatom to real atom factor of 17.1 was used, meaning that one pseudoprojectile is equivalent to 17.1 real projectiles, to ensure high accuracy. This leads to a total computation time of about 1300 cpu hours for each angle of incidence [43].

Figure 6.2(a) shows the experimentally obtained AFM image from [42]. The marked white square in figure 6.2(a) with a lateral expansion of $194 \times 194\,\text{nm}^2$ was used as topography input for TRI3DYN. To fulfill the necessary periodic boundary conditions this image had to be mirrored in both lateral directions. Since the original surface morphology has no particular preferred orientation, no information is
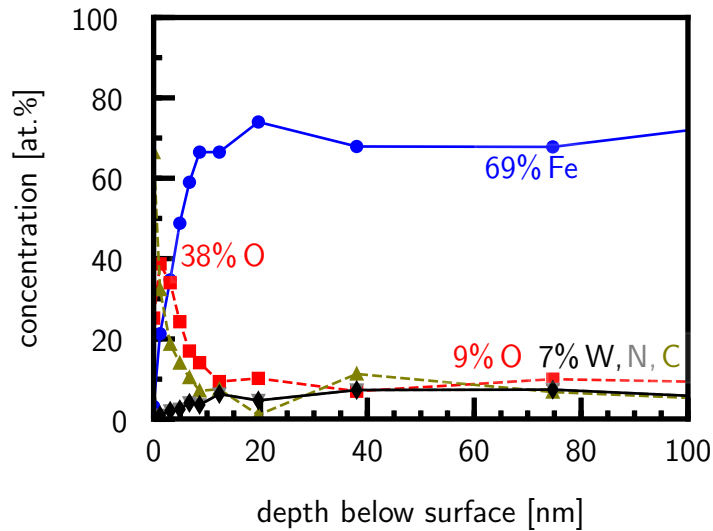
Figure 6.1 – Elemental depth profiles of a virgin Fe-W sample as determined by Sputter-XPS and used as input for TRI3DYN. The estimated error of the data points is 10%. An oxide layer at the surface and some light impurities (C, N, O) in the bulk are clearly visible. The bulk material contains up to 7 at.% W and 9 at.% O [43].

lost. The resulting initial root-mean-square roughness is $R_q = 2.9$ nm and i.e. almost the same as the full sized AFM image ($R_q = 3.2$ nm). The initial elemental depth profile input for TRI3DYN was taken from either sputter-XPS (figure 6.1) or RBS (table 6.1). Due to the significant difference of these measurements, simulations have been performed using input data from both techniques and the results later compared to the experiments. The resulting (initial) voxel pile can be seen in figure 6.2(b), where only the first 40 voxel layers are displayed. As soon as a complete voxel layer is sputtered away in the simulation, a new layer with the elemental distribution of the initial bottom layer is added at the bottom of the voxel pile. This should ensure that no projectile is transmitted through the bottom. Figure 6.2(c) shows a cross section of the voxel pile, displaying the initial surface line structure and elemental W concentration [43].
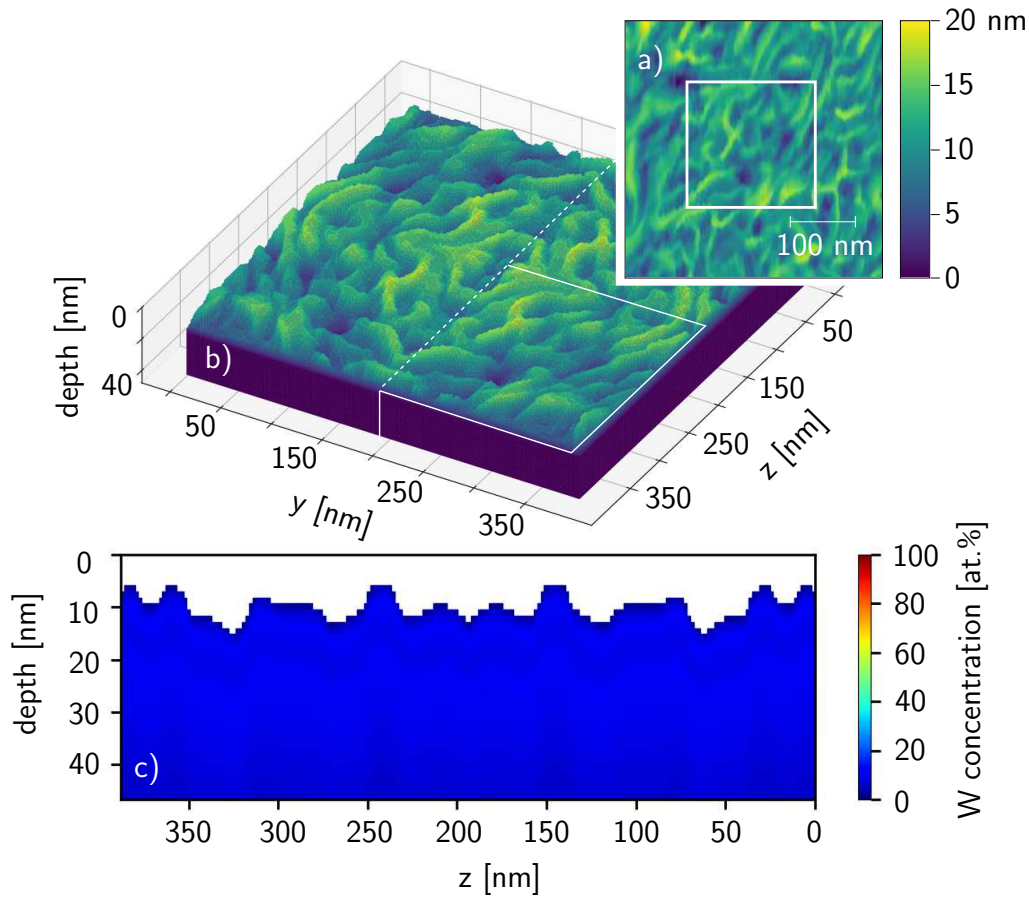
Figure 6.2 – (a) An AFM image [42] measured on the unirradiated Fe-W sample served as surface morphology input for our TRI3DYN simulations, with a R_q of 3.2 nm. For computational reasons the height information from only a part of the image (indicated by the white square) was extracted. To ensure periodic boundary conditions, this image had to be mirrored in both lateral directions, resulting in the voxel layer data shown in (b). There every voxel has a size of $11 \times 19 \times 19$ Å^3 (depth $\times$ y $\times$ z). The color code in (a) and (b) is equivalent. In (c) a cross-section through the middle of the voxel layer data (white dashed line in (b)) can be seen, showing the initial W concentration according to Sputter-XPS measurements [43].

6.3 Comparison of TRI3DYN Simulations to Experimental Data

The comparison was performed with experimental QCM data obtained for D projectiles at $250\,\mathrm{eV}$ impacting under angles of incidence of $0°, 45°$ and $60°$.

6.3.1 Fluence Dependence of the Mass-Removal-Rates

A continuous drop in the mass removal rate with increasing fluence and at constant impinging ion flux has been found, where the slope of this drop is higher at steeper angle of incidence [42]. As shown in figure 6.3 (solid blue line) the mass removal rate starts at $1.2\,\mathrm{amu/D}$ for $0°$, $1.1\,\mathrm{amu/D}$ for $45°$ and $1.7\,\mathrm{amu/D}$ for $60°$ ion beam angle of incidence and continuously drops to around $0.5\,\mathrm{amu/D}$ after a total fluence of $4 \times 10^{23}\,\mathrm{m}^{-2}$ without any sign of yet reaching a steady state value.
The standard interpretation in our [42] and previous work of other groups [101,116, 117] for this behaviour is, that due to preferential sputtering of Fe, the surface is enriched with W, thus reducing the sputtering yield considerably. Our simulations with TRI3DYN confirm this continuous reduction of the mass removal rate [43].

The TRI3DYN calculation for normal incidence ($\alpha = 0°$) using the sputter-XPS elemental depth data as input shows a quick drop from $0.9\,\mathrm{amu/D}$ to $0.5\,\mathrm{amu/D}$ after a fluence of only $7 \times 10^{22}\,\mathrm{m}^{-2}$, followed by a slower decrease of the mass removal rate (green dashed line in figure 6.3). Here the gradient of the mass removal rate shows a slope nearly identical to the QCM experiment. These calculations, however, slightly underestimate the measured mass removal rate.
A very comparable result can also be seen for an angle of incidence of $45°$. A quick drop of the mass removal rate from $1.25\,\mathrm{amu/D}$ to $0.75\,\mathrm{amu/D}$ after a fluence of only $5 \times 10^{22}\,\mathrm{m}^{-2}$ is followed by a slower decrease of the mass removal rate, with a comparable slope to the QCM experiment. Here also the resulting mass removal rate is underestimated.
When looking at the TRI3DYN results of the $60°$ angle of incidence, using the XPS elemental depth data as input, it is noticeable that the initial mass removal rate, of $1.7\,\mathrm{amu/D}$, corresponds exactly to the experiment. The mass removal rate drops quickly to $1\,\mathrm{amu/D}$, after a fluence of only $1 \times 10^{22}\,\mathrm{m}^{-2}$, where then the slope is lower and equal to the experimental one, though the absolute value slightly underestimated. After a fluence of $2.1 \times 10^{23}\,\mathrm{m}^{-2}$ another decrease of the slope is observable. The resulting TRI3DYN mass removal rate after $4 \times 10^{22}\,\mathrm{m}^{-2}$ is as before underestimated.
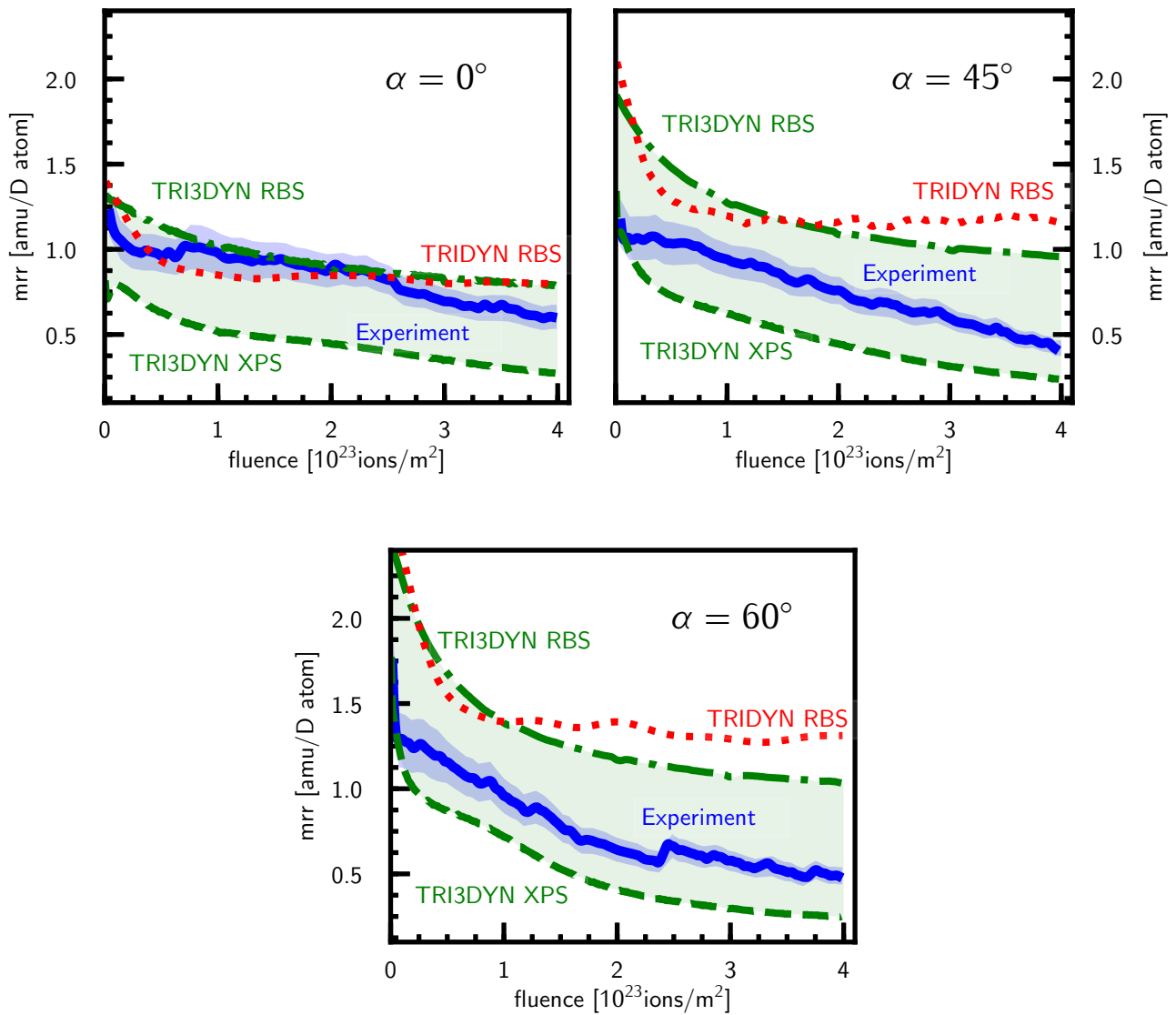
Figure 6.3 – Fluence dependence of the mass removal rate (mrr) under D ion bombardment at $250\,\text{eV/D}$ under different angles of incidence α. The dashed and the dashed-dotted line show TRI3DYN results, using RBS information and sputter-XPS elemental depth information as input. The full line represents experimental results evaluated with the QCM technique and lies between both TRI3DYN calculations. A clear decrease of the mass removal rate is observable, which is confirmed by TRI3DYN. A 1D simulation with TRIDYN shows a strong decrease of the mass removal rate and reaches steady state conditions already after around $1 \times 10^{23}\,\text{m}^{-2}$ [42, 43].

The TRI3DYN calculation using the RBS elemental depth data as input, displays a generally higher mass removal rate, as compared to the QCM experiments (compare with figure 6.3). At normal incidence the agreement with the experimental data is comparable good, although the quick drop at low fluences cannot be reproduced. The mass removal rate starts at $1.3\,\mathrm{amu/D}$ and continually decreases. After a fluence of $4 \times 10^{23}\,\mathrm{m}^{-2}$ the resulting mass removal rate is with $0.7\,\mathrm{amu/D}$ slightly higher than the measured value.

An angle of incidence of $\alpha = 45°$ shows in TRI3DYN with $1.9\,\mathrm{amu/D}$ an almost factor of two higher mass removal rate, compared to the experiment. At low fluences, a higher gradient can be seen, which continuously decreases and still does not reach steady state even after a fluence $4 \times 10^{23}\,\mathrm{m}^{-2}$. The resulting mass removal rate at this fluence is also by a factor of two higher than the experimental value.

A very similar picture can be seen under an angle of incidence $\alpha = 60°$. A pronounced slope in the mass removal rate at low fluences continuously reduces, but after a fluence of $4 \times 10^{23}\,\mathrm{m}^{-2}$ it has still not reached equilibrium.

To test the influence of changes in the surface morphology, a simulation with TRIDYN (1D) (which uses RBS elemental depth information and a perfectly flat surface) is shown in figure 6.3 for comparison. The resulting mass removal rate is overestimated by TRIDYN too (probably because of using the RBS input data). However, while a quick reduction of the mass removal rate is observable, already at about $1 \times 10^{23}\,\mathrm{m}^{-2}$ steady state conditions are reached [43].

6.3.2 Fluence Dependence of the Elemental Surface Concentrations and Roughnesses

The assumed surface enrichment of W due to preferential sputtering of Fe [42, 116, 117] is confirmed by TRI3DYN. Figure 6.4 displays the calculated fluence dependence of the mean elemental surface concentration. Using the RBS data as input (left column of figure 6.4) a continuous Fe reduction and a W surface enrichment up to 33% is calculated for an angle of incidence α of $45°$ and $60°$. For normal incidence the W surface enrichment reaches 28%. In all cases an increase in roughness R_q was found, which is stronger at steeper angles of incidence. At normal incidence ($\alpha = 0°$) the R_q value reaches $4.5\,\mathrm{nm}$ after a fluence of $4 \times 10^{23}\,\mathrm{m}^{-2}$, at $\alpha = 45°$ an R_q of $5.1\,\mathrm{nm}$ was found and under $\alpha = 60°$ an R_q of $5.9\,\mathrm{nm}$ can be observed.

By using the sputter-XPS data (right column of figure 6.4) a quick depletion of the impurity layers containing O and C can be seen, thus exposing the underlying Fe and W layers. With increasing fluence, however, the W enrichment at the surface reaches 67% for normal incidence ($\alpha = 0°$), 76% for $\alpha = 45°$, but only 63% for $\alpha = 60°$. Not surprisingly these changes in elemental concentrations have a
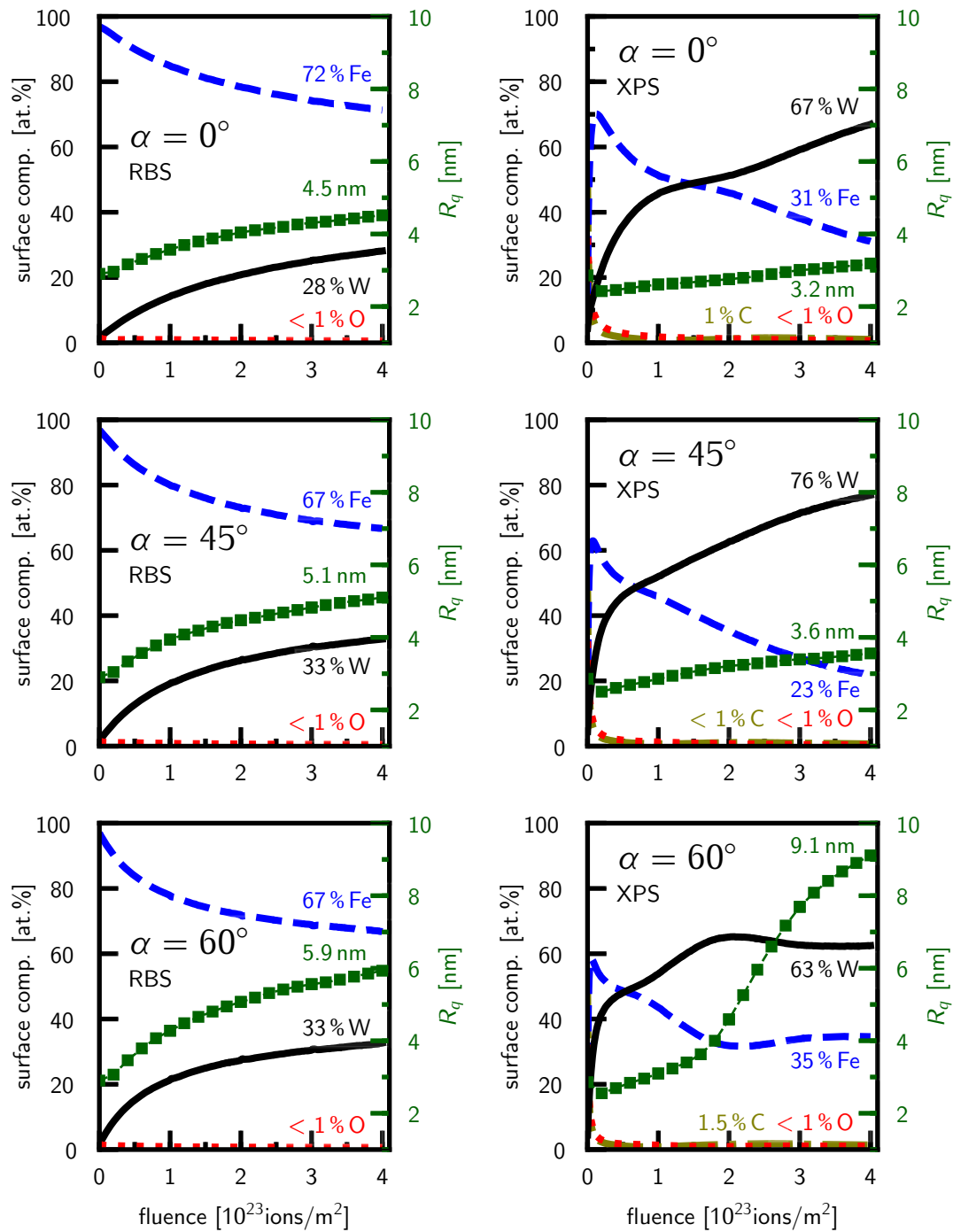
Figure 6.4 – Fluence dependence of the mean elemental surface concentration and root-mean-square roughness R_q under different angle of incidence α, evaluated with TRI3DYN. The left column of figures show the results using RBS data as input. A continuous surface enrichment of W is observed (black line), which is faster at steeper angle of incidences and causes also higher R_q values (green squares). In the right column of figures the results using XPS data as input can be seen. A quick depletion of O and C is followed by an increase of W surface concentration, as well as an increase in R_q.

direct effect on the sputtering yield, as can be seen by comparing figure 6.4 with figure 6.3. The increased mass removal rate at low fluences correlate with the low surface enrichment of W.

It is interesting to see that the roughness R_q drops at low fluences, during the depletion of the surface oxygen, but then continuously rises again, although the resulting R_q values after a fluence of $4 \times 10^{23}\,\mathrm{m^{-2}}$ are lower compared to the modelling results using RBS data. A special case represents the result under the angle of incidence of $\alpha = 60°$: Here the surface enrichment of W increases up to a fluence of about $2 \times 10^{23}\,\mathrm{m^{-2}}$, but then remains nearly constant around 63%. From this fluence value onwards one can also see a very strong increase in the roughness which reaches an R_q of 9.1 nm after a fluence of $4 \times 10^{23}\,\mathrm{m^{-2}}$.

It must be noted that the displayed elemental surface concentration values represent mean values averaged over the whole surface, meaning that local variations or material accumulations cannot be seen here.

Nevertheless TRI3DYN allows also to visualize resulting variations in surface concentrations, which will be shown hereinafter for the modelling using sputter-XPS elemental data as input (figure 6.5c, figure 6.6c and figure 6.7c). A clear surface enrichment of W can be seen up to a depth of 10nm. Furthermore the W concentration peaks on the elevations of the surface structure, which is more pronounced at $\alpha = 45°$ (figure 6.6c) and $\alpha = 60°$ (figure 6.7c) and preventing further erosion. In the valleys the W concentration is lower because of re-deposition of sputtered Fe.

6.3.3 Surface Morphology Comparison

In this section the resulting surface morphology evaluated with TRI3DYN is compared to the AFM images of the experimental results, as shown in reference [42]. Figure 6.5 shows the resulting surface morphology after the total fluence of $4 \times 10^{23}\,\mathrm{m^{-2}}$ and by ion bombardment under normal incidence. The revealing surface pattern is very similar to the experiment, although the height of the structures cannot be reproduced by TRI3DYN and are by about a factor of two smaller (compare figure 6.5 (a) and (b)).

Figure 6.6 shows the modelled result under an angle of incidence $\alpha = 45°$. Here the surface pattern as well as the height of the revealing structures can be reproduced [43].

In figure 6.7 the results under an angle of incidence $\alpha = 60°$ can be seen. Here the surface pattern shows a pronounced ripple formation, where on elevated positions a strong surface enrichment of W is observable, which face the incident ion beam and prevent further erosion of the underlying material. Comparing the results to the experimental determined AFM image (figure 6.7a) show that the height of the structures can be reproduced here too.

Using the elemental depth information from RBS revealed nearly identical surface

pattern as show in figure 6.5 and figure 6.6 but with slightly higher structure height and thus a higher roughness R_q (as shown in figure 6.4). Due to this strong similarity, the structures are not shown here.

Figure 6.5 – Surface morphology after a total D fluence of $4 \times 10^{23} \, \mathrm{m}^{-2}$ for $250 \, \mathrm{eV}$ and under normal incidence (90° relative to the surface plane). In (a) the experimental AFM image (taken from [42]) of an irradiated sample is shown, while (b) displays the corresponding computational result of TRI3DYN, using XPS data as input. The color code in (a) and (b) is equivalent, revealing that the surface pattern in the experiment are higher, by a factor of two. (c) gives a cross-section through the middle of of the TRI3DYN voxel layer data (white dashed line in (b)), showing the resulting W enrichment at the surface [43].
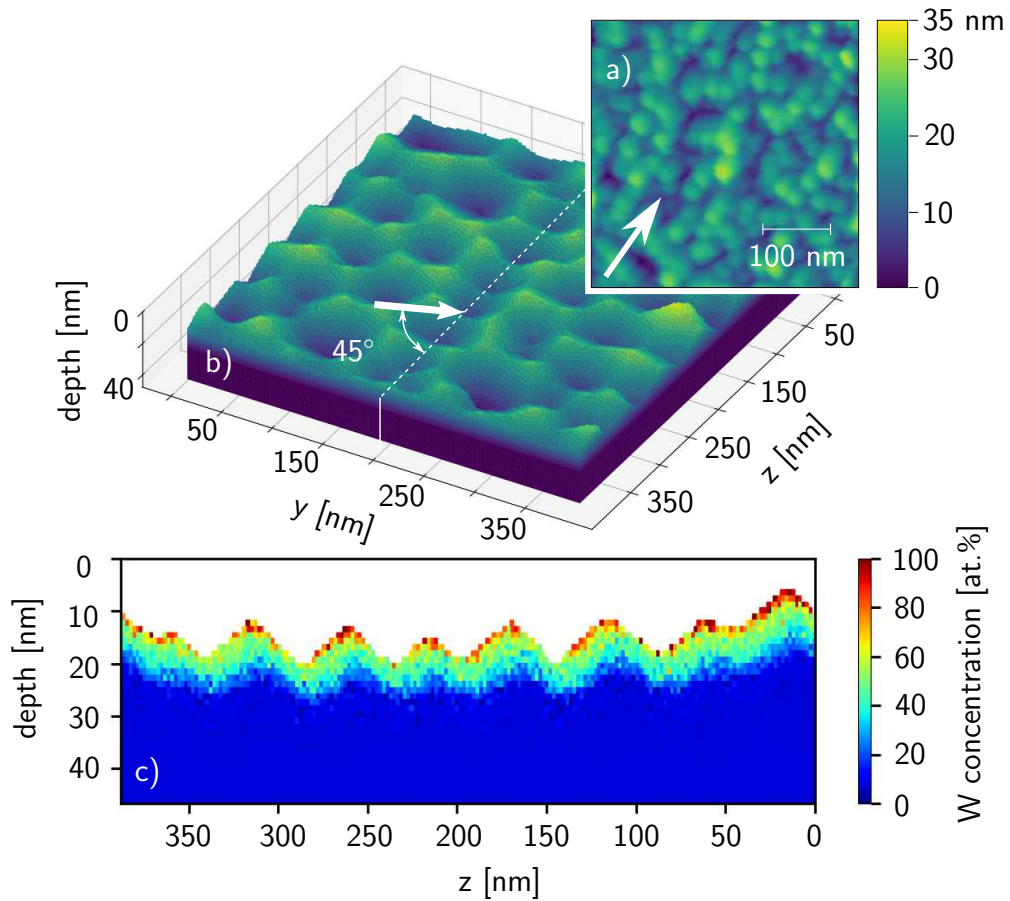
Figure 6.6 – Surface morphology after a total D fluence of 4×10^{23} m^{-2} for 250 eV and under 45° angle of incidence. The white arrows indicate the direction of the incident ion beam. In (a) the experimental AFM image (taken from [42]) of an irradiated sample is shown, while (b) displays the corresponding computational result of TRI3DYN, using XPS data as input. The color code in (a) and (b) is equivalent. (c) gives a cross-section through the middle of of the TRI3DYN voxel layer data (white dashed line in (b)), showing the resulting W enrichment at the surface, which acts as a protecting layer [43].
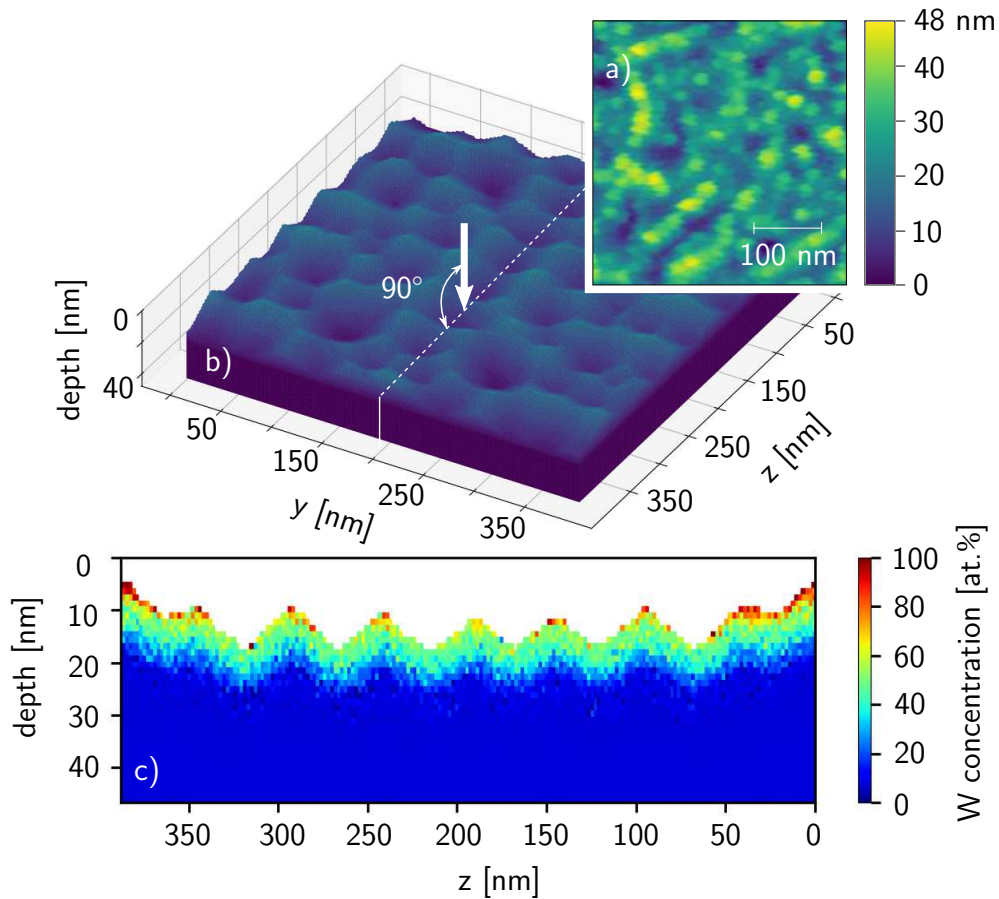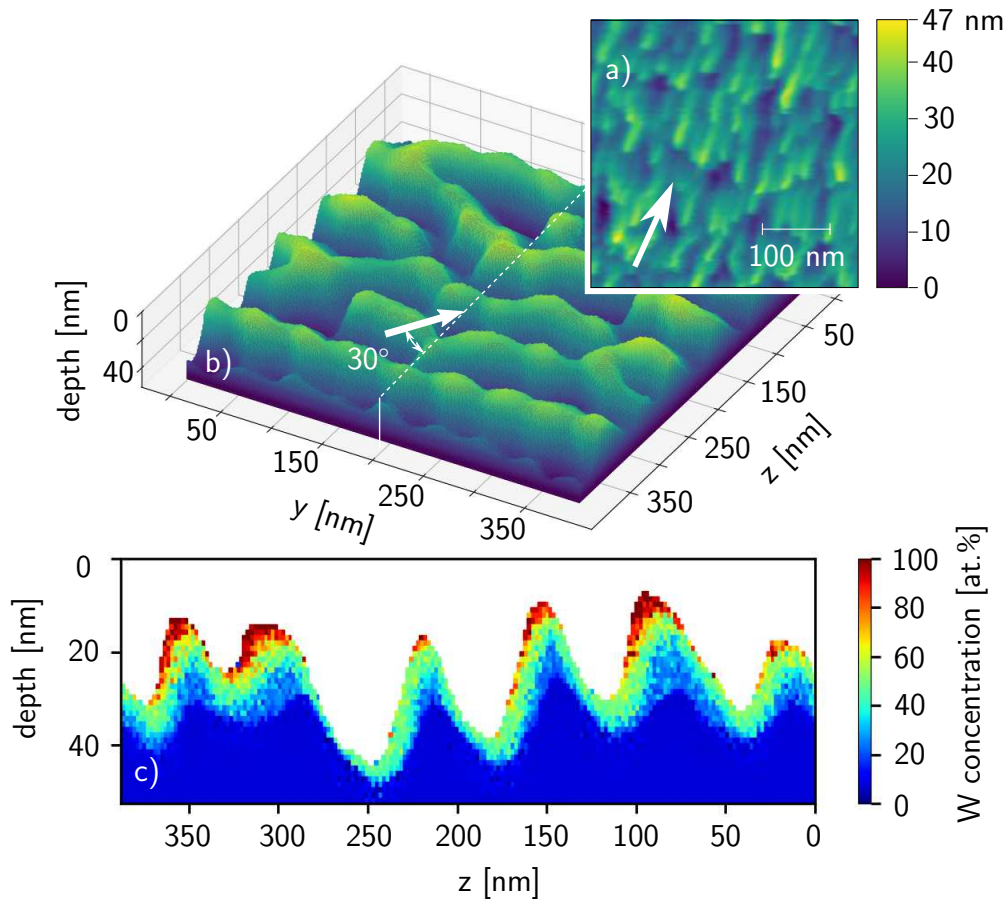
Figure 6.7 – Surface morphology after a total D fluence of $4 \times 10^{23}\,\mathrm{m}^{-2}$ for 250 eV and under 60° angle of incidence (30° relative to the surface plane). The white arrows indicate the direction of the incident ion beam. In (a) the experimental AFM image (taken from [42]) of an irradiated sample is shown, while (b) displays the corresponding computational result of TRI3DYN, using XPS data as input. The color code in (a) and (b) is equivalent. (c) gives a cross-section through the middle of of the TRI3DYN voxel layer data (white dashed line in (b)), showing the resulting W enrichment at the surface, which acts as a protecting layer.

6.4 Discussion

Figure 6.3 and figure 6.4 clearly demonstrate the necessity of precise elemental depth information in order to allow TRI3DYN to predict absolute sputtering yields as a function of ion fluence well. The drawback of RBS measurements is the lack of sensitivity to masses with low Z, like O and C and its limited depth resolution. Sputter-XPS on the other hand is a very surface sensitive technique. However since sputtering with Ar ions is used for depth profiling, this might lead to changes of the sample by the measurement. Therefore, the W concentrations in the sputter-XPS results in figure 6.1 are likely to be somewhat overestimated due to preferential sputtering (and consequently Fe concentrations are underestimated). The true elemental composition is probably between both measurements, as suggested by figure 6.3.

It is interesting to see, that TRI3DYN is actually able to reproduce the surface pattern from the AFM image quite well, as can be seen by comparing figures 6.5 to 6.7, (a) with (b). A modelled ion beam impinging the surface under normal incidence show structural heights, which are about a factor 2 too low compared to the experiment (compare with figure 6.5), but under 45° (figure 6.6) and 60° angle of incidence (figure 6.7), the structural heights also agrees quite good.

The strong ripple formation under 60° can also be reproduced with the software. The AFM image shows ripple formation in the ion beam direction, but on closer inspection also a formation of perpendicular mode ripples are observable. TRI3DYN reveals a structure were these perpendicular mode ripples formation is more pronounced.

Table 6.2 compares the resulting root-mean-square roughnesses R_q evaluated using TRI3DYN as well as real AFM images, after a applied fluence of $4 \times 10^{23} \, \mathrm{m}^{-2}$ D ions under different angles of incidence. The increase in roughness can be confirmed with TRI3DYN although the experimental value tends not to be reached. However, it must be pointed out that the AFM R_q values presented in table 6.2 are taken from reference [42] where $1 \, \mu\mathrm{m} \times 1 \, \mu\mathrm{m}$ images where used, but the modelled TRI3DYN surface need to be smaller.

Table 6.2 – Resulting surface roughnesses R_q using TRI3DYN and RBS as well as sputter-XPS elementary depth information and comparison to experimental determined roughnesses via AFM from [42].

angle of incidence	TRI3DYN RBS	TRI3DYN XPS	AFM (full image)
0°	4.5 nm	3.2 nm	8.6 nm
45°	5.1 nm	3.6 nm	6.4 nm
60°	5.9 nm	9.1 nm	10.5 nm

In figures 6.5 to 6.7 (c) a cross-cut of the resulting voxel-pile is given, revealing the local W concentration. On the elevations the W concentration tends to peak, preventing further erosion. In the valleys the W concentration is lower because of re-deposition of sputtered Fe. A closer look at the W concentration at the surface reveal an increased concentration in the $+z$ direction, because this is the ion beam facing side. Also the effect of shadowing of recessed areas can be observed, for the angle of incidence differing from normal incidence. At normal incidence the surface enrichment of W is less localized, which leads to a more even erosion of the surface. On the other hand, at an angle of incidence of $60°$, it leads to a strong localized surface enrichment of W, followed by a strong increase in roughness. The influence on the roughness of such localized W enrichment was also investigated by von Toussaint et.al. [118] using the 2D version of SDTrimSP. They confirm the severe increase in roughness, but the W clustering effect could not be reproduced, which may be caused by the 2D limitations of their code. The fact that TRI3DYN does not consider diffusion indicate that this effect tends to play no role at least at room temperature.

6.5 Summary

The TU Wien QCM technique is a powerful tool to investigate the dynamics of sputtering processes with high precision. This allows to benchmark 3D MC-BCA codes like TRI3DYN or SDTrimSP-3D. In this chapter a comparison with TRI3DYN was performed. As a test case Fe-W model films were taken, sputtered with a D ion beam at $250\,\mathrm{eV}$ impact energy under an angle of incidence of $0°$, $45°$ and $60°$ and up to a fluence of $4 \times 10^{23}\,\mathrm{m^{-2}}$. It could be demonstrated that by including initial information about the surface morphology of the sample in combination with precise elemental depth profiles, TRI3DYN is capable of forecasting the outcome of experiments. Modification of the surface morphology during sputtering is clearly reflected in the sputtering behaviour, which cannot be modelled with a 1-dimensional BCA code like TRIDYN. TRI3DYN instead, can reproduce the experimentally observed surface morphology changes, including the increase in surface roughness. Surprisingly even rather low initial (RMS) roughnesses in the nm range have a significant influence on the sputtering behaviour. The possibility to use a voxel pile as input for a realistic surface, also allows to simulate the sputtering of more complex nanostructures, like W-fuzz, which will be presented in chapter 7 [44, 119]. The huge computation time, however, limits these simulations to areas with rather small lateral extensions [43].

<div style="text-align: right;">**7**</div>

Results on the Erosion of Nanostructured Tungsten

The contents of the following chapter have been published in reference [45].

In this chapter the erosion of nanostructured tungsten (so-called W-fuzz) under Ar irradiation was investigated, by using the QCM in catcher configuration. In section 7.3.2 the experimental results were compared to a novel modelling approach (section 7.2.3.1), using the full 3D code TRI3DYN. Pre and post irradiation analysis of the W-fuzz samples were done by SEM and presented in section 7.2.1 and 7.3.

7.1 Preface

The most important parameters of a plasma facing material (PFM) are a low sputtering yield due to particle impact, a high melting point and low fuel retention. Tungsten (W) meets all these properties and is therefore the material of choice in today's fusion reactors [23, 38]. Under special conditions, however, a W surface can form nanometer-sized fibrous structures, also called tungsten-fuzz (W-fuzz). Such nanostructures are forming under high flux helium bombardment at low energies and at temperatures in the range of $900 - 2000\,\mathrm{K}$ [119–124]. Since these structures are highly porous, thermal transfer is reduced, which may led to melting of the PFM, in particular in the divertor region (compare with chapter 1.2.2) of a nuclear fusion device, as here the highest heat loads are expected [119, 121, 125]. Furthermore, there is general concern that W-Fuzz might be easily sputtered and causes a strong "high-Z" contamination of the fusion plasma, which contributes to cooling and degrades its performance [123, 125, 126]. Furthermore, sputtering

of such nanostructures by ion bombardment is less understood and therefore more investigations are required [45].

7.2 Material and Methods

7.2.1 Sample Preparation and Analysis

Samples of W-fuzz were produced and prepared at the FZJ, at the PSI-2 linear plasma device [122, 127]. This was done by exposing polycrystalline W bulk material to a He plasma at temperatures around $950\,\mathrm{K}$. There, a He ion flux of about $10^{21}\,\mathrm{m^{-2}s^{-1}}$ leads to the growth of nano-structured W [119, 122]. The precise processing parameters and conditions can be found in reference [122]. The samples have been analysed by using SEM at the HZDR as well as at the FZJ. Figure 7.1a shows a typical SEM image of one of the W-fuzz samples, where the nanostructured surface is clearly visible. A more detailed analysis of this image, by using the image processing software ImageJ, revealed an areal density of 50% and a string thickness of about $40\,\mathrm{nm}$ [45, 93].

(a) top-view SEM   (b) 54° inclined SEM with FIB-cut
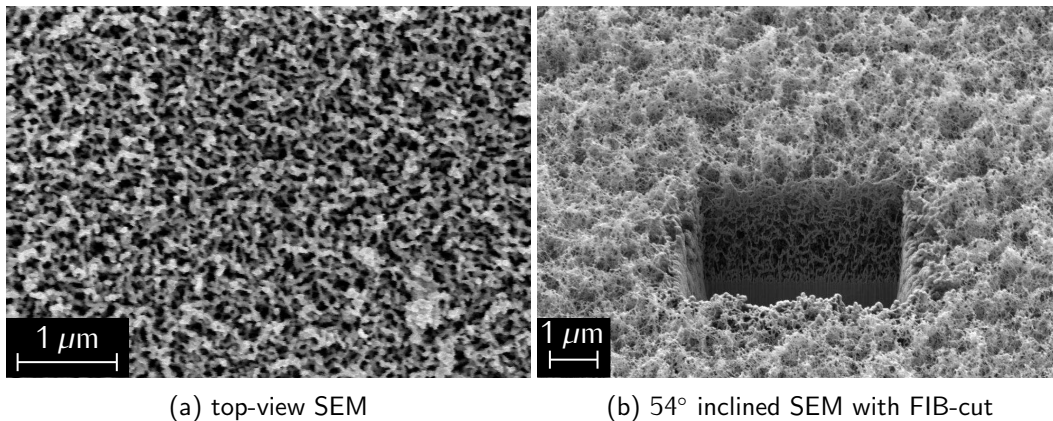
Figure 7.1 – SEM images of a W-fuzz sample showing the fuzzy nanostructures. In (a) a top-view SEM image can be seen, revealing an areal density of 50% and a string thickness of about $40\,\mathrm{nm}$. (b) shows a tilted SEM image by 54° and a FIB-cut spot revealing the underlying nanostructure material, which was conducted by a Ga ion beam with $30\,\mathrm{keV}$. A thickness of the fuzzy region of about $2\,\mu\mathrm{m}$ could be evaluated. Figures taken from [45].

In figure 7.1b a SEM image is presented, showing a FIB-cut SEM measurement of a virgin W-fuzz sample, where a Ga ion beam with an energy of $30\,\mathrm{keV}$ was used to cut into the fuzz material (see also chapter 4.2.1 for more details of this technique). This image is tilted by 54°, where the cross section through the W-

fuzz is presented very nicely. By processing the image with ImageJ, a W-fuzz height of about $2\,\mu$m could be assessed [45].

7.2.2 Experimental Approach

As experimental setup the QCM in catcher configuration was used. The detailed setup schematics and description can already be found in chapter 4.1.3, where the catcher technique is presented in detail in 4.1.4. The schematics of the experimental setup used for the W-fuzz erosion measurements can be seen in chapter 4.1.4, figure 4.9.

The used sputter ion source provides a focused and mass filtered Ar^{1+} ion beam, with a kinetic energy of $2\,$keV and an average ion flux of $\Phi \approx 10^{17}\,$m^{-2}s^{-1}. The built-in lens system and deflection plate pair allows focussing in the 0.1 mm range and ion beam scanning in the mm range.

The sample holder of the catcher-QCM is mounted on a linear stage which allows precise positioning of the distance d to the sample. It also ensures, that the catcher-QCM is always positioned parallel to the impact point of the ion beam. The relative position Δx is adjusted via the primary sample holder. The catcher-QCM uses quartz crystal samples on which the Au surface were pre-coated with $200\,$nm W, to avoid weaker signal and dynamic effects due to different sticking on Au and W [45].

7.2.3 Simulation Approach

The state-of-the art 3D sputter modelling software TRI3DYN was used here for simulations, as it allows to model the erosion of nearly any structured and nanostructured surface. This software and its functionality is presented in chapter 3, section 3.4. The performance of the code has been successfully demonstrated already in chapter 6, where a closed surface morphology was modelled.

This code uses so-called 'pseudoatoms' as projectiles, representing a certain amount of real projectiles. As TRI3DYN is a MC code, a high statistical accuracy can only be achieved by using a high number of pseudoatoms. For the evaluation of static sputtered and scattered particles distributions of the fuzz-modelling, a pseudoatom to real atom factor of 1 was used. To keep the computing time within limits, a factor of 200 had to be used for the dynamic erosion modelling, which includes changes in the sputter target. To avoid inaccuracies due to the discretization of a real sputter target, the voxel resolution should be as high as possible. However, a high number of voxels increases the computation time enormously, so the lateral extent of the modelled object is limited. A good compromise is to use a voxel

size that is approximately the length of the expected collision cascade [43]. The simulations presented in this chapter used a voxel size of $50 \times 50 \times 50 \, \text{Å}^3$ [45].

7.2.3.1 Creation of a W-fuzz model

Informations of the SEM images of the W-fuzz samples were used to create an adequate W-fuzz model target. By analysing these images (figure 7.1a and 7.1b) via the image processing software ImageJ, a string thickness of about $40 \, \text{nm}$ and an areal density of 50% could be evaluated. These two parameters were then used as the basis for a 'random-walk' algorithm that allows individual W strings to grow out from flat surface, with the lateral starting point as well as the polar and azimuthal direction chosen randomly. After a growth length of twice the string thickness, the growth direction is again varied randomly. When such a string has reached a maximum height, a new string begins to grow. This process is repeated until the measured areal density of 50% is reached. The resulting randomly generated W-fuzz target for TRI3DYN can be seen in figure 7.2. This target was also used for modelling in this chapter, where pure W was assumed as elemental composition of the target. Is should be noted, that the code uses periodic boundary conditions in both lateral directions (Y and Z coordinates).

The SEM images revealed a total W-fuzz height of $2 \, \mu\text{m}$ (figure 7.1b), which is unfortunately to big to be modelled. Therefore, the modelling was limited to a maximum total fuzz volume of $0.5 \times 0.5 \times 0.5 \, \mu\text{m}^3$ [45].

7.2.3.2 Reconstruction of the QCM catcher measurements

An attempt was made to reconstruct the QCM catcher signal by using sputtered and scattered particles distributions. Taking into account the geometric layout of the experimental setup (see figure 4.9 in chapter 4), including the angle of incidence of the impinging ion beam α, the distance d of the catcher to the ion beam hit point, beam scanning, as well as the sensitivity s of the quartz crystal disc, the QCM-catcher signal Y_{total} can be calculated for every Δx position. The detailed procedure of the catcher reconstruction is presented already in chapter 4, section 4.1.4.2 or can also be found in reference [45].
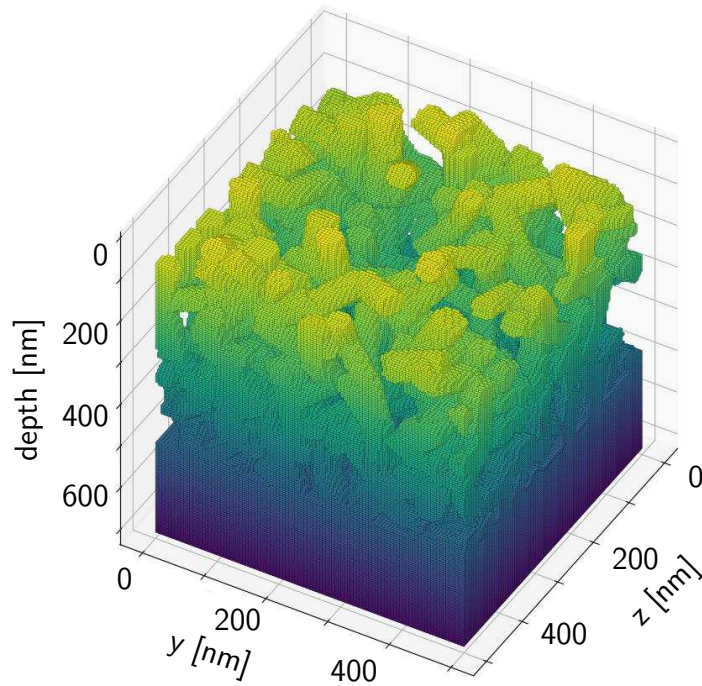
Figure 7.2 – A 3D plot of the W-fuzz structure as used for TRI3DYN simulations. The structure was randomly generated by using string thickness and areal coverage density information extracted from SEM images from W-fuzz samples. The depth dependent color code highlight the 3D structure. A total fuzz volume of $0.5 \times 0.5 \times 0.5\,\mu\text{m}^3$ was used here, were a voxel size of $50 \times 50 \times 50\,\text{Å}^3$ had to be used. The code uses periodic boundary conditions in both lateral Y and Z directions. Underneath the fuzz structure, 40 filled voxel layers of pure W were placed to prevent non-physical transmission of particles through the bottom. Figure taken from [45].

7.3 Results

The W-fuzz samples were stepwise irradiated with Ar^{1+} ions at $2\,keV$, where the size of the fluence steps are listed in table 7.1. Subsequently after each step the QCM-catcher method was used to measure the absolute catcher yield Y_c, which is related to the sputtered particle distribution (figure 7.10).

Table 7.1 – total applied fluences to W-fuzz sample after step 1 and 2

step no.	Ar^{1+} fluence $[m^{-2}]$
1	$8.6 \pm 0.9 \times 10^{20}$
2	$1.76 \pm 0.18 \times 10^{22}$

SEM images of the irradiated W-fuzz sample were made after fluence step 1 and 2. Figure 7.3 shows the W-fuzz surface after fluence step 1. Fuzzy nanostructures are still visible, but also the formation of grooves in the ion beam direction can be seen [45].
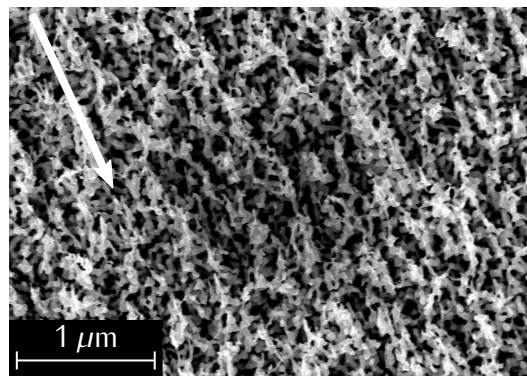

Figure 7.3 – SEM image of the W-fuzz sample, revealing the surface structure after an Ar^{1+} fluence of $8.6 \times 10^{20}\,m^{-2}$ (after step 1). The white arrow indicates the direction of the incident ion beam. W-fuzz structures are still observable, but also a grove formation in the direction of the ion beam. Figure taken from [45].

In figure 7.4a a top-view SEM image can be seen, after fluence step 2, showing a transition region from unsputtered to sputtered W-fuzz. In the lower left part of the image the typical nanostructures are visible, while in the upper right part a scale-like surface structure is visible. Small periodic cones are observable, aligned in the direction of the impinging ion beam. In figure 7.4b shows a magnification of the sputtered region, revealing the scaly structure more clearly. A investigation of this image by using the software ImageJ, a scale thickness of $216 \pm 48\,nm$ and a length of $390 \pm 141\,nm$ could be evaluated (error values correspond to the FWHM of the distributions) [93].

An inclined SEM image by an angle of $56°$ (figure 7.5a), which is nearly the ion impact angle of $60°$, shows that the base of the cones is nearly round, with a diameter of $307 \pm 73\,\text{nm}$. To check whether there is sill a W-fuzz structure underneath the scaly surface, a FIB-cut SEM was made, where its result can be seen in figure 7.5b. Some melting of the material is visible at the edges, but any underlying W-fuzz structure could no longer be found [45].
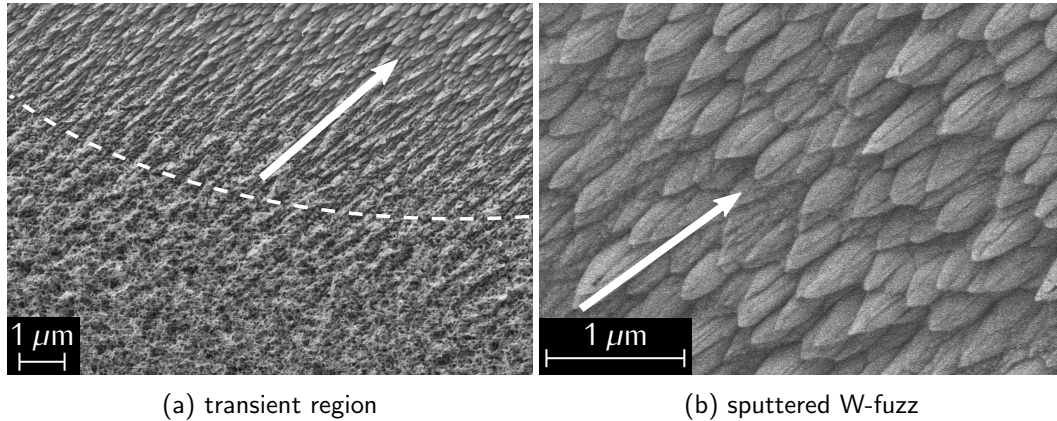

<div align="center">(a) transient region   (b) sputtered W-fuzz</div>

Figure 7.4 – SEM images of the W-fuzz sample after a total Ar^{1+} fluence of $1.76 \times 10^{22}\,\text{m}^{-2}$. In (a) a transient region from unsputtered (lower left) to sputtered area (upper right) is shown. A boundary region is visible and is indicated by a dashed white line. The sputtered area shows a scaly structure, where the tips point in the direction of the incident ion beam (beam direction indicated by the white arrow). (b) shows a magnified SEM image of the sputtered W-fuzz area, revealing small periodic cones that are similar to fish scales and aligned in the direction of the ion beam. Figures taken from [45].

7.3.1 TRI3DYN Modelling Results

TRI3DYN in static mode was used to compare sputtered and scattered particles distributions of a perfectly flat W surface with a W-fuzz structure from figure 7.2. In figure 7.6 the resulting sputtered particles distribution can be seen, by modelling an impinging ion beam under an angle of incidence of $60°$ (with respect to the surface normal). By using in total 2.5×10^7 pseudoparticles good statistics is ensured.

The modelled flat target in figure 7.6a show a pronounced sputtered particles distribution in forward direction, where a single knock-on peak around $-50°$ is observable. The modelled W-fuzz target instead (figure 7.6b), show a distribution with a strong back-sputtering, in the direction of the incoming ion beam. A maximum at around $35°$ is observable [45].
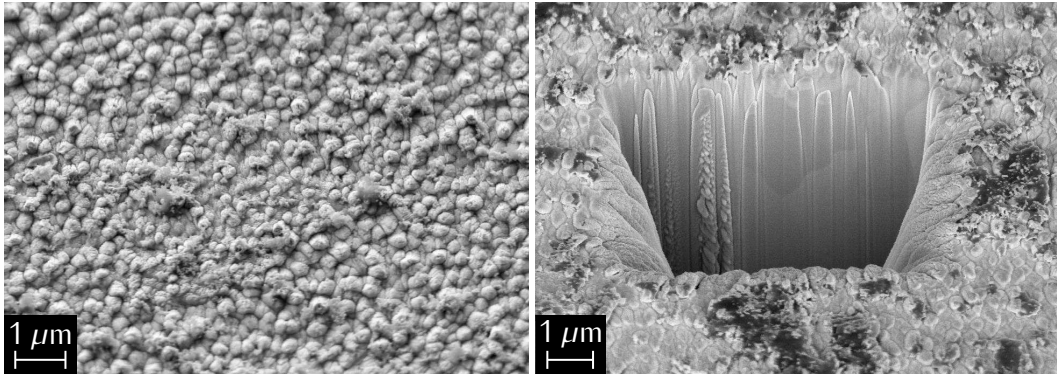
(a) 56° inclined SEM

(b) 56° inclined SEM with FIB-cut

Figure 7.5 – Tilted SEM image of the sputtered W-fuzz sample after an Ar^{1+} fluence of 1.76×10^{22} m^{-2}, where a tilt angle of 56° was used. This angle is close to the angle of incidence of the impinging ion beam (60°). In (a) the cones of the scaly surface can be seen, pointing directly in the direction of the observer. (b) shows a FIB-cut SEM image of the sputtered W-fuzz sample, where no underlying fuzz structure can be found any more. Figures taken from [45].
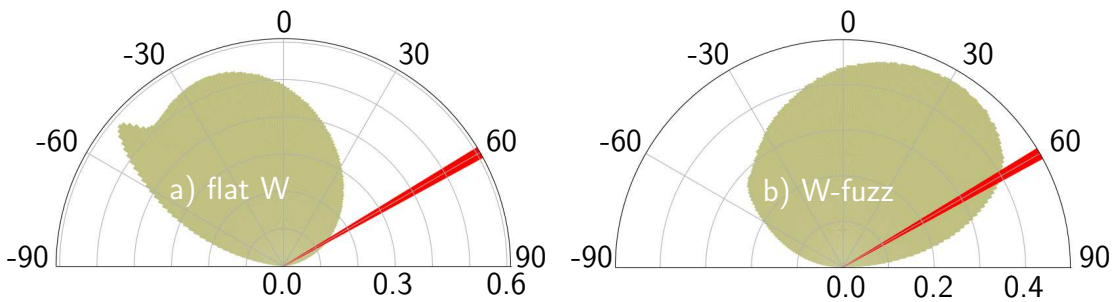

Figure 7.6 – Sputtered particles distributions modelled with TRI3DYN. The impinging Ar ion beam is marked as red arrow, hitting the surface under an angle of incidence of 60°. In (a) the results of using a flat W target is shown, while in (b) the results of the W-fuzz model is shown. A binning of 1° was used and the total distributions were normalized. Figures taken from [45].

The modelled results of the scattered projectiles distributions are shown in figure 7.7 and show a similar outcome compared to the sputtered particles distribution. The flat target (figure 7.7a) show a clear forward scattering an a single scattering peak at around $-30°$. The fuzz target show a broad distribution with a slightly pronounced back-scattering, in the direction of the incident ion beam. The maximum can be seen around $35°$, but also a clear single-scattering peak in forward direction is observable too, at $-30°$. The shown distributions were all normalized [45].
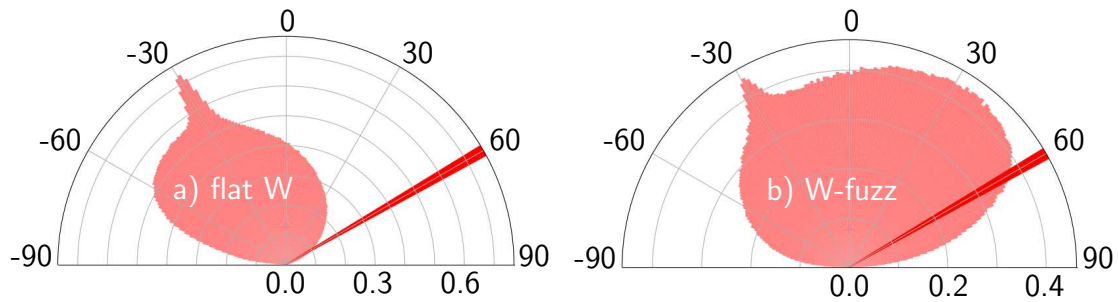

Figure 7.7 – Sputtered particles distributions modelled with TRI3DYN. In (a) the results of using a flat W target is shown, while in (b) the results of the W-fuzz model is shown. The impinging ion beam is marked as red arrow, impinging at $60°$. A binning of $1°$ was used and the total distributions were normalized. Figures taken from [45].

TRI3DYN is also capable of dynamic erosion modelling of a nanostructured surface. The initial structure, as presented in figure 7.2, was exposed to a uniform distributed Ar^{1+} ion beam, with a kinetic energy of $2\,keV$ and impinging under an angle of incidence of $60°$. The modelled results after a fluence of $1 \times 10^{21}\,m^{-2}$ (after step 1) can be seen in figure 7.8 under different points of view. The underlying fuzzy nanostructure is still observable, but also formation of grooves in the direction of the impinging ion beam is already observable.

One can also see that some voxel-cluster stay at elevated positions above the surface, but it must be noted that periodic boundary conditions are used. A seemingly floating voxel-pile at the end of one coordinate might be connected to the bulk at the opposite end. Nevertheless the limit of the underlying physical model need to be considered, as for example gravity is not included [45].

Figure 7.9 shows the modelled W-fuzz after an Ar fluence of $1.7 \times 10^{22}\,m^{-2}$ (after step 2). The nanostructures cannot be observed any more, where the surface pattern changed to a scale like morphology. The tips of these structures point in the direction of the impinging ion beam. The image processing software ImageJ was used to analyse the resulting morphology further [93]. A thickness of the scales at its origin of $76 \pm 46\,nm$ and a scale length of $296 \pm 102\,nm$ can be found (by including also the periodic boundary conditions) [45].
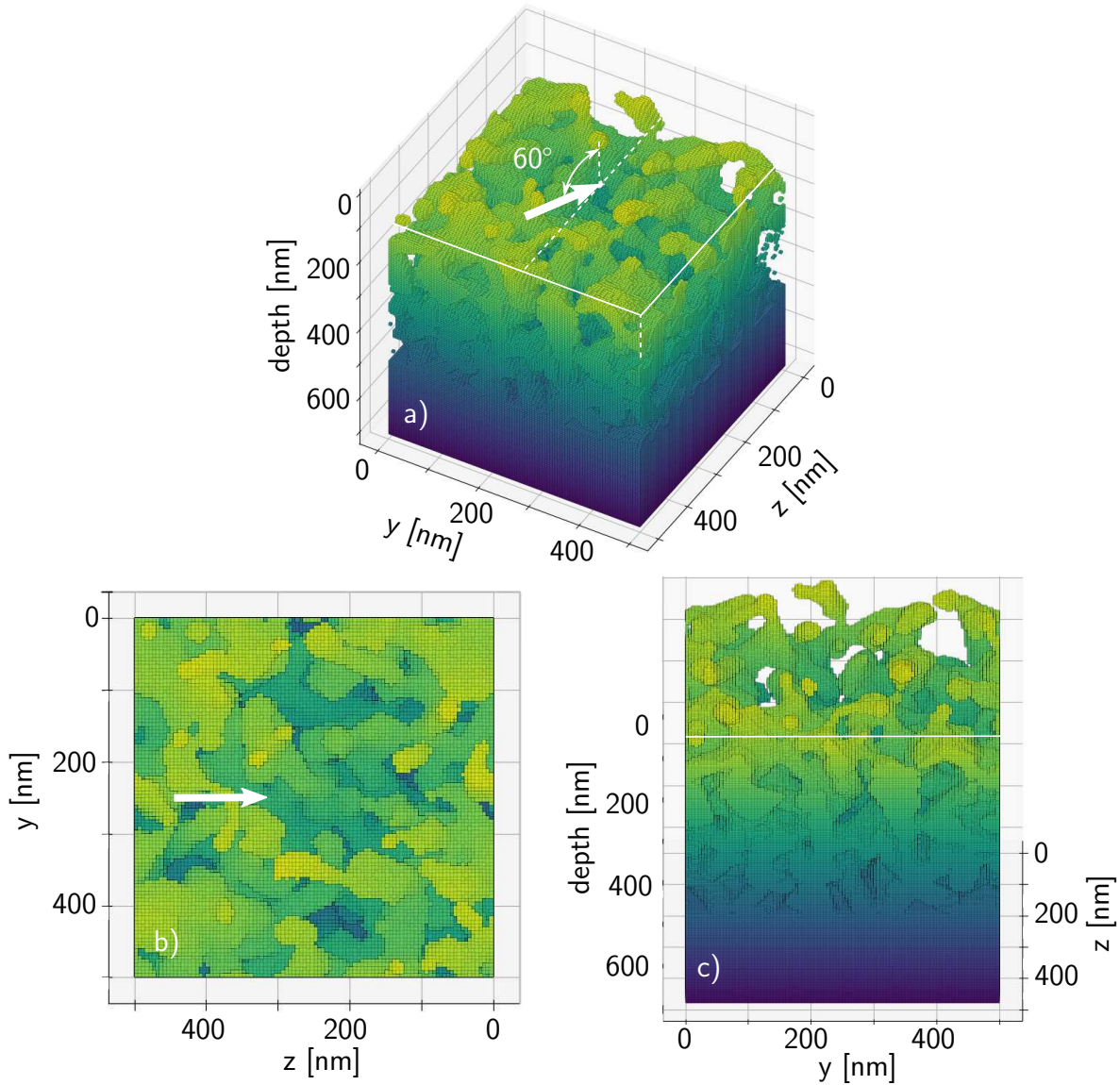
Figure 7.8 – Dynamic erosion modelling result of TRI3DYN, after an Ar fluence of $1 \times 10^{21}\,\mathrm{m}^{-2}$. Nanostructures are clearly visible, but also a slight alignment of the structure in the direction of the impinging ion beam (show as white arrow). In (a) a perspective view of the resulting 3D structure is shown. (b) shows a top view and in (c) the 3D structure is inclined by $60°$, so that the observer can see the structure from the angle of the incoming ion beam. A solid white line marks the edge of the surface. Figures taken from [45].
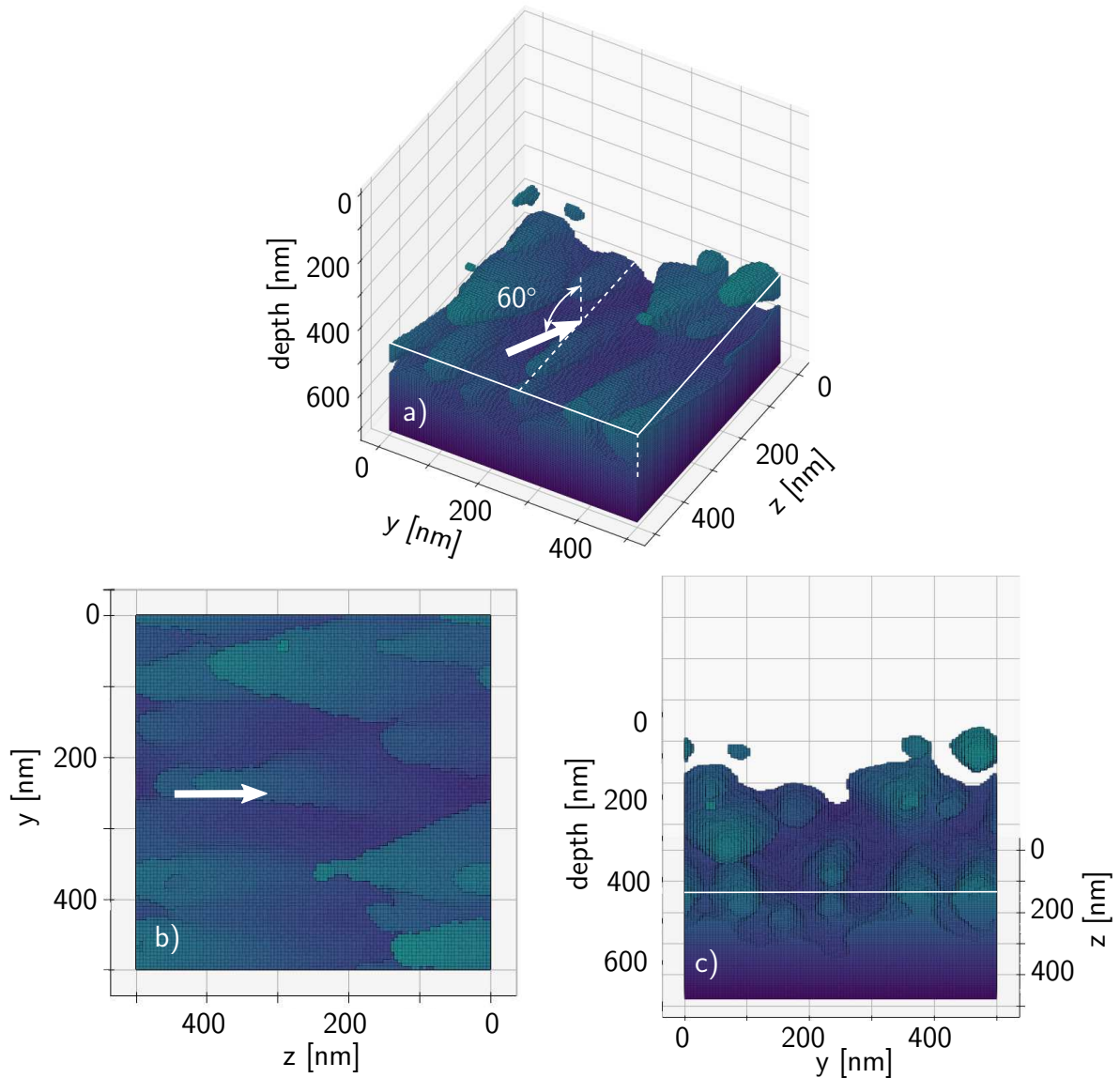
Figure 7.9 – Dynamic erosion modelling result of TRI3DYN, after an Ar fluence of $1.7 \times 10^{22} \, m^{-2}$. A scale-like surface morphology can be seen, where the cones point directly in the direction of the incident ion beam (indicated as white arrow). In (a) a perspective view of the resulting 3D structure is shown. (b) shows a top view and in (c) the 3D structure is inclined by 60°, so that the observer can see the structure from the angle of the incoming ion beam where the peaks of the scales point in the direction of the observer. A solid white line marks the edge of the surface. Figures taken from [45].

The resulting surface morphologies modelled with TRI3DYN are in good agreement with the SEM images. The SEM images of the W-fuzz after applying an Ar fluence of $8.6 \times 10^{20}\,\mathrm{m^{-2}}$ (after step 1) shows, that the fuzzy nanostructures are still visible (figure 7.3), which can be confirmed by TRI3DYN (figure 7.8). Even though the TRI3DYN W-fuzz model is limited to a lateral expansion of $0.5 \times 0.5\,\mu\mathrm{m^2}$, a beginning formation of grooves in the direction of the impinging ion beam can be seen.

After applying an Ar fluence of $1.7 \times 10^{22}\,\mathrm{m^{-2}}$ (after step 2) no underlying fuzzy nanostructures can be found any more, as can be seen in the FIB-cut SEM image in figure 7.5b. This is also confirmed by the TRI3DYN modelling, as can be seen in figure 7.9, although in the simulation only $0.5\,\mu\mathrm{m}$ ($50\,\text{Å} \times 100\,\mathrm{voxels}$) of fuzz have been sputtered away. In the experiment as well as in TRI3DYN a scaly surface morphology is revealed. A detailed investigation of the length and thickness of these scales showed, that TRI3DYN revealed comparable, but considerably smaller structures compared to the experimental results. This is most likely due to the lower fuzz volume in the model [45]. In the supplementary online material of reference [45] a fluence dependent animation of the simulation can be found (`https://doi.org/10.1016/j.jnucmat.2020.152019`).

7.3.2 QCM Catcher Results and Comparison to Modelling

The results of the measured total QCM catcher experiments at different positions of Δx can be found in figure 7.10 and figure 7.11. The first figure compares the measured QCM catcher yield of a flat W sample to W-fuzz samples in initial stage, as well as after two irradiation steps with $2\,\mathrm{keV}\,\mathrm{Ar^{1+}}$ impinging under an angle of incidence of $60°$. The height of the fluence steps can be found in table 7.1.

The catcher yield results of a flat W sample revealed a maximum of the distribution at $\Delta x = 0\,\mathrm{mm}$, with a yield of $0.13 \pm 0.03\,\mathrm{W/Ar}$. The results of the virgin fuzz sample shows a distribution with a maximum around $\Delta x = +6\,\mathrm{mm}$ with a catcher yield of $0.007 \pm 0.001\,\mathrm{W/Ar}$. This is only about 5% of the flat sample results. After each fluence step a continuous increase in the W-fuzz catcher yield is observable and approaches the measured distribution of the flat W-sample. Deviations at negative Δx values can be observed, which could be caused by the resulting smaller scales at the surface.

Figure 7.11 shows the virgin W-fuzz behaviour in more detail (black dashed area from figure 7.10). The experimentally evaluated distribution has a maximum at about $\Delta x = +6\,\mathrm{mm}$. An inset in figure 7.11 shows a precise setup schematics at this Δx position. One can see that the surface normal from the sample points
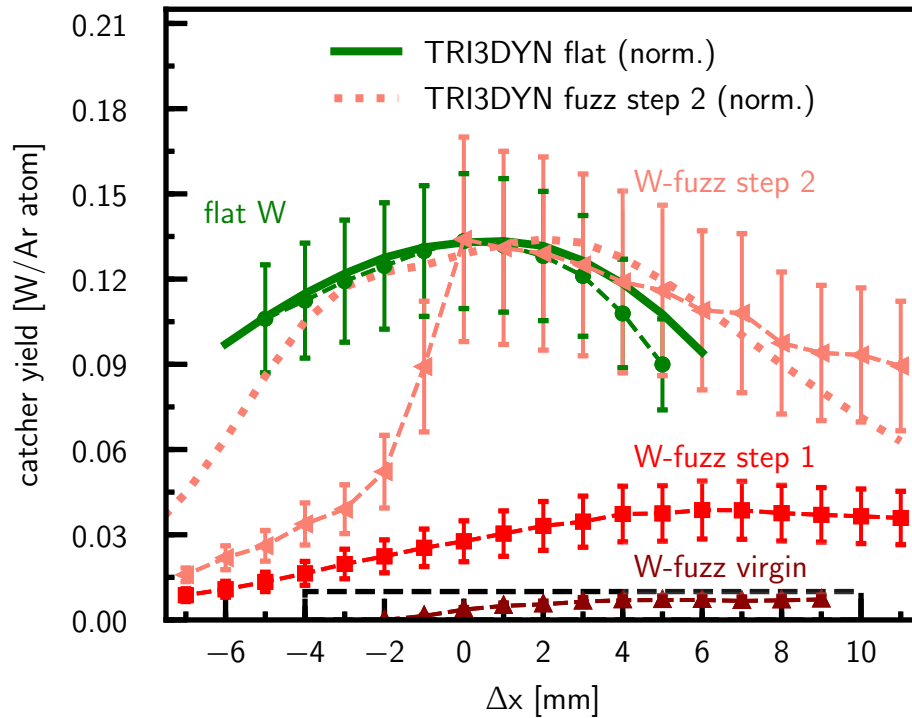
Figure 7.10 – Comparison of QCM catcher measurement results (symbols) of a flat W sample (green), a W-fuzz target in initial state and after two erosion steps (dark-red to to light-red), as well as comparison to TRI3DYN results. A catcher yield maximum of the flat sample can be seen at $\Delta x = 0\,\text{mm}$, whereas the virgin fuzz and the fuzz target after applying fluence step 1, show a much smaller catcher yield, with a maximum around $\Delta x = +6\,\text{mm}$. After eroding the fuzz sample further (fluence step 2), the measured catcher yield approaches that of the flat sample. TRI3DYN reproduces the trend of the catcher yield of a flat W target (green solid line) and also the W-fuzz target after fluence step 2, despite the fact that some deviations at negative Δx is observable (compare light-red triangles with light-red dotted line). Figure taken from [45].

directly towards the center of the catcher QCM, indicating that sputtering of material occurs preferentially in this direction [45].

The usage of the TRI3DYN sputtered and scattered particles distribution allows to make an attempt to reconstruct the measured catcher yield, as presented in chapter 4, section 4.1.4.2. The behaviour of a flat target can be quantitatively reproduced, as can be seen in figure 7.10 (solid green line). The measured behaviour of a fuzz sample instead, shows some deviation of the maximum position of the catcher yield, as can be seen in figure 7.11 (solid dark-red line). Here a maximum was found at $\Delta x = +2$ mm.

After a simulated erosion of 1.7×10^{22} m^{-2} (surface from figure 7.9) the reconstruction of the catcher yield signal agrees well with the measured results at $\Delta x \geq 0$ mm, as can be seen in figure 7.10 (dotted light red line).

Another attempt was made to reconstruct the catcher yield by assuming the simplest approach of isotropic emission of sputtered particles, using a cosine sputter distribution, according to equation 7.3.1, where γ is equivalent to a polar shift [61]. The results can be seen in figure 7.11 as highlighted in blue. By using a polar shift of $\gamma = 60°$, (in the direction of the incident ion beam), still deviations in forward sputter directions are observable (figure 7.11 blue-dashed line). Instead by using a $\gamma = 45°$, the reconstruction of the catcher yield is in good agreement with the measured initial W-fuzz sputtering behaviour (figure 7.11 blue-dotted line) [45].

$$f_{sp,sputtered}(\Omega(\Theta, \Phi)) = cos(\gamma + \Theta) \qquad \gamma = \{60°, 45°\} \qquad (7.3.1)$$

A separate control experiment with the QCM technique in classic configuration (see chapter 4, section 4.1.3) was performed, where a quartz crystal disc with a thin layer of W was directly exposed to an Ar^{1+} ion beam with 2 keV and under an angle of incidence of 60°. An absolute sputtering yield of 2.05 ± 0.28 W/Ar could be evaluated here.

Taking the data from the catcher measurements, where a factor of 17 lower signal was found for the fuzz measurements, and by including a geometric factor, which considers the increased target-catcher distance at $\Delta x = +6$ mm, a W-fuzz sputtering yield of 0.12 ± 0.07 W/Ar can be approximated.
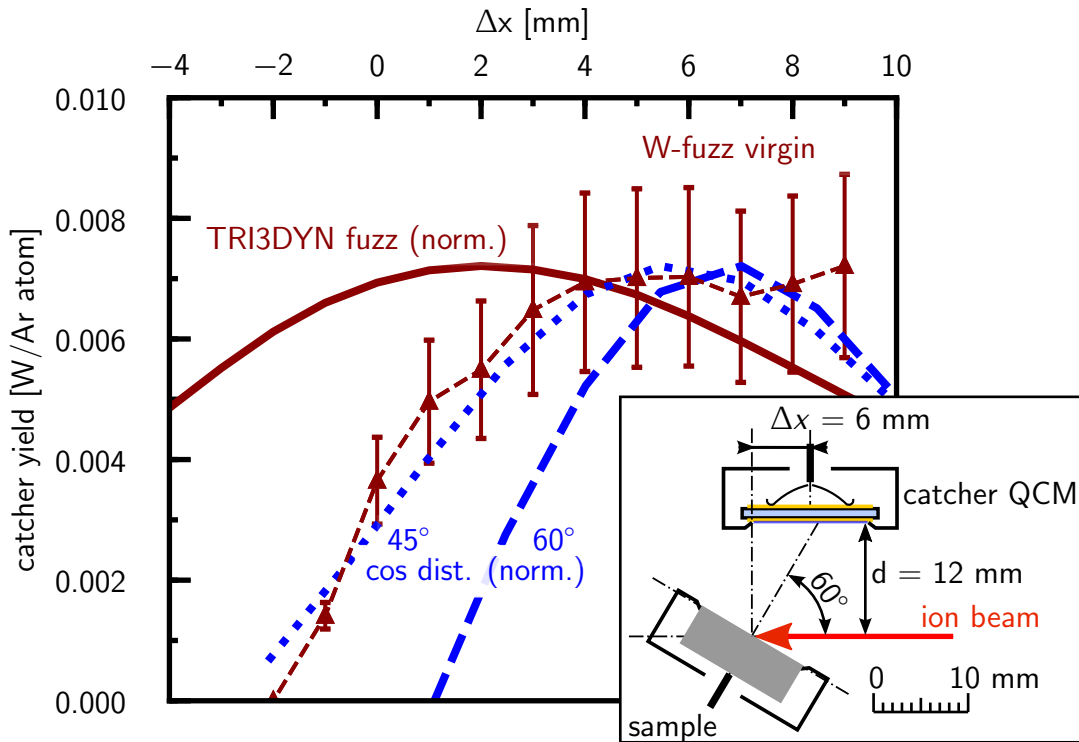
Figure 7.11 – Comparison of QCM catcher measurement results (symbols) of a virgin W-fuzz target to modelling with TRI3DYN and numerical approaches using a cosine distribution. A maximum of the measured catcher yield was found at around $\Delta x = +6$ mm of 0.007 ± 0.001 W/Ar. The inset shows the setup schematics at $\Delta x = +6$ mm and $d = 12$ mm. Here the surface normal of the sample points directly towards the center of the catcher QCM, indicating that sputtering of material occurs preferentially in this direction. Reconstruction using TRI3DYN results show a maximum at $\Delta x = +2$ mm. By using a sputtered particles distribution following a cosine distribution, including a polar shift of $\gamma = 45°$ (equation 7.3.1) the measured distribution can be reproduced. The reconstruction attempts were normalized to the maximum of the measured catcher yield. Figures taken from [45].

7.4 Discussion

The QCM-catcher technique shows a sputtered particle distribution of W-fuzz, which is peaking in the direction of the surface normal of the sample. A comparison to the catcher yield of a flat W sample revealed an approx. 17 times lower catcher yield (see figure 7.10 and 7.11). Other groups also confirm a W-fuzz sputter yield that is one order of magnitude lower compared to a flat target [125]. This indicates strong redeposition of sputtered material inside a fuzzy nanostructures, leading to a lower sputtering yield. Furthermore, sputtered particles seem to be able to exit the fuzz surface preferably only in the direction of the incident ion beam, since only here a path to the surface is open [125].

Erosion of the W-fuzz sample by applying a high Ar fluence, the measured total capture yield approaches that of a smooth sample, but deviations in negative Δx values can be observed. SEM measurements of the fuzz samples performed after irradiation reveal the formation of a scaly structure pointing in the direction of the impinging ion beam. These structures still lead to a repositioning of the sputtered material and may shield the QCM catcher at negative Δx values [45].

In this chapter a first attempt was made to model the erosion of a nanostructured material by using the code TRI3DYN. The modelled dynamic erosion of the W-fuzz structure can reproduce the formation of a scaly surface morphology, which can be seen by comparing figure 7.9 to 7.4b. Modelling of the sputtered and scattered particle distributions show clearly that a fuzzy surface causes severe 'backward' sputtering and also projectile scattering in the direction of the ion beam [45].

An attempt was made to reconstruct the QCM catcher measurements by using these distributions. Deviations to the experimental results are observable, as can be seen in the figure 7.10 and figure 7.11. This deviation is caused by too much forward scattering and sputtering, which in turn may be caused by a too simple model of the W-fuzz. The assumption that every voxel in the TRI3DYN fuzz model includes pure W with a surface binding energy of a bulk W material may not hold true for a nanostructured material.

Although the analysis of the SEM images revealed a porosity of about 50%, other groups measured by weight loss techniques a porosity of about 90% [122, 123]. Therefore it can be concluded that fuzzy nanostructures might have additional porosity. Unfortunately, this is beyond the capabilities of TRI3DYN, because modelling of such finely resolved structures in the size of the modelled volume would require a much higher voxel resolution. This would lead to a tremendous increase in computing time, where no reasonable result in a realistic time would be possible yet.

Although the assumptions for the TRI3DYN model are simple, the comparison to the experiment demonstrated the power of MC-BCA codes and shows that the inclusion of surface morphologies is essential [45].

7.5 Conclusion

This chapter points out the capabilities of the TU Wien QCM catcher technique, as it allows to investigate in-situ the erosion of nearly any sputter target independent of its surface morphology.

Irradiation of a W-fuzz sample with an Ar^{1+} ion beam under an angle of incidence of $60°$, at $2\,keV$ revealed pronounced backward sputtering and an absolute W-fuzz sputtering yield of $0.12 \pm 0.07\,W/Ar$ could be approximated.

Continuous erosion of the W-fuzz leads to an increase in the catcher yield and also a shift of the measured yield distribution, approaching the behaviour of sputtering a flat W sample. Subsequent SEM measurements revealed the formation of a scaly surface structure, where the tips of these scales point directly towards the direction of the incident ion beam.

TRI3DYN as a powerful 3D-MC-BCA code allows to model nearly any surface structure including it's substructures. The results of the W-fuzz modelling are very promising. Some deviations to the experimental results are still observable, but the formation of a scaly structure after continuous erosion of W-fuzz can be reproduced and points out the capabilities of this modelling method [45].

As in a nuclear fusion device the contamination of the fusion plasma by high Z material is undesirable, due to increased radiative cooling of the plasma, the results showed in this chapter are good news [126]. Nanostructured W was feared to have a higher sputtering yield, which could increase the contamination, but the measurements showed here that the sputtering yield is tremendously lower, due to severe redeposition of sputtered material inside the fuzzy structure. Consequently, this should not be the case, although further investigations are necessary, since at elevated temperature the sputtering can be different, due to flattening/smoothing of the surface.

<div style="text-align: right;">*8*</div>

Results on the Erosion of Be films

The contents of the following chapter are in preparation of publishing.

In this chapter 8 the erosion of Be during Ar and D ion impact is presented (section 8.3) and the implantation behaviour of D investigated in detail. The sputtering behaviour as well as the implantation behaviour was compared to SDTrimSP-1D. This chapter also presents first results of the dual-mode QCM technique.
The Be experiments were performed at the FZJ, as the IAP at TU Wien is not equipped for this toxic material.

8.1 Preface

Be has advantageous properties such as low weight, high thermal and electrical conductivity, and has also the ability of neutron multiplication. It's low thermal expansion coefficient in combination with the low weight makes it an ideal mirror material for space telescopes, such as the James Webb Space Telescope [128].
It is also used in aviation and as an alloy with copper in the electronics industry. Since it is toxic to humans, especially as an aerosol, the applications in human environments are limited.
Be is also successfully used as PFM in the fusion experiment JET and is planned for ITER, currently being built in south of France [19]. As a low Z material the influence on the fusion plasma performance is low, as radiative cooling can only occur in the plasma edge (compare with chapter 1.2.2).
The armouring of the inner wall blankets, which face the plasma will be made of Be, but also test blankets will be utilized, where neutron multiplication will be

used to breed tritium (T) out of lithium (Li) [19, 129].

Implantation of the fusion fuel into the first wall and it's retention is a critical issue and under continuous investigation, especially as T is a radioactive material. The amount of T in the wall should therefore stay low, to minimize the radioactive contamination. For ITER an administrative safety limit of 700 g T in the whole Be blanket wall has been committed [33, 130]. Therefore, the retention and possible release mechanisms of the fusion fuel are investigated in detail.

In this chapter the retention mechanism of D in Be is investigated by using the QCM technique. Thin test films of Be were exposed to an Ar and D ion beam at room temperature. The possibility of in-situ analysis of the implantation measurements with the QCM technique in combination with the dual-mode temperature compensation technique (see chapter 4.1) during implantation and subsequent TDS allows measurements, which provide insight into the retention and release behaviour of Be.

8.2 Material and Methods

The basic setup of the experiment is largely identical as the setup shown in chapter 4.1. The main difference was the use of a Prevac IS40 sputter ion source, provided by the FZJ. Apart from that it is identical to the classic configuration of the QCM (see chapter 4, section 4.1.3 for details). This ion source delivers an ion flux of $\Phi \approx 10^{17}\,\mathrm{m^{-2}s^{-1}}$ without the use of a Wien-filter.

To evaluate the outgassing elements during TDS measurements a quadrupole residual gas analyser (RGA) of type Pfeiffer QMG-700 was used.

As samples Be coated quartz crystals were used. These coatings were fabricated by using a TVA technique at the National Institute of Laser, Plasma and Radiation Physics in Bucharest [131]. 500 nm thick Be films were deposited on top of an electrode of the quartz crystals.

In figure 8.1 the elemental composition of an unirradiated sample can be seen, where the TOF-ERDA technique was used (see chapter 4, section 4.2.2.3 for technique details). At the surface an oxide layer could be observed, where an O amount of 10% was measured. After a depth of only 20 nm the O amount drops to $2 - 3\%$, which stays constant throughout the bulk material. The high sensitivity to low Z materials of the TOF-ERDA technique allow also to determine the amount of H in the material, which was throughout below 1%. In general a high purity of Be samples can be seen.
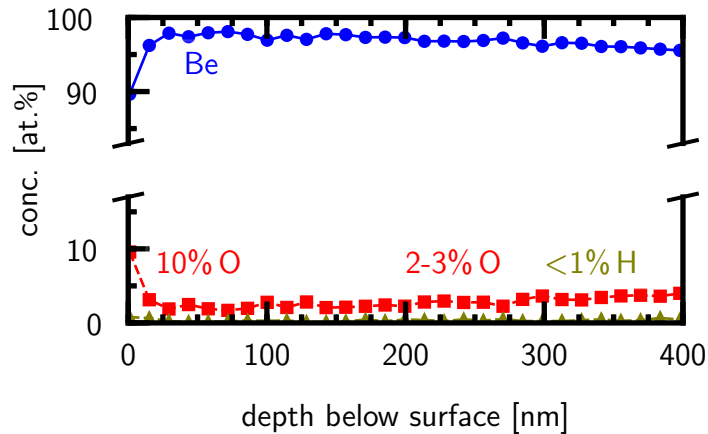
Figure 8.1 – Elemental depth profiles of a virgin Be sample as determined by TOF-ERDA, up to a depth of 400 nm. The measurement show a high concentration (conc.) of Be. At the surface O was found, up to 10 at.%, where in the bulk only $2 - 3$ at.% of O can be seen. H was detected throughout the sample with an amount of less than 1 at.%.

8.3 Ar and D Irradiation of Be

As a pre step to the implantation measurements, Ar irradiation of the Be samples was performed, in order to clean the sample surface from oxides. This allowed to evaluate sputtering yields of Ar on Be.

In figure 8.2 the measured absolute sputtering yields of Ar on Be and D on Be are presented and compared to literature data.

The left image shows the results using Ar as projectile at different energies and under normal incidence. A continuous erosion measurement was carried out with the QCM techniqe and the value was determined as soon as equilibrium conditions were reached. While literature data is mainly available below 1 keV the measured Ar sputtering yields complete the picture up to 5 keV. The agreement with the results of a static erosion modelling with SDTrimSP-1D is also very good.

The right image shows the results using D as projectile at a kinetic energy of 1.25 keV and 2.5 keV, as well as literature data and static erosion modelling with SDTrimSP-1D. One can clearly see fluctuations of the measurement results and also deviations from the result of the static modelling. The difficulty is that here significant implantation of the projectile in Be occurs and only after a certain saturation fluence it is possible to evaluate absolute sputtering yields. This behaviour will be investigated in more detail in the next section 8.4.
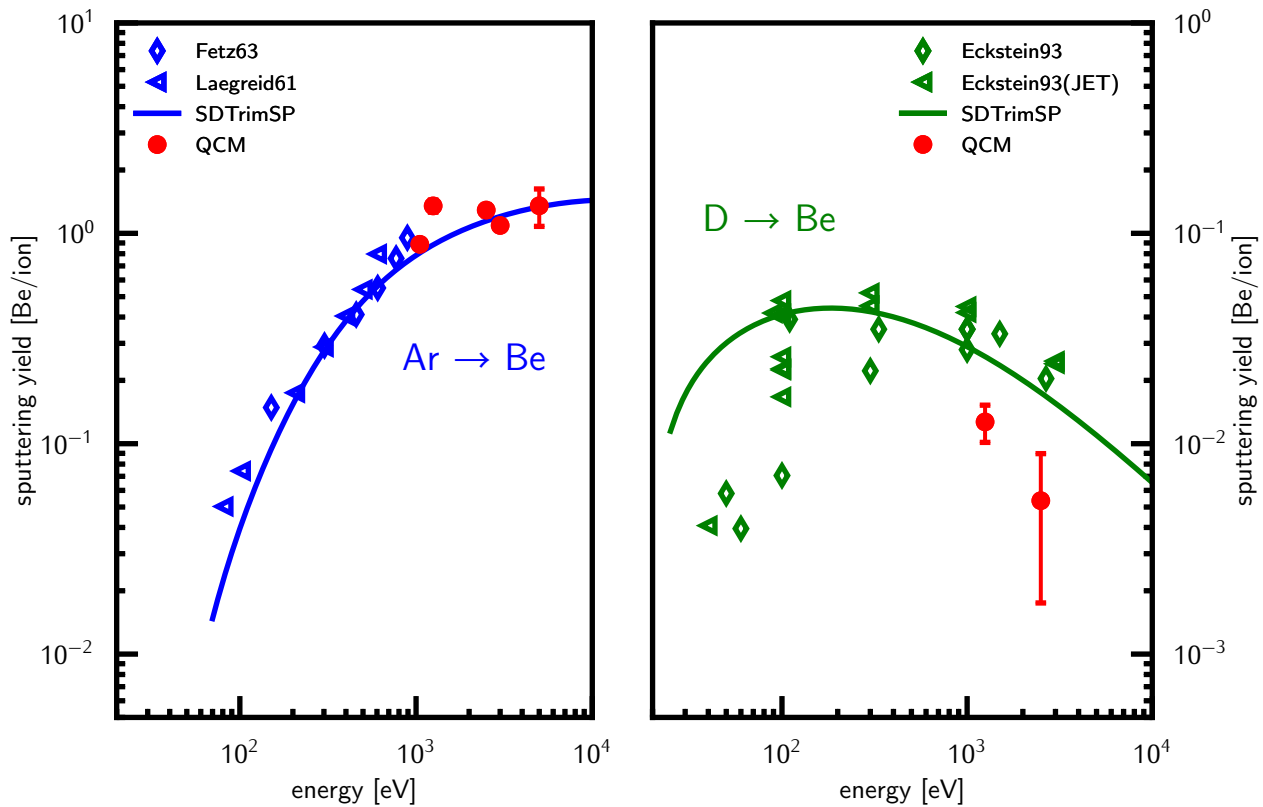
Figure 8.2 – Energy dependence of the sputtering yield of Be at Ar (blue/left) and D (green/right) irradiation under normal incidence and comparison to literature data as well as to static simulations with SDTrimSP-1D (solid lines) [48,109,111]. The red circles highlight the results evaluated with the classic QCM technique during this thesis. Note the different scaling of the ordinates.

8.4 D Implantation in Be

After a surface cleaning procedure by Ar ion impact, implantation measurements of D in Be were conducted. Implantation measurements were done with 2 different energies, but only one energy is now considered in full detail, as the behaviour is very similar. Since the sputter ion source delivers the highest ion current by using the D_2 molecule, this projectile was also used for implantation, where the kinetic energy of $5\,keV$ per D_2 is equivalent to $2.5\,keV$ per D. An average ion flux of $\Phi = (7.9 \pm 0.5) \times 10^{17}\,m^{-2}s^{-1}$ could be reached.

In figure 8.3 the results of the implantation measurement of D in Be can be seen. Implantation was performed at room temperature and under normal incidence ion impact, up to a fluence of $(9.9 \pm 0.6) \times 10^{21}\,m^{-2}$.
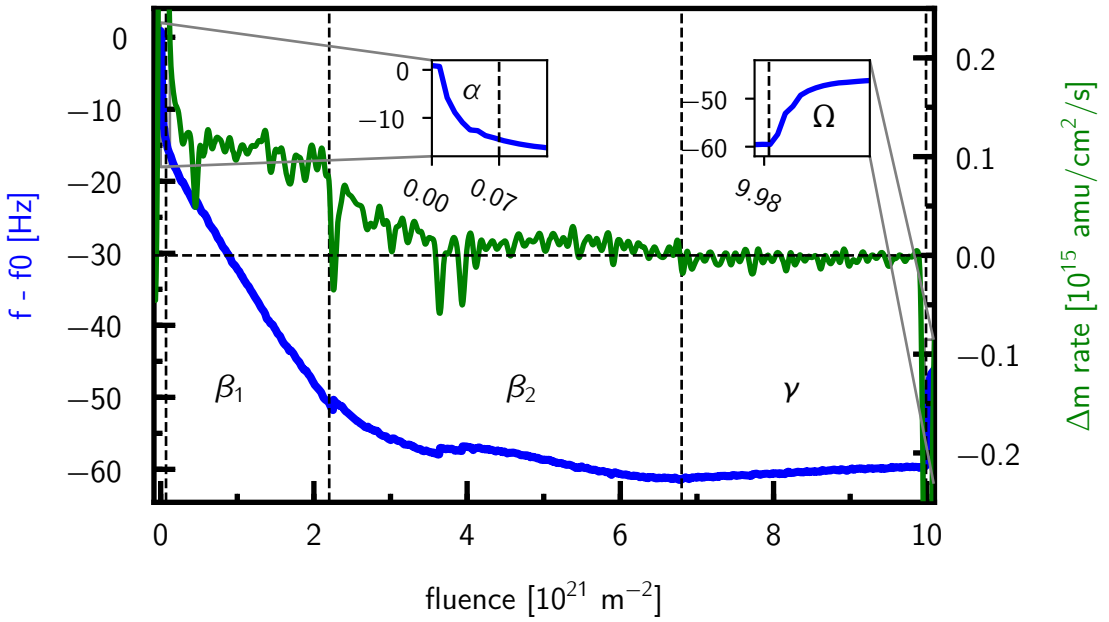
Figure 8.3 – Fluence dependence of the resonance frequency of the quartz crystal sample (blue) and the mass change rate (Δm rate) (green) of a Be sample under D irradiation with $2.5\,\text{keV}$ and normal incidence. Severe implantation of D can be seen as drop in the resonance frequency as well as a positive Δm rate (β_1 and β_2 region). Saturation of the sample occurs after a fluence of about $6.7 \times 10^{21}\,\text{m}^{-2}$, whereupon sputtering takes over as dominant process (γ region). The beam-on (α) and beam-off (Ω) regions are equivalent in height of about $12\,\text{Hz}$. Both insets have equivalent width and height for better comparison.

The QCM technique allows highly accurate mass change measurements, but only determination of the net mass change is possible. During ion bombardment of a sample, implantation as well as sputtering and outgassing occurs.

The implantation dominated regime can be seen as a drop in the resonance frequency of the crystal, which is equivalent to a positive mass change rate and therefore an increase of the sample mass. As soon as saturation occurs, Δm rate gets negative, meaning that sputtering overtakes as dominant process.

The implantation measurements show different regions, which can be interpreted as follows (compare with figure 8.3):

α - Switch-on region: Implantation of projectiles in easy accessible vacancies in combination with local stresses on the quartz crystal causing fast frequency changes. In the measurement a fast frequency drop of $12\,\text{Hz}$ can be seen and after a fluence of about $7 \times 10^{19}\,\text{m}^{-2}$ the linear implantation region starts.

β - Implantation region: Here, the quartz crystal is in stress equilibrium again and the implantation of projectiles continues, showing a positive and constant mass change rate of about $1.6 \times 10^{14}\,\text{amu/cm}^2/\text{s}$, as well as a continuous decrease of the resonance frequency. Easy accessible vacancies are filled up first, which can be seen in a high mass change rate (β_1 region). After a fluence of about $2.2 \times 10^{21}\,\text{m}^{-2}$ the mass change rate decreases, showing that easy accessible spots in the sample are nearly filled up and interstitial spots start getting filled (β_2 region).

γ - Sputtering region: After a fluence of $6.7 \times 10^{21}\,\text{m}^{-2}$ the sample is saturated and the mass change rate (Δm rate) becomes negative, meaning that sputtering overtakes as dominant process. By evaluating the slope of the frequency response in this region, the sputtering yield can be evaluated (see also chapter 4.1 for the detailed procedure).

Ω - Switch-off region: After a fluence of $9.9 \times 10^{21}\,\text{m}^{-2}$, the ion beam is switched off and projectiles implanted close to the surface are outgassing, causing a mass loss of the quartz. Also the sudden release of the local stress on the quartz crystal itself contributes to this response. Usually this region is the inverse of region α. It should be noted that after switching off the ion beam no more fluence is applied, but the abscissa was plotted further to allow a comparison with α.

The measured mass change rate also allows to determine the total mass change during this irradiation. Here a total mass increase of $\Delta m = 381 \times 10^{15}\,\text{amu/cm}^{-2}$ could be evaluated.

8.5 TDS Measurements

After the implantation measurement a thermal desorption spectroscopy (TDS) measurement was initiated. The included ohmic heating wires of the sample holder in combination with a computer controlled current supply and an attached thermocouple (compare with chapter 4.1.4) allows to perform a heating ramp with a slope of $1.5\,\mathrm{K/min}$. A quadrupole mass spectrometer (QMS) attached to the chamber, with a distance of about $10\,\mathrm{cm}$ of the sensor head to the sample, allowed to analyse the outgassing elements and molecules.

In figure 8.4 a TDS result can be seen, from room temperature to $500\,\mathrm{K}$. The QMS signal shows a pronounced $m/q = 4$ (D_2) peak, at a temperature of $423\,\mathrm{K}$, where in the $m/q = 2$ signal (H_2 and D) only a continuous decrease of the signal can be seen. The blue line in this signal shows the resulting mass change rate evaluated via the newly developed dual-mode QCM technique (compare with chapter 4.1.2). It confirms a negative mass change, peaking at $423\,\mathrm{K}$ and thus clearly shows the outgassing of D, which desorbs as D_2. By integrating the mass change rate over this peak, a total mass loss of $\Delta m = -394 \cdot 10^{15}\mathrm{amu/cm^2}$ could be evaluated.

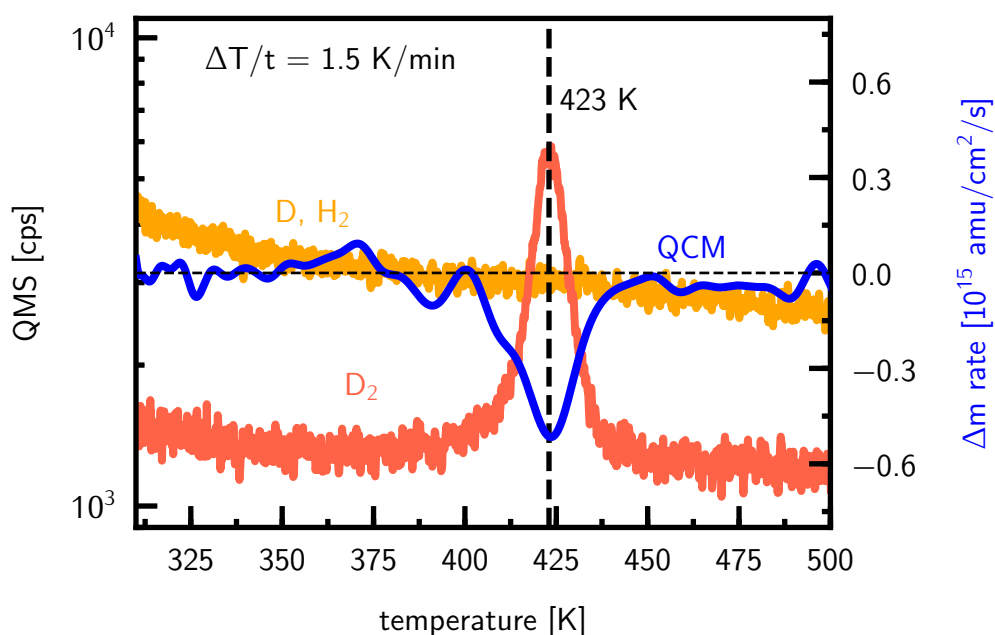

Figure 8.4 – TDS result after D implantation in Be. The quadrupole mass spectrometer revealed a pronounced D_2 outgassing, peaking at $423\,\mathrm{K}$ with a QMS count rate of 6×10^3 cps. The QCM confirms this peak, showing a negative peak of the mass change rate. By integrating over this peak, a total mass loss of $\Delta m = -394 \cdot 10^{15}\mathrm{amu/cm^2}$ can be evaluated.

In table 8.1 the mass change rates evaluated during implantation and during the TDS are compared and the relative to the total applied fluence evaluated. During implantation 19.2% of the total applied fluence was implanted into the sample, where during the TDS a value of 19.9% could be evaluated. Although an error of about 6% in the total applied fluence need to be considered here, it is interesting to see that as much mass change occurs through implantation as during TDS. This also shows that all the implanted D is released below $500\,\mathrm{K}$.

total applied fluence:	$9.9 \cdot 10^{21}\mathrm{D/m^2} = 1980 \cdot 10^{15}\mathrm{amu/cm^2}$	
Δm during implantation:	$+381 \cdot 10^{15}\mathrm{amu/cm^2}$	19.2%
Δm during TDS (at $m = 4$ peak):	$-394 \cdot 10^{15}\mathrm{amu/cm^2}$	19.9%

Table 8.1 – Comparison of the total applied fluence to the measured mass change rate (Δm) during implantation of D_2 on Be and subsequent TDS. The percentages refer to the total applied fluence. The mass loss measured with the QCM (using dual mode temperature compensation) during TDS is in good agreement with the mass increase during implantation. This shows that only about 20% of the total applied D is implanted and all implanted D is released during the TDS temperature scan (up to $500\,\mathrm{K}$).

8.5.1 Comparison to Modelling with SDTrimSP-1D

The software code SDTrimSP-1D allows to model dynamic erosion of a target, which can include material mixing, projectile implantation, as well as surface recession (see chapter 3 for more details).

To compare the implantation behaviour of D in Be with the QCM technique (figure 8.4) to modelling with SDTrimSP-1D the value of Δm rate need to be converted to the value of mass removal rate (mrr), which represents the mass change per incident particle. This can be easily done by simply including the incident ion current density (compare with chapter 4).

In figure 8.5 the fluence dependence of the mrr can be seen (blue). Equivalent to figure 8.3 a pronounced implantation behaviour is shown, up to a fluence of $2 \times 10^{21}\,\mathrm{m^{-2}}$. Henceforth the implantation decreases and after a fluence of $7 \times 10^{21}\,\mathrm{m^{-2}}$ the mrr becomes positive, which means that sputtering takes over as the dominant process.
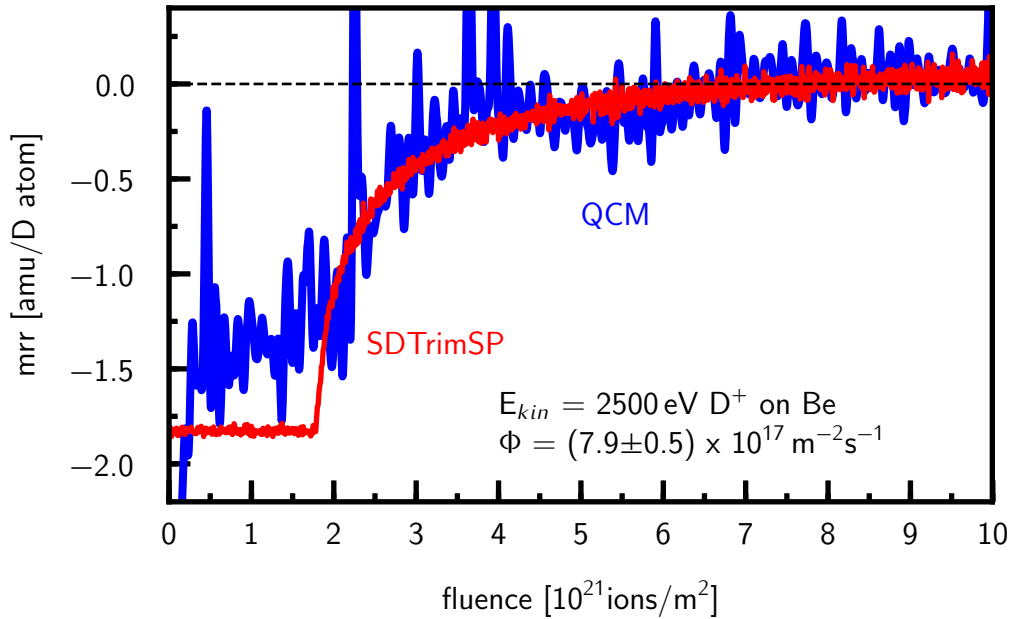
Figure 8.5 – Fluence dependence of the mass removal rate (mrr) of a Be sample under D irradiation with $2.5\,keV$ per D and normal incidence, using the QCM technique (blue). The negative mrr indicates pronounced implantation of D into Be, where after a fluence of around $2\times10^{21}\,m^{-2}$ saturation starts to appear. After a fluence of $6.7\times10^{21}\,m^{-2}$ the mrr becomes positive, meaning that sputtering takes over as dominant process. A good agreement with the code SDTrimSP-1D can be seen, by inlcuding a maximum D retention of $26\,at.\%$.

Figure 8.5 shows also a dynamic modelling result using SDTrimSP-1D (red). Here a pure Be target was assumed and simulated for irradiation with D projectiles of $2.5\,keV$ under normal incidence. Implantation of D in the Be target was considered and limited to $26\,at.\%$. If the implanted quantity exceeds this value the additional projectile is assumed to diffuse immediately to the surface and to desorb there. Deviations at low fluences are observable, but the saturation trend can be reproduced in acceptable agreement.

8.6 Summary and Conclusion

The interaction of energetic Ar and D ions with Be surfaces was investigated in this chapter, by using the newly developed dual-mode QCM technique. Ar irradiation was primarily performed to clean the sample surface from an oxide layer. After reaching a steady state erosion yield the absolute sputtering yield of Ar on Be

could be evaluated at energies from $1\,keV$ to $5\,keV$. The evaluated sputtering yields were compared to modelling with SDTrimSP. The rather simple modelling approach, by simulating a static and pure Be target already delivers good results and agrees well with the measured sputtering yields.

Subsequently implantation measurements with D in Be were investigated in more detail at $2.5\,keV$ per D and showed a pronounced fluence dependence. The possibility of in-situ mass change measurements with the QCM revealed valuable insight into the D saturation dynamics behaviour of a Be sample. It could be shown, that the implantation behaviour can be divided into 3 major-regimes: A nearly constant implantation mass change rate is observable in the initial-regime. After a fluence of $2.2 \times 10^{21}\,m^{-2}$ an transient region is observable, where the mass change rate decreases. Saturation of the sample occurs after a fluence of $6.7 \times 10^{21}\,m^{-2}$. From here sputtering becomes the dominant process.

By converting the measured mass change rate to a mass removal rate (mrr) a comparison with the erosion modelling code SDTrimSP-1D becomes possible. By performing a dynamic implantation modelling, allowing a maximum retention of D of $26\,\%$, good agreement with the measurements is found. This value agrees reasonable well with Oberkofler et. al. [35], where a slightly lower value of $20\,\%$ was found.

After D implantation of up to $9.9 \times 10^{21}\,m^{-2}$ TDS measurement were performed, with a heating ramp of $1.5\,K/min$, from room temperature to $500\,K$. The 'low-temperature' release peak of D could be seen very clearly, at a temperature of $423\,K$. It must be noted that the temperature was evaluated via a thermocouple mounted on the sample holder, as no direct connection to the quartz crystal sample is possible as it would disturb precise frequency measurements. Oberkofler et. al. [33] found out that a threshold fluence needs to be implanted first in order to see this 'low-temperature' release peak at all, whereon the maximum of this peak shifts to lower temperatures at higher fluences. Furthermore he found out that between $700\,K$ and $850\,K$ further D is released.

By using for the first time the new dual-mode temperature compensated QCM technique it could be shown that during the performed TDS up to $500\,K$ the same total mass change occurred as during implantation, which was found out to be about 20% of the total applied fluence. Therefore no further release of D is expected at higher temperatures. Unfortunately a temperature of $850\,K$ cannot be reached with the dual-mode QCM technique, as the quartz crystal does not survive such high temperatures.

As temperatures around $900\,K$ are expected for a Be blanket PFC in a fusion device the implantation of the fusion fuel into the wall should therefore be negligible small as it outgasses immediately [13, 129].

However, the retention mechanism in Be is still not completely understood and further experiments are necessary.

9

Conclusion and Outlook

The purpose of this work was to investigate the interaction of plasma facing materials (PFMs) under ion bombardment in the kinetic energy range of $0.25 - 5\,keV$. Depending on the angle of incidence, the composition of the ion and the sample material, reflection or implantation of the projectile occurs. In addition, surface erosion in form of physical sputtering takes place and changes the surface morphology, which can result in surface smoothening or roughening. Furthermore, the elemental composition of the surface in the form of preferential sputtering can also be changed considerably, which in turn influences the sputtering behaviour [42, 43, 101].

By using the highly sensitive TU Wien QCM the interaction of thin films of tungsten, iron, and beryllium as well as iron-tungsten mixed films under deuterium and argon irradiation was investigated [43]. Furthermore, the erosion of nanostructured tungsten (W-fuzz) under argon irradiation was investigated, using the QCM in catcher configuration. The high flexibility of this measurement method allows erosion investigations on a small scale under precise laboratory conditions without the need of a large tokamak fusion experiment.
The QCM measurements allow in situ investigations which, in combination with surface investigations using AFM and SEM, as well as elemental depth measurements via IBA or sputter-XPS, reveal the dynamic process of ion beam induced erosion with a high degree of detail.

These measurements make it possible to perform a comparison and benchmarking of erosion modelling with newly developed codes, which can take into account surface morphologies and even nanostructures.
In this work it could be shown that surface morphology sensitive MC-BCA codes, such as SDTrimSP-2D and TRI3DYN are capable to forecast the outcome of

experiments, if precise surface morphologies and elemental sample compositions are available.

Erosion measurements of Fe films under $500\,\text{eV}$ monoenergetic Ar irradiation at $60°$ angle of incidence showed a fluence dependent erosion rate, originating from a native oxide layer on top of the samples. After applying a fluence of $8 \times 10^{21}\,\text{m}^{-2}$ a clear decrease in the root mean square roughness R_q as well as in the width of the inclination distribution was observed, by performing pre and post AFM measurements. By using the code SDTrimSP-2D, where as surface input a random line surface was created with the same inclination distribution and R_q as the real sample, as well as the measured elemental depth distribution, the outcome of the QCM measurements could be reproduced. To be able to reproduce the actual surface pattern, the 2D approach is not sufficient and requires a full 3D code. Nevertheless the results are already remarkable, especially since the method of reducing a real 2D surface to a 1D line surface already led to a good agreement with the experimental results [44].

For the reconstruction of the FeW measurements the full 3D code TRI3DYN was used for the first time. The possibility to use a real AFM image as surface morphology input for the code, as well as the detailed elemental depth distribution evaluated via sputter-XPS and RBS allows a detailed comparison with the QCM experiments. The erosion due to prolonged D irradiation with $250\,\text{eV}$ up to a fluence of $4 \times 10^{23}\,\text{m}^{-2}$ under an angle of incidence of $0°$, $45°$ and $60°$ revealed a continuous reduction of the erosion yield due to surface enrichment of W, as well as an increase in the R_q [42]. The code TRI3DYN is able to confirm and reproduce the surface enrichment of W and the consequential reduction of the erosion rate. The comparison of the TRI3DYN results using different elemental depth measurements of sputter-XPS and RBS shows that very accurate data are essential to reproduce the experimental results. The resulting surface morphologies, especially under $0°$ and $45°$ angle of incidence are in good agreement with the experiments [43]. Under $60°$ angle of incidence the experiments revealed also a strong ripple formation, but TRI3DYN revealed a structure where the perpendicular mode ripple formation is more pronounced. The reason for this is not quite clear, but most probably the initial surface is of crucial importance here. The limited lateral extent of the surfaces that can be modelled is also an inaccuracy that is related to this deviation. Nevertheless, the comparison with TRI3DYN clearly shows that the surface morphology has an influence on the erosion behaviour even with low R_q roughnesses in the nm range [43].

TRI3DYN is also capable of modelling nanostructures, which allows a comparison to erosion measurement of W-fuzz. The QCM in catcher configuration was used to experimentally investigate the erosion of W-fuzz samples under prolonged Ar irradiation $2\,\text{keV}$ and under $60°$ angle of incidence. It was found that sputtered particles were emitted preferably in direction of the incident ion beam and that

nanostructures have only about 5% of the sputtering yield of bulk tungsten. After an applied fluence of $1.7 \times 10^{22}\,\mathrm{m}^{-2}$ a formation of scaly surface structures was observed via SEM, where the tips of these scales point directly towards the observer. For TRI3DYN erosion simulations, data was extracted from SEM images of real W-fuzz samples to randomly generate a nanostructured input model with identical areal coverage density and string thickness. This novel approach allows to create a fuzz model, whith that TRI3DYN is able to reproduce the dynamic formation of a scaly structure under prolonged Ar irradiation. The structure formation, due to severe redepostion of sputtered material and the clearly occurring backward sputtering could be reproduced. Nevertheless, deviations from the real experiments can still be seen, as the modelled total sputtering yield is overestimated and a too pronounced forward sputtering was modelled. The reason for this can certainly be the too rough model of the W-fuzz. By modelling additional porosity and a bigger volumes the agreement could likely be improved, but this goes beyond the capability of TRI3DYN so far. For fusion research the results are promising, as fuzz has a significantly lower sputtering yield than anticipated. However further experiments are necessary, since different behaviour may be seen, especially at elevated temperatures [45].

During the work also efforts were made to improve the TU Wien quartz crystal microbalance. A quasi simultaneous excitation of the ground mode (C1) and the third overtone mode (C3) of a quartz crystal allows to compensate for frequency changes caused by temperature changes of up to $700\,\mathrm{K}$. This technique was used for the first time to investigate the implantation and release behaviour of D in Be. A total D fluence of $9.9 \times 10^{21}\,\mathrm{m}^{-2}$ was applied, where the QCM mass change measurements during implantation showed that about 20% of the applied D fluence was implanted. A subsequent TDS measurement in combination with the new QCM dual-mode temperature compensation technique revealed a total mass change of also 20% of the total applied D fluence. Concluding it could be showed that the implanted D completely desorbed already below $500\,\mathrm{K}$. As higher temperatures are expected in a fusion device the retention of fusion fuel in a Be-PFM should be negligible small [13, 129]. The implantation behaviour was also modelled with the 1D version of SDTrimSP and the simulations could reproduce the experimentally observed behaviour well, if the D retention was limited to $26\,\mathrm{at}.\%$.

This work clearly showed the possibilities of the meanwhile nearly 40 years old MC-BCA code principle. The increasing computing power allows to continuously improve and extend the functionality, by taking into account dynamic changes and also surface morphologies [57, 69, 74]. Nevertheless the codes physical limits need always to be considered and makes the comparison to experimental results unavoidable. The TU Wien QCM technique in both classic and in the catcher configuration, is ideally suited for that.

Further measurements are ongoing, where a redesign of the QCM catcher manip-

ulator will be used. This upgrade allows to move the catcher in additional degrees of freedom and includes also a tilt axis, allowing to precisely align the surface of the catcher QCM to face the sample. This make it possible to measure the angular distribution of the sputtered particles with a higher degree of precision, as sensitivity effects due to distance and relative orientation changes can be avoided (refer to C. Cupak [132]).

Acronyms

AIC Analytical Instrumentation Center

ADC analog digital converter

AFM atomic force microscope

amu atomic mass unit

BCA binary collision approximation

CAD computer aided design

CCFE Culham Center for Fusion Energy

CF ConFlat

CM confocal microscope

CMS center of mass system

coax coaxial cable

DEMO DEMOnstration power station

ECR electron cyclotron resonance

ELM edge localized mode

ERDA elastic recoil detection analysis

FIB focused ion beam

FWHM full width half maximum

FZJ Forschungszentrum Jülich

GUI graphical user interface

HZDR Helmholtz Zentrum Dresden Rossendorf

IAP Institute of Applied Physics

IEA International Energy Agency

IPP Max Planck Institute of Plasma Physics

IBA ion beam analysis

ITER International Thermonuclear Experimental Reactor

JET Joint European Torus

KrC Krypton-Carbon

LS laboratory system

MC monte carlo

mrr mass removal rate

MD molecular dynamics

NBI neutral beam injection

PC personal computer

PFC plasma facing component

PFM plasma facing material

PVD physical vapour deposition

Python script based high level programming language www.python.org

QCM quartz crystal microbalance

QMS quadrupole mass spectrometer

RBS Rutherford backscattering spectroscopy

RGA residual gas analyser

RMSR root mean square roughness

SEM scanning electron microscopy

SRIM Stopping and Range of Ions in Matter

SDTrimSP Static and Dynamic TRIM Sequential and Parallel

STM scanning tunnelling microscope

toe tonnes of oil equivalent

TDS thermal desorption spectroscopy

TOF time of flight

TC thermocouple

TRIDYN Dynamic Transport of Ions in Matter

TRI3DYN TRIDYN in 3D

TRIM transport of ions in matter

tokamak Toroidal Chamber with Magnetic Coils (russian: ТОроидальная КА-мера с МАгнитными Катушками)

TVA thermionic vacuum arc

UHV ultra high vacuum

XPS X-ray photoelectron spectroscopy

ZBL Ziegler–Biersack–Littmark

Danksagung

Da es am Ende einer Doktorarbeit üblich ist noch ein paar Dankesworte an alle zu richten die mir dabei geholfen haben soweit zu kommen, möchte ich dieser Tradition ebenso beiwohnen. Zuvor möchte ich hier aber noch die zeitliche Entwicklung dieser Doktorarbeit zeigen, welche in der Abbildung 9.1 zu sehen ist. Ein kleines Python-Programm zur Datensicherung analysierte auch automatisch die wachsende PDF Datei der Dissertation. Insgesamt dauerte das Schreiben ca. viereinhalb Monate auch wenn manche Plateaus zu sehen sind, die entweder auf Feiertage oder Paperverbesserungsarbeiten zurückzuführen sind, wobei sich dies auch immer wieder überschnitten hat.
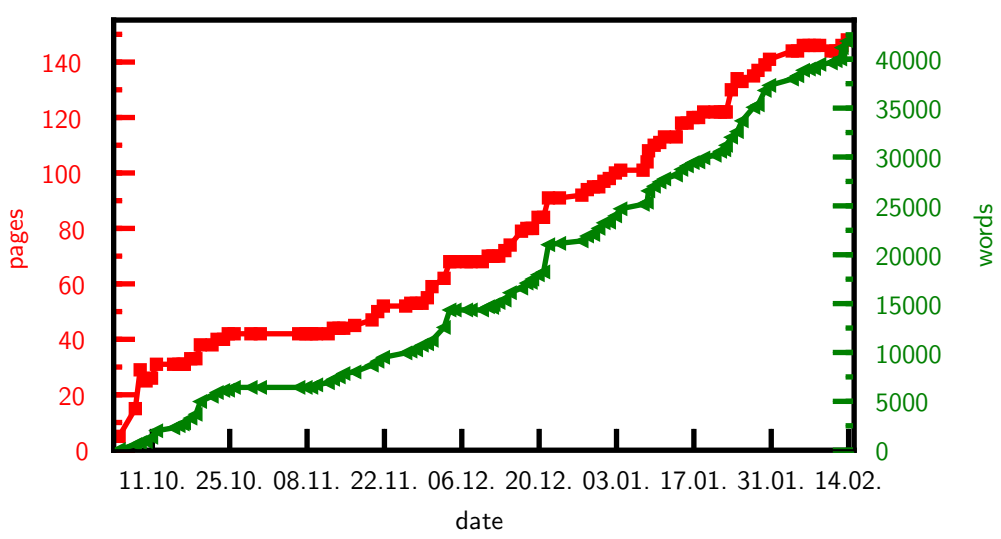

Abbildung 9.1 – Der dokumentierte Fortschritt der Dissertation.

109

Mit den folgenden letzten Zeilen möchte ich mich nun an all jene bedanken, die mir geholfen haben das Doktorrat durchzustehen und zu vollenden.

Als erstes bedanke ich mich bei Prof. Dr. Friedrich Aumayr: Lieber Fritz, vielen Dank für das Vertrauen, dass du mir entgegengebracht hast und auch die großartige Unterstützung. Du hattest immer ein offenes Ohr für mich und wertvolle Tipps, nicht nur für physikalische Probleme, sondern auch wie man nahender Überforderung entgegenwirkt. Es wird mir immer ein Vorbild sein mit welcher scheinbaren Leichtigkeit du Probleme angehst und löst. Danke auch, dass ich an 16 Konferenzen teilnehmen durfte, wobei die PSI in Princeton und in Rom besonders hervorzuheben sind, aber auch freue ich mich sehr, dass ich gleich zweimal auf die berühmte 3S Konferenz mitfahren durfte.

Ein großes Dankeschön gilt auch allen Mitgliedern der Arbeitsgruppe Atom- und Plasmaphysik. Insbesondere die QCM-ler Paul S., Daniel M., Herbert B. und Christian C. Ihr habt mir sehr viel bei den Experimenten und deren Auswertung geholfen sowie ihrer Interpretation. Ohne euch hätte ich es nicht geschafft!

Lieber Paul, du als längstjähriges Arbeitsgruppenmitglied und langjähriger Büro-Kollege verdienst besonderen Dank. Du hast mir bei vielen Problemen weitergeholfen, wobei auch immer wieder Zeit für Späße war. Deine ruhige Art sowie deine überlegte und ruhige Herangehensweise an Probleme finde ich immer wieder sehr beeindruckend.

Lieber Herbert, danke auch für deine Unterstützung und das fleißige 'Rumnerden'. Es hat Spaß gemacht mit dir über allerhand technische Probleme zu philosophieren, aber auch über Dinge in anderen Lebenslagen. Du bist eine großartige Bereicherung für das gesamte IAP.

Lieber Christian Cupacca, ein Danke auch an dich. Als wir uns bei deiner Bachelorarbeit 2017 kennengelernt haben ist mir bereits dein Ehrgeiz und Eifer aufgefallen und es freut mich umso mehr, dass du mein Nachfolger wirst. Alles Gute dabei!

Lieber Daniel, auch dir ein großes Dankeschön für deine äußerst präzise und detailverliebte Laborarbeit.

Des Weiteren möchte ich allen weiteren AG Mitgliedern danken, die weniger mit der QCM zu tun haben:

Liebe Janine S., gemeinsam haben wir am IAP sehr viel erlebt. Beide haben wir im Herbst 2014 begonnen und das wunderschöne fensterlose Augustin Labor lieben gelernt. Gemeinsam haben wir zweimal auf der 3S den Arlberg gerockt und auch auf der ISI Russland unsicher gemacht. Die vielen Unterhaltungen bei den Schokolade unterstützten Kaffeepausen mit dir habe ich sehr genossen, auch wenn ich hin und wieder nicht alles gehört habe was du gesagt hast. Du warst stets hilfsbereit und hast es auch geschafft mir Motivation zu geben. Vielen Dank für alles!

Lieber Richard W., deine reichhaltige Erfahrung in der Experimentalphysik war mir sehr oft nützlich, vielen Dank dafür! Unsere gemeinsamen Aufenthalte in Frankreich und Moskau waren kulinarische Höhepunkte, welche ich nie vergessen

werde! Ich bin froh und zuversichtlich, dass du die Arbeitsgruppe übernehmen wirst, auch wenn nun leider ich, als scheinbar einziger weiterer Star-Trek Fan, die Gruppe verlassen werde.

Lieber Georg H., auch dir ein Danke für die gemeinsame Doktoratszeit. Du warst zwar die meiste Zeit in Garching und oft nur als Hologramm oder per Skype anwesend, aber es war toll mit dir gemeinsam die Baustelle von ITER besucht zu haben.

Liebe Anna N., danke für deine immer sehr motivierenden Backwaren! Du bist eine großartige Bereicherung für die gesamte Arbeitsgruppe, insbesondere dein selbstloser Fleiß zum Wohle der Gruppe ist äußerst lobenswert.

Liebe Johanna F., liebe Lidija R. und lieber Gabriel S., auch euch ein Danke für die produktive und schöne gemeinsame Zeit.

Nicht nur den Arbeitsgruppen Mitgliedern gebührt Dank, sondern auch ganz besonderen Menschen:

Liebe Gabriela T., dir muss ich ganz besonders danken! Du hast mir in den letzten 1.5 Jahren, seit dem wir uns kennen, sehr viel Kraft und Liebe gegeben. Du hast mir gezeigt, dass mehr in mir steckt als das ich selbst gesehen habe und standest mir auch in schweren Stunden zur Seite. Deine wundervolle lebensfrohe Art und gewisse Dinge einfach etwas anders zu sehen hat mir sehr geholfen Ablenkung zu finden und Energie zu tanken! Dankeschön ♡!

Ein großes Danke auch an die Bootcamp KollegInnen, insbesondere an den Trainer Günther F. Die wöchentlichen USI Trainingsstunden um 7:00 früh, draußen und bei jedem Wetter waren eine Wohltat für meinen Geist und halfen mir mich besser konzentrieren zu können, auch wenn der Muskelkater danach oft lange und laut geschnurrt hat.

Liebe Maria S., auch wenn du deinen Lebensmittelpunkt im 9600 km entfernten Tucson gewählt hast, muss ich dir danken. Du hast mir während des Studiums sehr viel Unterstützung zukommen lassen und hattest auch während meines Doktorats immer ein offenes Ohr für meine Probleme, insbesondere wenn ich mal wieder meiner Grenze zur Überforderung nahe kam. Dankeschön und alles Gute in dem Land der unbegrenzten Möglichkeiten!

Zum Abschluss möchte ich mich noch bei meinen Eltern Elfriede und Fritz bedanken. Ihr habt mich immer unterstützt egal was ich gemacht habe. Es tut mir leid, dass ich nicht diese Leidenschaft für land- und forstwirtschaftliche Arbeiten aufweise die ihr habt, aber ich hoffe, dass ihr trotzdem zufrieden mit mir seid. Danke für die großartige Unterstützung!

Reinhard Stadlmayr

Wien, Österreich, Februar 2020

Bibliography

[1] IEA, 'world energy balances', Report (2019), URL `http://www.iea.org/statistics`

[2] Etheridge D.M., Steele L.P., Langenfelds R.L., Francey R.J., Barnola J.M. and Morgan V.I., 'Natural and anthropogenic changes in atmospheric CO2 over the last 1000 years from air in Antarctic ice and firn', *Journal of Geophysical Research: Atmospheres*, 101, 4115 (1996), URL `https://doi.org/10.1029/95JD03410`

[3] 'NASA', (2019), URL `https://climate.nasa.gov/`

[4] Lenssen N.J.L., Schmidt G.A., Hansen J.E., Menne M.J., Persin A., Ruedy R. and Zyss D., 'Improvements in the GISTEMP Uncertainty Model', *Journal of Geophysical Research: Atmospheres*, 124, 6307 (2019), URL `https://doi.org/10.1029/2018JD029522`

[5] Heard B.P., Brook B.W., Wigley T.M.L. and Bradshaw C.J.A., 'Burden of proof: A comprehensive review of the feasibility of 100renewable-electricity systems', *Renewable and Sustainable Energy Reviews*, 76, 1122 (2017), URL `http://www.sciencedirect.com/science/article/pii/S1364032117304495`

[6] Aust N., *Zur Problematik der Energiewende*, Skeptiker 3 (2019), URL `https://www.gwup.org/images/stories/skeptiker/sonstiges/Begleitmaterial_Skeptiker.pdf`

[7] IAEA, 'Measurement of Radionuclides in Food and the Environment', Report, international atomic energy agency (1989), URL `https://www.iaea.org/publications/1398/measurement-of-radionuclides-in-food-and-the-environment`

[8] Friedman F.D. and Friedman F., 'The Underground Relief Panels of King Djoser at the Step Pyramid Complex', *Journal of the American Research*

Center in Egypt, 32, 1 (1995), URL `https://www.doi.org/10.2307/40000828`

[9] 'Uranium 2018 Resources, Production and Demand ('Red Book')', Report, OECD-NEA and IAEA (2018), URL `http://www.oecd-nea.org/ndd/pubs/2018/7413-uranium-2018.pdf`

[10] Weizsäcker C.F.v., 'Zur Theorie der Kernmassen', *Zeitschrift für Physik*, 96, 431 (1935), URL `https://doi.org/10.1007/BF01337700`

[11] Einstein A., 'Zur Elektrodynamik bewegter Körper', *Annalen der Physik*, 322, 891 (1905), URL `https://doi.org/10.1002/andp.19053221004`

[12] Einstein A., 'Ist die Trägheit eines Körpers von seinem Energieinhalt abhängig?' *Annalen der Physik*, 323, 639 (1905), URL `https://doi.org/10.1002/andp.19053231314`

[13] Kikuchi M. and Lackner K., *Fusion Physics*, IAEA, International Atomic Energy Agency (IAEA) (2012), URL `http://www-pub.iaea.org/MTCD/Publications/PDF/Pub1562_web.pdf`

[14] Lawson J.D., 'Some Criteria for a Power Producing Thermonuclear Reactor', *Proceedings of the Physical Society. Section B*, 70, 6 (1957), URL `https://doi.org/10.1088/0370-1301/70/1/303`

[15] Bosch H.S. and Hale G.M., 'Improved formulas for fusion cross-sections and thermal reactivities', *Nuclear Fusion*, 32, 611 (1992), URL `https://www.doi.org/10.1088/0029-5515/32/4/i07`

[16] Cook I., Marbach G., Di Pace L., Girard C., Rocco P. and Taylor N.P., 'Results, conclusions, and implications of the SEAFP-2 programme', *Fusion Engineering and Design*, 51-52, 409 (2000), URL `https://doi.org/10.1016/S0920-3796(00)00271-4`

[17] Li S., Jiang H., Ren Z. and Xu C., 'Optimal Tracking for a Divergent-Type Parabolic PDE System in Current Profile Control', *Abstract and Applied Analysis*, 2014, 8 (2014), URL `http://dx.doi.org/10.1155/2014/940965`

[18] 'EUROfusion', (2020), URL `www.euro-fusion.org`

[19] 'ITER Organisation', (2020), URL `https://www.iter.org/`

[20] Pedersen T.S., Otte M., Lazerson S., Helander P., Bozhenkov S., Biedermann C., Klinger T., Wolf R.C., Bosch H.S. and Wendelstein X.T., 'Confirmation of the topology of the Wendelstein 7-X magnetic field to better than 1:100,000', *Nat Commun*, 7, 13493 (2016), URL `https://www.doi.org/10.1038/ncomms13493`

[21] Jacquinot J. and team t.J.E.T., 'Deuterium-tritium operation in magnetic confinement experiments: results and underlying physics', *Plasma Physics and Controlled Fusion*, 41, A13 (1999), URL `http://dx.doi.org/10.1088/0741-3335/41/3A/002`

[22] Pitts R.A., Kukushkin A., Loarte A., Martin A., Merola M., Kessel C.E., Komarov V. and Shimada M., 'Status and physics basis of the ITER divertor', *Physica Scripta*, T138, 014001 (2009), URL `http://dx.doi.org/10.1088/0031-8949/2009/T138/014001`

[23] Pitts R.A., Carpentier S., Escourbiac F., Hirai T., Komarov V., Kukushkin A.S., Lisgo S., Loarte A., Merola M., Mitteau R., Raffray A.R., Shimada M. and Stangeby P.C., 'Physics basis and design of the ITER plasma-facing components', *Journal of Nuclear Materials*, 415, S957 (2011), URL `https://doi.org/10.1016/j.jnucmat.2011.01.114`

[24] Merola M., Escourbiac F., Raffray A.R., Chappuis P., Hirai T. and Gicquel S., 'Engineering challenges and development of the ITER Blanket System and Divertor', *Fusion Engineering and Design*, 96-97, 34 (2015), URL `https://www.doi.org/10.1016/j.fusengdes.2015.06.045`

[25] Janeschitz G., 'Plasma–wall interaction issues in ITER', *Journal of Nuclear Materials*, 290-293, 1 (2001), URL `http://www.sciencedirect.com/science/article/pii/S0022311500006231`

[26] Dux R., Bobkov V., Herrmann A., Janzer A., Kallenbach A., Neu R., Mayer M., Müller H.W., Pugno R., Pütterich T., Rohde V. and Sips A.C.C., 'Plasma-wall interaction and plasma behaviour in the non-boronised all tungsten ASDEX Upgrade', *Journal of Nuclear Materials*, 390-391, 858 (2009), URL `https://www.doi.org/10.1016/j.jnucmat.2009.01.225`

[27] Zohm H., 'Edge localized modes (ELMs)', *Plasma Physics and Controlled Fusion*, 38, 105 (1996), URL `http://dx.doi.org/10.1088/0741-3335/38/2/001`

[28] Lang P.T., Loarte A., Saibene G., Baylor L.R., Becoulet M., Cavinato M., Clement-Lorenzo S., Daly E., Evans T.E., Fenstermacher M.E., Gribov Y.,

Horton L.D., Lowry C., Martin Y., Neubauer O., Oyama N., Schaffer M.J., Stork D., Suttrop W., Thomas P., Tran M., Wilson H.R., Kavin A. and Schmitz O., 'ELM control strategies and tools: status and potential for ITER', *Nuclear Fusion*, 53, 043004 (2013), URL `http://dx.doi.org/10.1088/0029-5515/53/4/043004`

[29] Fortuna-Zaleśna E., Grzonka J., Moon S., Rubel M., Petersson P. and Widdowson A., 'Fine metal dust particles on the wall probes from JET-ILW', *Physica Scripta*, T170, 014038 (2017), URL `http://dx.doi.org/10.1088/1402-4896/aa8ddf`

[30] Kallenbach A., Balden M., Dux R., Eich T., Giroud C., Huber A., Maddison G.P., Mayer M., McCormick K., Neu R., Petrie T.W., Pütterich T., Rapp J., Reinke M.L., Schmid K., Schweinzer J. and Wolfe S., 'Plasma surface interactions in impurity seeded plasmas', *Journal of Nuclear Materials*, 415, S19 (2011), URL `https://www.doi.org/10.1016/j.jnucmat.2010.11.105`

[31] Kallenbach A., Dux R., Fuchs J.C., Fischer R., Geiger B., Giannone L., Herrmann A., Lunt T., Mertens V., McDermott R., Neu R., Pütterich T., Rathgeber S., Rohde V., Schmid K., Schweinzer J. and Treutterer W., 'Divertor power load feedback with nitrogen seeding in ASDEX Upgrade', *Plasma Physics and Controlled Fusion*, 52, 055002 (2010), URL `https://www.doi.org/10.1088/0741-3335/52/5/055002`

[32] Kallenbach A., Bernert M., Eich T., Fuchs J.C., Giannone L., Herrmann A., Schweinzer J. and Treutterer W., 'Optimized tokamak power exhaust with double radiative feedback in ASDEX Upgrade', *Nuclear Fusion*, 52, 122003 (2012), URL `https://www.doi.org/10.1088/0029-5515/52/12/122003`

[33] Oberkofler M., Reinelt M., Allouche A., Lindig S. and Linsmeier C., 'Towards a detailed understanding of the mechanisms of hydrogen retention in beryllium', *Physica Scripta*, T138, 014036 (2009), URL `https://www.doi.org/10.1088/0031-8949/2009/t138/014036`

[34] Oberkofler M. and Linsmeier C., 'Deuterium release from implanted beryllium and beryllium oxide', *Journal of Nuclear Materials*, 415, S724 (2011), URL `https://www.doi.org/10.1016/j.jnucmat.2010.11.015`

[35] Oberkofler M., Reinelt M. and Linsmeier C., 'Retention and release mechanisms of deuterium implanted into beryllium', *Nuclear Instruments and Methods in Physics Research Section B: Beam Interactions with Materials*

and Atoms, 269, 1266 (2011), URL `https://www.doi.org/10.1016/j.nimb.2010.11.058`

[36] Ogorodnikova O.V., Roth J. and Mayer M., 'Ion-driven deuterium retention in tungsten', *Journal of Applied Physics*, 103, 034902 (2008), URL `https://www.doi.org/10.1063/1.2828139`

[37] Dobes K., Köppen M., Oberkofler M., Lungu C.P., Porosnicu C., Höschen T., Meisl G., Linsmeier C. and Aumayr F., 'Interaction of nitrogen ions with beryllium surfaces', *Nuclear Instruments and Methods in Physics Research Section B: Beam Interactions with Materials and Atoms*, 340, 34 (2014), URL `https://www.doi.org/10.1016/j.nimb.2014.06.025`

[38] Brezinsek S., Coenen J.W., Schwarz-Selinger T., Schmid K., Kirschner A., Hakola A., Tabares F.L., Meiden H.J.v.d., Mayoral M.L., Reinhart M., Tsitrone E., Ahlgren T., Aints M., Airila M., Almaviva S., Alves E., Angot T., Anita V., Parra R.A., Aumayr F., Balden M., Bauer J., Yaala M.B., Berger B.M., Bisson R., Björkas C., Radovic I.B., Borodin D., Bucalossi J., Butikova J., Butoi B., Čadež I., Caniello R., Caneve L., Cartry G., Catarino N., Čekada M., Ciraolo G., Ciupinski L., Colao F., Corre Y., Costin C., Craciunescu T., Cremona A., Angeli M.D., Castro A.d., Dejarnac R., Dellasega D., Dinca P., Dittmar T., Dobrea C., Hansen P., Drenik A., Eich T., Elgeti S., Falie D., Fedorczak N., Ferro Y., Fornal T., Fortuna-Zalesna E., Gao L., Gasior P., Gherendi M., Ghezzi F., Ž G., Greuner H., Grigore E., Grisolia C., Groth M., Gruca M., Grzonka J., Gunn J.P., Hassouni K., Heinola K., Höschen T., Huber S., Jacob W., Jepu I., Jiang X., Jogi I., Kaiser A., Karhunen J., Kelemen M., Köppen M., Koslowski H.R., Kreter A., Kubkowska M., Laan M., Laguardia L., Lahtinen A., Lasa A., Lazic V., Lemahieu N., Likonen J., Linke J., Litnovsky A., Ch L., Loewenhoff T., Lungu C., Lungu M. *et al.*, 'Plasma–wall interaction studies within the EUROfusion consortium: progress on plasma-facing components development and qualification', *Nuclear Fusion*, 57, 116041 (2017), URL `https://www.doi.org/10.1088/1741-4326/aa796e`

[39] Jung P., 'Diffusion and retention of implanted helium in beryllium', *Journal of Nuclear Materials*, 202, 210 (1993), URL `https://www.doi.org/10.1016/0022-3115(93)90389-g`

[40] Maisonnier D., Cook I., Pierre S., Lorenzo B., Edgar B., Karin B., Luigi D.P., Robin F., Luciano G., Stephan H., Claudio N., Prachai N., Aldo P., Neill T. and David W., 'The European power plant conceptual study', *Fusion Engineering and Design*, 75-79, 1173 (2005), URL `https://www.doi.org/10.1016/j.fusengdes.2005.06.095`

[41] Bolt H., Barabash V., Federici G., Linke J., Loarte A., Roth J. and Sato K., 'Plasma facing and high heat flux materials – needs for ITER and beyond', *Journal of Nuclear Materials*, 307-311, 43 (2002), URL `https://www.doi.org/10.1016/s0022-3115(02)01175-3`

[42] Berger B.M., Stadlmayr R., Blöch D., Gruber E., Sugiyama K., Schwarz-Selinger T. and Aumayr F., 'Erosion of Fe-W model system under normal and oblige D ion irradiation', *Nuclear Materials and Energy*, 12, 468 (2017), URL `https://www.doi.org/10.1016/j.nme.2017.03.030`

[43] Stadlmayr R., Szabo P.S., Mayer D., Cupak C., Möller W. and Aumayr F., 'Erosion of iron-tungsten model films by deuterium ion irradiation: a benchmark for TRI3DYN', *Physica Scripta*, T180, in print (2020), URL `https://www.doi.org/10.1088/1402-4896/ab438f`

[44] Stadlmayr R., Szabo P.S., Berger B.M., Cupak C., Chiba R., Blöch D., Mayer D., Stechauner B., Sauer M., Foelske-Schmitz A., Oberkofler M., Schwarz-Selinger T., Mutzke A. and Aumayr F., 'Fluence dependent changes of surface morphology and sputtering yield of iron: Comparison of experiments with SDTrimSP-2D', *Nuclear Instruments and Methods in Physics Research Section B: Beam Interactions with Materials and Atoms*, 430, 42 (2018), URL `https://www.doi.org/10.1016/j.nimb.2018.06.004`

[45] Stadlmayr R., Szabo P.S., Cupak C., Mayer D., Dittmar T., Bischoff L., Möller S., Rasinski M., Wilhelm R.A., Möller W. and Aumayr F., 'Sputtering of Nanostructured Tungsten and Comparison to Modelling with TRI3DYN', *Journal of Nuclear Materials*, 532 (2020), URL `https://www.doi.org/10.1016/j.jnucmat.2020.152019`

[46] Eckstein W., *The Binary Collision Model*, book section Chapter 2, 4–32, Springer Series in Materials Science, Springer Berlin Heidelberg, Berlin, Heidelberg (1991), URL `http://dx.doi.org/10.1007/978-3-642-73513-4_2`

[47] Grün E., Horanyi M. and Sternovsky Z., 'The lunar dust environment', *Planetary and Space Science*, 59, 1672 (2011), URL `https://www.doi.org/10.1016/j.pss.2011.04.005`

[48] Behrisch R. and Eckstein W., *Sputtering by Particle Bombardment*, volume 110 of *Topics in Applied Physics*, Springer Berlin Heidelberg (2007), URL `https://www.doi.org/10.1007/978-3-540-44502-9`

[49] Langley R.A., Bohdansky J., Eckstein W., Mioduszewski P., Roth J., Taglauer E., Thomas E.W., Verbeek H. and Wilson K.L., 'Data Compendium for Plasma-Surface Interactions', *Nuclear Fusion*, 24, S9 (1984), URL `http://dx.doi.org/10.1088/0029-5515/24/S1/001`

[50] Ballauf L., Hechenberger F., Stadlmayr R., Dittmar T., Daxner M., Zöttl S., Aumayr F., Herman Z. and Scheier P., 'Formation of beryllium-hydrogen ions in chemical sputtering from 20 to 420eV', *Nuclear Materials and Energy*, 22, 100722 (2020), URL `https://doi.org/10.1016/j.nme.2019.100722`

[51] Aumayr F. and Winter H., 'Potential sputtering', *Philos Trans A Math Phys Eng Sci*, 362, 77 (2004), URL `https://www.doi.org/10.1098/rsta.2003.1300`

[52] Hayderer G., Schmid M., Varga P., Winter H.P., Aumayr F., Wirtz L., Lemell C., Burgdörfer J., Hägg L. and Reinhold C.O., 'Threshold for Potential Sputtering of LiF', *Physical Review Letters*, 83, 3948 (1999), URL `https://www.doi.org/10.1103/PhysRevLett.83.3948`

[53] Gruber E., Wilhelm R.A., Petuya R., Smejkal V., Kozubek R., Hierzenberger A., Bayer B.C., Aldazabal I., Kazansky A.K., Libisch F., Krasheninnikov A.V., Schleberger M., Facsko S., Borisov A.G., Arnau A. and Aumayr F., 'Ultrafast electronic response of graphene to a strong and localized electric field', *Nat Commun*, 7, 13948 (2016), URL `https://www.doi.org/10.1038/ncomms13948`

[54] Sigmund P., *Sputtering by ion bombardment theoretical concepts*, 9–71, Springer Berlin Heidelberg, Berlin, Heidelberg (1981), URL `https://doi.org/10.1007/3540105212_7`

[55] Möller W., 'Fundamentals of Ion-Solid Interaction - A Compact Introduction', Report, Helmholtz-Zentrum Dresden-Rossendorf (2017), URL `https://www.hzdr.de/publications/Publ-24296`

[56] Eckstein W., *Computer Simulation of Ion-Solid Interactions*, volume 10 of *Springer Series in Materials Science*, Springer, Berlin, Heidelberg (1991), URL `https://www.doi.org/10.1007/978-3-642-73513-4`

[57] Ziegler J.F., Ziegler M.D. and Biersack J.P., 'SRIM – The stopping and range of ions in matter (2010)', *Nuclear Instruments and Methods in Physics Research Section B: Beam Interactions with Materials and Atoms*, 268, 1818 (2010), URL `https://www.doi.org/10.1016/j.nimb.2010.02.091`

[58] Biersack J.P. and Haggmark L.G., 'A Monte Carlo computer program for the transport of energetic ions in amorphous targets', *Nuclear Instruments and Methods*, 174, 257 (1980), URL `https://doi.org/10.1016/0029-554X(80)90440-1`

[59] Wilson W.D., Haggmark L.G. and Biersack J.P., 'Calculations of nuclear stopping, ranges, and straggling in the low-energy region', *Physical Review B*, 15, 2458 (1977), URL `https://www.doi.org/10.1103/PhysRevB.15.2458`

[60] Mutzke A., Schneider R., Eckstein W. and Dohmen R., 'SDTrimSP Version 5.00', Report, Max-Planck-Institut für Plasmaphysik (2011), URL `http://hdl.handle.net/11858/00-001M-0000-0026-EAFA-8`

[61] Sigmund P., 'Theory of Sputtering. I. Sputtering Yield of Amorphous and Polycrystalline Targets', *Physical Review*, 184, 383 (1969), URL `https://www.doi.org/10.1103/PhysRev.184.383`

[62] Arredondo R., Oberkofler M., Schwarz-Selinger T., von Toussaint U., Burwitz V.V., Mutzke A., Vassallo E. and Pedroni M., 'Angle-dependent sputter yield measurements of keV D ions on W and Fe and comparison with SDTrimSP and SDTrimSP-3D', *Nuclear Materials and Energy*, 18, 72 (2019), URL `https://doi.org/10.1016/j.nme.2018.12.007`

[63] Küstner M., Eckstein W., Dose V. and Roth J., 'The influence of surface roughness on the angular dependence of the sputter yield', *Nuclear Instruments and Methods in Physics Research Section B: Beam Interactions with Materials and Atoms*, 145, 320 (1998), URL `https://www.doi.org/10.1016/s0168-583x(98)00399-1`

[64] Küstner M., Eckstein W., Hechtl E. and Roth J., 'Angular dependence of the sputtering yield of rough beryllium surfaces', *Journal of Nuclear Materials*, 265, 22 (1999), URL `<GotoISI>://WOS:000078356100003`

[65] Alder B.J. and Wainwright T.E., 'Studies in Molecular Dynamics. I. General Method', *The Journal of Chemical Physics*, 31, 459 (1959), URL `https://doi.org/10.1063/1.1730376`

[66] d'Ans J. and Lax E., *Taschenbuch für Chemiker und Physiker: Band 3: Elemente, anorganische Verbindungen und Materialien, Minerale*, volume 3, Springer-Verlag (2013), URL `https://www.doi.org/10.1007/978-3-642-58842-6`

[67] Biersack J.P. and Eckstein W., 'Sputtering studies with the Monte Carlo Program TRIM.SP', *Applied Physics A*, 34, 73 (1984), URL `https://doi.org/10.1007/BF00614759`

[68] Möller W., Eckstein W. and Biersack J.P., 'Tridyn-binary collision simulation of atomic collisions and dynamic composition changes in solids', *Computer Physics Communications*, 51, 355 (1988), URL `https://www.doi.org/10.1016/0010-4655(88)90148-8`

[69] Möller W. and Eckstein W., 'Tridyn — A TRIM simulation code including dynamic composition changes', *Nuclear Instruments and Methods in Physics Research Section B: Beam Interactions with Materials and Atoms*, 2, 814 (1984), URL `https://www.doi.org/10.1016/0168-583x(84)90321-5`

[70] Mutzke A., Schneider R., Eckstein W., Dohmen R., Schmid K., Toussaint U.v. and Badelow G., 'SDTrimSP Version 6.00', (2019), URL `https://www.doi.org/10.17617/2.3026474`

[71] Hofsäss H., Zhang K. and Mutzke A., 'Simulation of ion beam sputtering with SDTrimSP, TRIDYN and SRIM', *Applied Surface Science*, 310, 134 (2014), URL `https://www.doi.org/10.1016/j.apsusc.2014.03.152`

[72] Mutzke A., Schneider R. and Bandelow G., 'SDTrimSP-2D: Simulation of Particles Bombarding on a Two Dimensional Target-Version 2.0', Report, Max-Planck-Institut für Plasmaphysik (2013), URL `http://hdl.handle.net/11858/00-001M-0000-0026-E06F-E`

[73] Bizyukov I., Mutzke A., Schneider R. and Davis J., 'Evolution of the 2D surface structure of a silicon pitch grating under argon ion bombardment: Experiment and modeling', *Nuclear Instruments and Methods in Physics Research Section B: Beam Interactions with Materials and Atoms*, 268, 2631 (2010), URL `https://www.doi.org/10.1016/j.nimb.2010.06.035`

[74] Möller W., 'TRI3DYN – Collisional computer simulation of the dynamic evolution of 3-dimensional nanostructures under ion irradiation', *Nuclear Instruments and Methods in Physics Research Section B: Beam Interactions with Materials and Atoms*, 322, 23 (2014), URL `https://www.doi.org/10.1016/j.nimb.2013.12.027`

[75] von Toussaint U., Mutzke A. and Manhard A., 'Sputtering of rough surfaces: a 3D simulation study', *Physica Scripta*, T170, 014056 (2017), URL `https://www.doi.org/10.1088/1402-4896/aa90be`

[76] Sauerbrey G., 'Verwendung von Schwingquarzen zur Wägung dünner Schichten und zur Mikrowägung', *Zeitschrift für Physik*, 155, 206 (1959), URL https://www.doi.org/10.1007/bf01337937

[77] Benes E., Gröschl M., Burger W. and Schmid M., 'Sensors based on piezoelectric resonators', *Sensors and Actuators A: Physical*, 48, 1 (1995), URL https://www.doi.org/10.1016/0924-4247(95)00846-2

[78] Schmid M., 'Möglichkeiten und Grenzen der Schwingquarz-Schichtdickenmessung', Dissertation (1989), URL http://katalog.ub.tuwien.ac.at/AC00067936

[79] Hayderer G., Schmid M., Varga P., Winter H.P. and Aumayr F., 'A highly sensitive quartz-crystal microbalance for sputtering investigations in slow ion–surface collisions', *Review of Scientific Instruments*, 70, 3696 (1999), URL https://www.doi.org/10.1063/1.1149979

[80] Pierce D.E., Kim Y. and Vig J.R., 'A temperature insensitive quartz microbalance', *IEEE Trans Ultrason Ferroelectr Freq Control*, 45, 1238 (1998), URL https://www.doi.org/10.1109/58.726449

[81] Azcondo F.J. and Peire J., 'Quartz crystal oscillator used as temperature sensor', in *Proceedings IECON '91: 1991 International Conference on Industrial Electronics, Control and Instrumentation*, 2580–2585 vol.3, URL https://www.doi.org/10.1109/IECON.1991.238941

[82] Besson R.J., Boy J.J., Glotin B., Jinzaki Y., Sinha B. and Valdois M., 'A dual-mode thickness-shear quartz pressure sensor', *IEEE Transactions on Ultrasonics, Ferroelectrics, and Frequency Control*, 40, 584 (1993), URL https://www.doi.org/10.1109/58.238112

[83] Golczewski A., Dobes K., Wachter G., Schmid M. and Aumayr F., 'A quartz-crystal-microbalance technique to investigate ion-induced erosion of fusion relevant surfaces', *Nuclear Instruments and Methods in Physics Research Section B: Beam Interactions with Materials and Atoms*, 267, 695 (2009), URL https://www.doi.org/10.1016/j.nimb.2008.10.088

[84] (2006), URL http://www.kvg-gmbh.de/

[85] Kelly P.J. and Arnell R.D., 'Magnetron sputtering: a review of recent developments and applications', *Vacuum*, 56, 159 (2000), URL https://doi.org/10.1016/S0042-207X(99)00189-X

[86] Reichelt K. and Jiang X., 'The preparation of thin films by physical vapour deposition methods', *Thin Solid Films*, 191, 91 (1990), URL `https://doi.org/10.1016/0040-6090(90)90277-K`

[87] Lungu C.P., Mustata I., Zaroschi V., Lungu A.M., Anghel A., Chiru P., Rubel M., Coad P. and Matthews G.F., 'Beryllium coatings on metals for marker tiles at JET: development of process and characterization of layers', *Physica Scripta*, T128, 157 (2007), URL `http://dx.doi.org/10.1088/0031-8949/2007/T128/030`

[88] Dobeš K., 'Erosion of fusion relevant surfaces under ion impact', Phd thesis (2014), URL `http://katalog.ub.tuwien.ac.at/AC11439843`

[89] Berger B.M., 'Laboratory work on plasma-wall-interaction processes relevant for fusion experiments', Phd thesis (2017), URL `http://katalog.ub.tuwien.ac.at/AC13695810`

[90] Berger B.M., Szabo P.S., Stadlmayr R. and Aumayr F., 'Sputtering measurements using a quartz crystal microbalance as a catcher', *Nuclear Instruments and Methods in Physics Research Section B: Beam Interactions with Materials and Atoms*, 406, 533 (2017), URL `https://www.doi.org/10.1016/j.nimb.2016.11.039`

[91] Stevens D.S. and Tiersten H.F., 'An analysis of doubly rotated quartz resonators utilizing essentially thickness modes with transverse variation', *The Journal of the Acoustical Society of America*, 79, 1811 (1986), URL `https://www.doi.org/10.1121/1.393190`

[92] McMullan D., 'Scanning electron microscopy 1928–1965', *Scanning*, 17, 175 (1995), URL `https://doi.org/10.1002/sca.4950170309`

[93] Schneider C.A., Rasband W.S. and Eliceiri K.W., 'NIH Image to ImageJ: 25 years of image analysis', *Nature Methods*, 9, 671 (2012), URL `https://doi.org/10.1038/nmeth.2089`

[94] Oura K., Katayama M., Zotov A.V., Lifshits V.G. and Saranin A.A., *Surface Analysis III. Probing Surfaces with Ions*, 109–143, Springer Berlin Heidelberg, Berlin, Heidelberg (2003), URL `https://doi.org/10.1007/978-3-662-05179-5_6`

[95] Rutherford E., 'LXXIX. The scattering of alpha and beta particles by matter and the structure of the atom', *The London, Edinburgh, and Dublin Philosophical Magazine and Journal of Science*, 21, 669 (1911), URL `https://doi.org/10.1080/14786440508637080`

[96] Mayer M., 'SIMNRA, a simulation program for the analysis of NRA, RBS and ERDA', *AIP Conference Proceedings*, 475, 541 (1999), URL `https://www.doi.org/10.1063/1.59188`

[97] L'Ecuyer J., Brassard C., Cardinal C., Chabbal J., Deschênes L., Labrie J.P., Terreault B., Martel J.G. and St. Jacques R., 'An accurate and sensitive method for the determination of the depth distribution of light elements in heavy materials', *Journal of Applied Physics*, 47, 381 (1976), URL `https://doi.org/10.1063/1.322288`

[98] Giangrandi S., Sajavaara T., Brijs B., Arstila K., Vantomme A. and Vandervorst W., 'Low-energy heavy-ion TOF-ERDA setup for quantitative depth profiling of thin films', *Nuclear Instruments and Methods in Physics Research Section B: Beam Interactions with Materials and Atoms*, 266, 5144 (2008), URL `https://www.doi.org/10.1016/j.nimb.2008.08.018`

[99] Zhang Y., Whitlow H.J., Winzell T., Bubb I.F., Sajavaara T., Arstila K. and Keinonen J., 'Detection efficiency of time-of-flight energy elastic recoil detection analysis systems', *Nuclear Instruments and Methods in Physics Research Section B: Beam Interactions with Materials and Atoms*, 149, 477 (1999), URL `https://doi.org/10.1016/S0168-583X(98)00963-X`

[100] Norajitra P., Bühler L., Fischer U., Gordeev S., Malang S. and Reimann G., 'Conceptual design of the dual-coolant blanket in the frame of the EU power plant conceptual study', *Fusion Engineering and Design*, 69, 669 (2003), URL `https://www.doi.org/10.1016/s0920-3796(03)00207-2`

[101] Sugiyama K., Roth J., Alimov V.K., Schmid K., Balden M., Elgeti S., Koch F., Höschen T., Baldwin M.J., Doerner R.P., Maier H. and Jacob W., 'Erosion study of Fe–W binary mixed layer prepared as model system for RAFM steel', *Journal of Nuclear Materials*, 463, 272 (2015), URL `https://www.doi.org/10.1016/j.jnucmat.2014.11.044`

[102] Mutzke A., Bizyukov I., Schneider R. and Davis J., 'Nano-scale modification of 2D surface structures exposed to 6keV carbon ions: Experiment and modeling', *Nuclear Instruments and Methods in Physics Research Section B: Beam Interactions with Materials and Atoms*, 269, 582 (2011), URL `https://www.doi.org/10.1016/j.nimb.2011.01.012`

[103] Golczewski A., Kuzucan A., Schmid K., Roth J., Schmid M. and Aumayr F., 'Ion-induced erosion of tungsten surfaces studied by a sensitive quartz-crystal-microbalance technique', *Journal of Nuclear Materials*, 390-391, 1102 (2009), URL `https://www.doi.org/10.1016/j.jnucmat.2009.01.279`

[104] Dobes K., Smejkal V., Schäfer T. and Aumayr F., 'Interaction between seeding gas ions and nitrogen saturated tungsten surfaces', *International Journal of Mass Spectrometry*, 365-366, 64 (2014), URL `https://www.doi.org/10.1016/j.ijms.2013.11.015`

[105] Guseva M.I., Suvorov A.L., Korshunov S.N. and Lazarev N.E., 'Sputtering of beryllium, tungsten, tungsten oxide and mixed W–C layers by deuterium ions in the near-threshold energy range', *Journal of Nuclear Materials*, 266-269, 222 (1999), URL `https://www.doi.org/10.1016/s0022-3115(98)00819-8`

[106] Roth J., Bohdansky J. and Ottenberger W., 'Data on Low Energy Light Ion Sputtering', Report (1979), URL `http://hdl.handle.net/11858/00-001M-0000-0027-6AE6-7`

[107] Borders J.A., Langley R.A. and Wilson K.L., 'Low energy hydrogen and deuterium sputtering measurements of stainless steel, graphite, and beryllium oxide', *Journal of Nuclear Materials*, 76-77, 168 (1978), URL `https://doi.org/10.1016/0022-3115(78)90131-9`

[108] Hintz E., Rusbüldt D., Schweer B., Bohdansky J., Roth J. and Martinelli A.P., 'The determination of the flux density of sputtered atoms by means of pulsed dye laser excited fluorescence', *Journal of Nuclear Materials*, 93-94, 656 (1980), URL `https://doi.org/10.1016/0022-3115(80)90188-9`

[109] Eckstein W., Garcia-Rosales C., Roth J. and Ottenberger W., 'Sputtering Data', Report (1993), URL `http://hdl.handle.net/11858/00-001M-0000-0027-6324-6`

[110] Sugiyama K., Schmid K. and Jacob W., 'Sputtering of iron, chromium and tungsten by energetic deuterium ion bombardment', *Nuclear Materials and Energy*, 8, 1 (2016), URL `https://www.doi.org/10.1016/j.nme.2016.05.016`

[111] Laegreid N. and Wehner G.K., 'Sputtering Yields of Metals for Ar+ and Ne+ Ions with Energies from 50 to 600 ev', *Journal of Applied Physics*, 32, 365 (1961), URL `https://www.doi.org/10.1063/1.1736012`

[112] Weijsenfeld C.H., Hoogendoorn A. and Koedam M., 'Sputtering of polycrystalline metals by inert gas ions of low energy (100–1000 eV)', *Physica*, 27, 763 (1961), URL `https://doi.org/10.1016/0031-8914(61)90093-3`

[113] Berger B.M., Stadlmayr R., Meisl G., Čekada M., Eisenmenger-Sittner C., Schwarz-Selinger T. and Aumayr F., 'Transient effects during erosion of WN

by deuterium ions studied with the quartz crystal microbalance technique', *Nuclear Instruments and Methods in Physics Research Section B: Beam Interactions with Materials and Atoms*, 382, 82 (2016), URL `https://www.doi.org/10.1016/j.nimb.2016.04.060`

[114] Smith J. N. J., Meyer C. H. J. and Layton J.K., 'Low-yield sputtering measurements on CTR materials using Auger electron spectroscopy', *Transactions of the American Nuclear Society*, 29–30 (1975), URL `http://inis.iaea.org/search/search.aspx?orig_q=RN:07250064`

[115] Karmakar P. and Ghose D., 'Ion beam sputtering induced ripple formation in thin metal films', *Surface Science*, 554, L101 (2004), URL `https://www.doi.org/10.1016/j.susc.2004.02.020`

[116] Roth J., Sugiyama K., Alimov V., Höschen T., Baldwin M. and Doerner R., 'EUROFER as wall material: Reduced sputtering yields due to W surface enrichment', *Journal of Nuclear Materials*, 454, 1 (2014), URL `https://www.doi.org/10.1016/j.jnucmat.2014.07.042`

[117] Lindau R., Möslang A., Rieth M., Klimiankou M., Materna-Morris E., Alamo A., Tavassoli A.A.F., Cayron C., Lancha A.M., Fernandez P., Baluc N., Schäublin R., Diegele E., Filacchioni G., Rensman J.W., Schaaf B.v.d., Lucon E. and Dietz W., 'Present development status of EUROFER and ODS-EUROFER for application in blanket concepts', *Fusion Engineering and Design*, 75-79, 989 (2005), URL `https://www.doi.org/10.1016/j.fusengdes.2005.06.186`

[118] von Toussaint U. and Mutzke A., 'Fluence dependent changes of erosion yields and surface morphology of the iron-tungsten model system: SDTrimSP-2D simulation studies', *Nuclear Materials and Energy*, 12, 318 (2017), URL `https://www.doi.org/10.1016/j.nme.2016.09.005`

[119] Shin K., Wataru S., Noriyasu O., Naoaki Y. and Tsubasa S., 'Formation process of tungsten nanostructure by the exposure to helium plasma under fusion relevant plasma conditions', *Nuclear Fusion*, 49, 095005 (2009), URL `https://www.doi.org/10.1088/0029-5515/49/9/095005`

[120] Baldwin M.J., Lynch T.C., Doerner R.P. and Yu J.H., 'Nanostructure formation on tungsten exposed to low-pressure rf helium plasmas: A study of ion energy threshold and early stage growth', *Journal of Nuclear Materials*, 415, S104 (2011), URL `https://doi.org/10.1016/j.jnucmat.2010.10.050`

126

[121] Baldwin M.J. and Doerner R.P., 'Helium induced nanoscopic morphology on tungsten under fusion relevant plasma conditions', *Nuclear Fusion*, 48, 035001 (2008), URL `http://dx.doi.org/10.1088/0029-5515/48/3/035001`

[122] Möller S., Kachko O., Rasinski M., Kreter A. and Linsmeier C., 'In situ investigation of helium fuzz growth on tungsten in relation to ion flux, fluence, surface temperature and ion energy using infrared imaging in PSI-2', *Physica Scripta*, T170, 014017 (2017), URL `http://dx.doi.org/10.1088/1402-4896/aa8a0a`

[123] Baldwin M.J. and Doerner R.P., 'Formation of helium induced nanostructure 'fuzz' on various tungsten grades', *Journal of Nuclear Materials*, 404, 165 (2010), URL `https://doi.org/10.1016/j.jnucmat.2010.06.034`

[124] Petty T.J., Baldwin M.J., Hasan M.I., Doerner R.P. and Bradley J.W., 'Tungsten 'fuzz' growth re-examined: the dependence on ion fluence in non-erosive and erosive helium plasma', *Nuclear Fusion*, 55, 093033 (2015), URL `http://dx.doi.org/10.1088/0029-5515/55/9/093033`

[125] Nishijima D., Baldwin M.J., Doerner R.P. and Yu J.H., 'Sputtering properties of tungsten 'fuzzy' surfaces', *Journal of Nuclear Materials*, 415, S96 (2011), URL `https://www.doi.org/10.1016/j.jnucmat.2010.12.017`

[126] Noda N., Philipps V. and Neu R., 'A review of recent experiments on W and high Z materials as plasma-facing components in magnetic fusion devices', *Journal of Nuclear Materials*, 241-243, 227 (1997), URL `https://doi.org/10.1016/S0022-3115(97)80042-6`

[127] Kreter A., Brandt C., Huber A., Kraus S., Möller S., Reinhart M., Schweer B., Sergienko G. and Unterberg B., 'Linear Plasma Device PSI-2 for Plasma-Material Interaction Studies', *Fusion Science and Technology*, 68, 8 (2015), URL `https://doi.org/10.13182/FST14-906`

[128] Gardner J.P., Mather J.C., Clampin M., Doyon R., Greenhouse M.A., Hammel H.B., Hutchings J.B., Jakobsen P., Lilly S.J., Long K.S., Lunine J.I., McCaughrean M.J., Mountain M., Nella J., Rieke G.H., Rieke M.J., Rix H.W., Smith E.P., Sonneborn G., Stiavelli M., Stockman H.S., Windhorst R.A. and Wright G.S., 'The James Webb Space Telescope', *Space Science Reviews*, 123, 485 (2006), URL `https://doi.org/10.1007/s11214-006-8315-7`

[129] Vladimirov P., Bachurin D., Borodin V., Chakin V., Ganchenkova M., Fedorov A., Klimenkov M., Kupriyanov I., Moeslang A., Nakamichi M., Shibayama T., Til S.V. and Zmitko M., 'Current Status of Beryllium Materials for Fusion Blanket Applications', *Fusion Science and Technology*, 66, 28 (2014), URL `https://doi.org/10.13182/FST13-776`

[130] Roth J., Tsitrone E., Loarte A., Loarer T., Counsell G., Neu R., Philipps V., Brezinsek S., Lehnen M., Coad P., Grisolia C., Schmid K., Krieger K., Kallenbach A., Lipschultz B., Doerner R., Causey R., Alimov V., Shu W., Ogorodnikova O., Kirschner A., Federici G. and Kukushkin A., 'Recent analysis of key plasma wall interactions issues for ITER', *Journal of Nuclear Materials*, 390-391, 1 (2009), URL `https://www.doi.org/10.1016/j.jnucmat.2009.01.037`

[131] Hwangbo D., Kawaguchi S., Kajita S. and Ohno N., 'Erosion of nanostructured tungsten by laser ablation, sputtering and arcing', *Nuclear Materials and Energy*, 12, 386 (2017), URL `https://www.doi.org/10.1016/j.nme.2017.03.004`

[132] Cupak C., Phd thesis (ongoing)
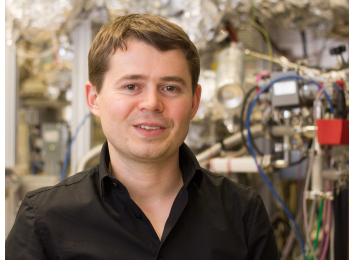
Reinhard
STADLMAYR

Curriculum Vitae

Personal Information

Address	Scheugasse 1/13, 1100 Vienna, Austria
Phone	(+43) 699 11501151
Email	stadlmayr@iap.tuwien.ac.at
Date of Birth	August 29th, 1982
Place of Birth	Gmunden, Austria
Nationality	Austria
ORCID	0000-0001-5194-1933

Education

2016–2020 **Doctoral programme in Engineering Science: Technical Physics**, *TU Wien, Austria*.
Thesis topic: 'Erosion of Fusion Relevant Materials - Experiments and Modelling'
Supervisor: Prof. Friedrich Aumayr

2013–2016 **Master's programme in Technical Physics**, *TU Wien, Austria*.
Dipl.Ing. (MSc) graduation in March 2016, with distinction
Thesis topic: 'Erosion of Tungsten-Nitride and Iron-Tungsten Surfaces under Deuterium Ion Impact'

2014 **ATHENS student exchange programme**, *TU Delft, Netherlands*.

2014 **Erasmus student exchange programme**, *University of Umeå, Sweden*.

2009–2013 **Bachelor's programme in Technical Physics**, *TU Wien, Austria*.
BSc graduation in February 2013

1997–2002 **Federal College of Engineering**, *HTL Steyr, Austria*, specialising in electronics and informatics.
Matura (secondary education graduation diploma) in June 2002

1993–1997 **Secondary Modern School**, *HS Gmunden Traundorf*.

1989–1993 **Ground School**, *VS Gschwandt bei Gmunden*.

Awards

2013	**Leistungsstipendium (Academic Merit Award)**, *TU Wien, Austria*.

Languages

German	Mother tongue
English	Fluent
Swedish	Basic words and phrases

Work Experience

2016–2020	**Project Assistant**, *Institute of Applied Physics*, TU Wien, Austria.
	Activities: Laboratory work on plasma-wall interaction processes relevant for fusion experiments, as well as mentoring of master and bachelor students.
2003–2009	**Service Technician**, *GFM GmbH*, Steyr, Austria.
	Activities: Assembling, programming and commissioning of CNC machines for metal forming, as well as international servicing and operator training.
	Engineer (Ing.) title awarded in 2007
2002–2003	**Military Service**.

Other Activities

- Extreme Sports: Trailrunning
- Member of a Volunteer Fire Brigade